ANALYSIS OF SYNCHRONOUS AND ASYNCHRONOUS WHIRL OF JEFFCOTT ROTOR CONSIDERING MATERIAL NON-LINEARITY

by

Shah Mohammad Mohiuddin Siddique

A Thesis submitted for partial fulfillment of the requirements for the degree of
MASTER OF SCIENCE IN MECHANICAL ENGINEERING

DEPARTMENT OF MECHNANICAL ENGINEERING
BANGLADESH UNIVERSITY OF ENGINEERING AND TECHNOLOGY
DHAKA-1000, BANGLADESH
February 2018

The thesis titled "**Analysis of Synchronous and Asynchronous Whirl of Jeffcott Rotor Considering Material Non-Linearity.**" submitted by Shah Mohammad Mohiuddin Siddique, Roll No.:0413102118 Session: April 2013, has been accepted as satisfactory in partial fulfillment of the requirement for the degree of MASTER OF SCIENCE IN MECHANICAL ENGINEERING on 13 February 2018
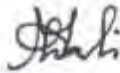
BOARD OF EXAMINERS

Dr. M. Ashiqur Rahman
Professor
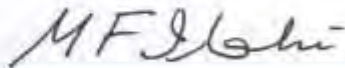Department of Mechanical Engineering
BUET, Dhaka-1000

Chairman

Dr. Md. Abdus Salam Akanda
Professor
Department of Mechanical Engineering
BUET, Dhaka-1000

Member

Dr. Mohammad Ali
Professor and Head
Department of Mechanical Engineering
BUET, Dhaka-1000

Member
(Ex- officio)

Dr. Muhammad Fazli Ilahi
Professor (Ex – VC, IUT, OIC)
House No. 13, Road No. 1, Sector 11,
Uttara Model Town, Dhaka.

Member
(External)

CANDIDATE'S DECLARATION

It is hereby declared that this thesis or any part of it has not been submitted elsewhere for the award of any degree or diploma.

_____

Shah Mohammad Mohiuddin Siddique

DEDICATION

I dedicate this thesis to my parents and my brother.

CONTENTS

List of Figures

List of Symbols & Abbreviations

a	=	Acceleration (m/s^2)
c	=	Coefficient of damping (Ns/m)
c_c	=	Coefficient of Critical damping (Ns/m)
d	=	Diameter of the shaft (mm)
E	=	Modulus of elasticity (GPa)
E_r	=	Reduced modulus of elasticity (GPa)
e	=	Eccentricity of circular disc (mm)
G	=	Center of gravity
h_1, h_2	=	Positions of the farthest fibers measured w.r.t neutral axis (mm)
I	=	Moment of inertia (mm^4)
i	=	Radial direction
j	=	Tangential direction
k	=	Linearly elastic bending stiffness of the shaft material (N/m)
M	=	Bending moment (Nm)
m	=	Disc mass (g)
P_d	=	Dynamic force acting at the shaft center (N)
r, Y_1	=	Whirling amplitude (mm)
$\dot{r}, Y_2$	=	Radial velocity (m/s)
θ, Y_3	=	Angular displacement (rad)
$\dot{\theta}, Y_4$	=	Whirl speed, whirl frequency (rad/s)
t	=	Time (s)
v	=	Gradient of a straight line
w	=	Radius of the circular shaft. (mm)
z	=	Intercept at y-axis by a straight line (mm)
$\ddot{r}$	=	Radial acceleration (m/s^2)
ω	=	Forcing frequency, Spin speed (rad/s)
ω_n	=	Natural frequency, (rad/s)

β	$=$	Spin ratio $\left(\frac{\omega}{\omega_n}\right)$
ξ	$=$	Damping ratio $\left(\frac{c}{c_c}\right)$
σ	$=$	Stress (MPa)
ε	$=$	Strain
ε_1	$=$	Tensile strain
ε_2	$=$	Compressive strain
ρ	$=$	Radius of curvature (mm)
$\Delta, \varepsilon_1 + \varepsilon_2$	$=$	Sum of absolute values of the maximum elongation and the maximum contraction of shaft's lengthwise fibers.
φ, δ	$=$	Phase angle (rad)
λ	$=$	Whirl speed ratio $\left(\frac{\dot{\theta}}{\omega}\right)$
kr	$=$	Radial restoring force due to bending stiffness (N)
$c\dot{r}$	$=$	Radial damping force (N)
$cr\dot{\theta}$	$=$	Tangential damping force (N)
SDOFS	$=$	Single degree of freedom system
2DOFS	$=$	Two degrees of freedom system (r & θ)
MDOFS	$=$	Multiple degrees of freedom system
SMA	$=$	Shape Memory Alloy

Acknowledgement

Abstract

Whirling is defined as the rotation of the plane made by the bent shaft and the line of centers of the bearing. The phenomenon of whirling of shaft is often explained in terms of a "Jeffcott rotor model". The Jeffcott rotor consists of a simply supported flexible shaft with a rigid thin disc mounted at the mid-span. Whirling results from various causes such as: a) Mass eccentricity (rotating unbalance), b) Lack of initial straightness of the shaft, c) Non-homogenous material, d) Unbalanced magnetic pull in case of electrical machinery e) Lubricant viscosity, f) Shaft material's initial stiffness and number of supports, g) Unbalanced centrifugal forces, h) Hysteresis characteristics of shaft materials etc.

In this thesis whirling is extensively studied considering eccentric mass centre of the rotor on the shaft. Generally, two modes of whirling (synchronous and asynchronous) can be observed in various rotating machines. In the synchronous motion of the shaft, the whirl (also called orbital) speed and its own spin speed are equal. However, in case of asynchronous whirl motion of the shaft, the orbital speed and its own spin speed are not equal.

Previous studies of Jeffcott rotor mostly dealt with synchronous whirl considering steady-state vibration and involving linearly elastic shaft materials. Therefore, present thesis aims to focus following unexplored but important points concerning whirling of shafts: asynchronous mode of whirl, whirl during transient vibration and, the effect of material non-linearity (that is, the shaft material has a non-linear stress-strain relation and Hook's law cannot be applied) on the shaft's response.

To accomplish the goals, at first, a new theoretical model has been developed to predict response of shafts during steady-state whirl (both synchronous mode as well as asynchronous mode) in terms of exact solutions. Thus, differences between the shaft responses are analyzed for synchronous and asynchronous modes of whirl during steady-state vibration.

Secondly, a new mathematical model has been developed to predict response of shafts during unsteady-state (transient) whirl in terms of numerical solutions. Original non-linear second order governing differential equations are solved as an initial value problem.

Next, results from transient solutions and exact solutions are compared.

Thirdly, material non-linearity issue is handled in terms of a mathematical model that has been developed to solve pure bending of a shaft (that is whirling), the material of which does not follow Hooke's law. It should be noted here that, SMA inherently has highly non-linear stress-strain curves in tension and compression. Thus, bending moment-curvature and reduced modulus-curvature relations are obtained for a superelastic SMA shaft. Results are used to predict effect of material non-linearity on the response of a whirling shaft.

Effect of various other factors like damping ratio, eccentricity ratio, whirl speed ratio and spin ratio on response of whirling shafts are studied and analyzed. Some salient findings are as follows.

The Jeffcott rotor system behaves as a single degree of freedom system. For steady-state and synchronous whirl, increased damping greatly reduces whirling amplitude and its maximum value is at spin ratio of unity, because of resonance. However, for large value of spin ratio, non-dimensional whirling amplitude approaches unity. Another interesting finding is that, all load-spin ratio curves intersect at a spin ratio of 1.414.

Interestingly, for asynchronous whirl, resonance does not occur at a spin ratio of unity. Rather, it is the whirl speed ratio that determines at what speed resonance will occur.

As material non-linearity is taken into account some portion of the shaft is found to experience stresses (different magnitude in tension and compression) beyond proportional limit. Effect of material non-linearity becomes prominent as whirl

amplitude starts to become large. Moreover, the maximum deflection of a shaft is found to be much larger when material non-linearity is considered in comparison to the case of linearly elastic shaft material.

When, unsteady-state whirl of Jeffcott rotor is considered, the peak value of whirling amplitude is found to be almost equal to that for steady-state whirl. In turn, it proves soundness of the entire mathematical scheme because steady-state solutions are exact (obtained analytically from the simplified mathematical model) and transient solutions are obtained by numerical method from the original non-linear governing equations. Beyond resonance, whirl amplitude increases with the spin ratio. Also increased eccentricity increases the whirl amplitude. However, peaks at resonance disappear with increasing damping ratio.

Finally, an experimental setup is constructed and distinct whirling is demonstrated at and above resonance. Material non-linearity and inelastic behavior of shaft is demonstrated by permanently bent shaft due to whirling. Experimental observations are explained in terms of mathematical predictions.

Key words: Jeffcott rotor, Whirl, Synchronous whirl, Asynchronous whirl, Material non-linearity, Steady-state whirl, Unsteady-state whirl, Threshold bending moment, Reduced modulus, Transient solution.

CHAPTER 1

INTRODUCTION

1.1 Introduction to Whirling of Rotating Shaft

Rotating machines are extensively used in diverse engineering applications, such as power stations, marine propulsion systems, aircraft engines, machine tools, automobiles, household accessories and futuristic micro and nano-machines. The design trend of such systems in modern engineering is towards lower weight and operating at super critical speeds. An accurate prediction of rotor system dynamic characteristics is vitally important in the design of any type of machinery. Of the many published works, the most extensive portion of the literature on rotor dynamics analysis is concerned with determining critical speeds, natural whirl frequencies, the instability thresholds and bands, and the unbalance and transient responses [Rajiv (2017)]. Apart from these analyses some works also cover balancing of rotors, the estimation of bearing dynamic parameters, the condition monitoring and the non-linear analysis.

In this thesis, a great interest is shown for the different aspects of whirling of rotating shaft and non-linear analysis of shaft materials.

Rotating shafts tend to bow out at certain speeds and whirl in a complicated manner [Thomson et al. (2011)]. Whirling is defined as the rotation of the plane made by the bent shaft and the line of centers of the bearing. To understand the phenomena of whirling of shaft, "Jeffcott rotor model" is considered.

1.2 Jeffcott Rotor model

Jeffcott rotor consists of a simply supported flexible shaft with a rigid thin disc mounted at the mid-span. The disc center of rotation, C, and its center of gravity, G, is offset by a distance e, which is called the eccentricity. The shaft spin speed is ω, and the shaft whirls about the bearing axis with a whirl frequency, $\dot{\theta}$. Shaft mass is ignored in comparison to disc mass in this Jeffcott rotor.

The vibration theory for rotor-dynamic systems was first developed by August Föppl (Germany) in 1895 and Henry Homan Jeffcott (England) in 1919 [Yoon et. al. (2013)]. Employing a simplified rotor/bearing system, they developed the basic theory on prediction and attenuation of rotor vibration. This simplified rotor system that is commonly known as the Föppl/Jeffcott rotor, or simply the Jeffcott rotor, is often employed to evaluate rotor-dynamic systems in the real world. Jeffcott (1919) proposed this model and Figure 1.1 shows a typical Jeffcott (it is also called Föppl or Laval) rotor model [Rajiv (2014)].

1.3 Causes of Whirling of Rotating Shaft

All rotating/spinning shafts, even in the absence of external load, will deflect due to various factors during rotation. Whirling is defined as the rotation of the plane made by the bent shaft and the line of centers of the bearing. The unbalanced mass of the rotating object causes deflection that will create resonant vibration at certain speeds, known as the critical speeds. When a shaft is having a rotor or without a rotor, its center of gravity usually doesn't coincide with the axis of rotation of the shaft, this center of gravity is normally displaced from the axis of rotation, although the amount of displacement may be very small. The phenomenon of whirling of rotating shaft results from various causes such as pointed out by various researchers [1, 4-8, 13-15, 17-19, 23].

a) Mass eccentricity of the rotor on the shaft.

b) Lack of initial straightness of the shaft.

c) Bending of shaft under the action of gravity in case of horizontal shaft.

d) Non-homogenous material.

e) Unbalanced magnetic pull in case of electrical machinery.

f) Lubricant viscosity.

g) Shaft material's initial stiffness and number of supports.

h) Unbalanced centrifugal forces.

i) Hysteresis characteristics of shaft materials.

j) Gyroscopic effect.

Generally two types of whirling can be observed in various rotating machines. These are,

1. Synchronous whirl motion.

2. Asynchronous whirl motion.

In the synchronous motion of the shaft, the whirl $(\dot{\theta})$ speed and its own spin speed (ω) are equal as shown in Figure 1.2. The sense of rotation of the shaft spin and the whirling are also same. The black spot on the shaft represents the unbalance location on to the shaft. The unbalance force, in general, leads to synchronous whirl conditions, hence this motion is basically a forced response.

In case of asynchronous whirl motion of the shaft, the orbital speed and its own speed are not equal $(i.e., \dot{\theta} \neq \omega)$. Generally asynchronous whirl motion may occur when speeds are high (e.g., when gyroscopic effect predominates) or when the rotor is asymmetric or when dynamic properties of the bearing are anisotropic. The asynchronous whirl motion may occur even in the perfectly balanced rotor, and due to this it will have whirl frequency as one of the natural frequencies of the rotor system as long as the rotor linear model is considered. The black mark on to the shaft will not be so systematic as in synchronous whirl (Figure 1.2) and may occupy various positions depending upon the frequency of whirl.

Other kind of whirl motion, which may occur in real systems is anti-synchronous $(i.e, \dot{\theta} = -\omega)$; as shown in Figure 1.3. The anti-synchronous whirl may occur when there is rubbing between the rotor and the stator, however, it occurs very rarely. For this case, the sense of rotation of the shaft spin and the whirling are opposite.

Figure 1.1 illustrates the single mass Jeffcott rotor with rigid bearings. The rotor disc with mass m is located at the axial center of the shaft. In this study, mass of the shaft in the Jeffcott rotor is assumed to be negligible compared to that of the disc. The geometric center of the disc C is located at the point (U_xC, U_yC) along coordinate axes defined about the bearing center line, and the disc center of mass G is located at (U_xG, U_yG). The unbalance eccentricity (e_u) is the vector connecting the points C and G, and it

represents the unbalance in the rotor disc. This mass unbalance can cause whirling in rotating shaft as mentioned in this section earlier.

If it is assumed that the material of a rotating shaft is perfectly elastic and any kind of damping is neglected, then on the basis of these two assumptions, two forms of whirling of the shaft due to some eccentricity is generally possible, namely (1) below the critical speed and (2) above the critical speed [Timoshenko (1955)]. It was found that in both cases the plane containing the bent axis of the shaft rotates with the same speed as the shaft itself. Both these forms of motion are theoretically stable so that if a small deviation from the circular path of the center of gravity of the disc is produced by impact, for example, the result is that small vibrations in a radial and in a tangential direction are superposed on the circular motion of the center of gravity. The existence of such motion can be demonstrated by the use of a suitable stroboscope. In this way it can also be shown that due to unavoidable damping the vibrations gradually die out if the speed of the shaft is below critical speed (ω_{cr}). However if it is above ω_{cr} a peculiar phenomenon sometimes can be observed, namely, that the plane of the bent shaft rotates at the ω_{cr} while the shaft itself is rotating at a higher speed ω. Sometimes this motion has a steady character and the deflection of the shaft remains constant. At other times the deflection tends to grow with time up to the instant when the disc strikes the guard. To explain this phenomenon the imperfection in the elastic properties of the shaft must be considered.

Experiments with repeated tension-compression show that all materials exhibit some hysteresis characteristics so that instead of a straight line *AA* (Figure 1.4), representing Hooke's law, we usually obtain a loop of which the width depends on the limiting values of stresses applied in the experiment. If the loading and unloading is repeated several hundred times, the shape of the loop is finally stabilized and the area of the loop gives the amount of energy dissipated per cycle due to hysteresis. Timoshenko (1955) pointed out that such a hysteresis contributes to the whirling of shaft.

One of the important aspects on dynamic behaviors of the rotor system is the gyroscopic effect, which predominates especially for high speed rotor. Gyroscopic effects affect the synchronous as well as the asynchronous whirl. Rajiv (2017) analyses

gyroscopic effect on rotor system by two different approaches, firstly by the quasi-static analysis (which gives a better physical insight into the effect of gyroscopic effects, however, can be applied practically to simple systems only), and secondly by the dynamic analysis (which can be easily extended to MDOF systems). Rajiv (2017) showed that because of the gyroscopic effect the whirl natural frequency becomes dependent on the rotor spin speed. Another interesting phenomenon that can be observed is that the rotor can have the forward and backward whirling motion.

Whirl also takes place due to fluid trapped in rotor according to Crocker (1998). This occurs in hollow rotors, mostly in high-speed rotating machinery, where liquids (such as oil in bearing sumps or steam condensates) inadvertently be trapped in the internal cavity of the rotors. The spinning surface of the cavity drags fluid in the direction of rotation. The deflection of the shaft and the centrifugal forces on the trapped fluid produce a force having a tangential component, inducing a forward whirl. Crocker (1998) showed that the onset speed for instability is always above the critical speed of the rotor and below twice the critical speed.

Dry friction whip is experienced when the surface of the rotating shaft comes in contact with an unlubricated stationary surface. This can be caused by inadequate journal bearing lubrication, contact between rotors and labyrinth seals, or turbo machinery blade rubs. The contact between the surface of the rotating shaft and the stationary surface will induce a tangential force on the rotor, which then produces a whirling motion. This generates a larger centrifugal force on the rotor. No first-order interdependence of whirl speed with rotational speed is established. It has been suggested that the whirl frequency is half the rotational speed of the rotor [Crocker (1998)].

1.4 Motivation for the Present Study

As rotating machines have been used extensively in diverse engineering applications, an accurate prediction of rotor system dynamic characteristics (often dictated by whirling of a shaft) is vitally important in the design of any type of machinery.

For the sake of simplicity, researches regarding vibration of shafts have been limited mostly to steady-state and synchronous whirl. Obviously in practical applications shaft may whirl in asynchronous mode and moreover, stresses in shaft may exceed elastic limit during whirling. But literature survey shows no research on asynchronous and synchronous whirling considering inelastic shaft material (that is, the shaft material has a non-linear stress-strain relation and Hooke's law cannot be applied).

Therefore, present study aims to focus the above-mentioned unexplored points concerning whirling of shafts.

In this dissertation, the terms 'Transient' and 'Unsteady-state' are interchangeably used to indicate time dependent solutions. In similar fashion, words 'Superelastic SMA' and 'SMA' are used interchangeably to indicate a smart material that can regain original size and shape from an apparently plastically deformed state.

1.5 Objectives

Present study aims to extensively deal with whirling of shafts. However, the work will focus specifically on whirl during transient period and asynchronous whirl of shaft with a Jeffcott rotor where the shaft material can possess a non-linear stress-strain relation. Objectives of this study can be summarized as below:

a) To develop a mathematical model for pure bending of Jeffcott rotor shafts while whirling, the material of which may be elastic (stress-strain relation is linear) and Hooke's law can be applied or, inelastic (having a non-linear stress-strain relation). The model will be able to handle steady-state as well as transient vibration pertaining to shaft whirling.

b) Based on (a), to develop a generalized computer code for analysis of whirling of Jeffcott rotor.

c) To obtain results (in terms of steady-state shaft response) for synchronous whirl of Jeffcott rotor considering elastic material and also inelastic material. It can be performed using the computer code.

d) To repeat step (c) for asynchronous whirl.

e) To analyze differences between the results obtained in (c) and (d) by changing some parameters like damping ratio, eccentricity, geometry, spin ratio, materials etc.

f) To obtain results for transient vibrations and to compare and validate some results with existing available exact results.

g) To analyze the effect of transient vibration on shaft whirling.

h) To experimentally demonstrate the effect of inelastic shaft deformation during whirling.

1.6 Outline of Methodology

Major steps of methodology of thesis for comprehensive analysis of whirling of Jeffcott rotor are as follows.

Handling of Material Non-linearity

Cross-section geometry plays an important role for inelastic bending of beams or buckling of columns [Research group of Rahman (2001, 2007, 2008 and 2009)]. In order to simulate inelastic bending of a shaft, at first the stress-strain curve of the beam material must be known. Next, the moment-curvature relation and reduced modulus-curvature relation for a particular cross-section should be evaluated. So far, simulation of response of beams and columns of rectangular cross-section has been carried out by research group of Rahman (2001, 2007, 2008 and 2009). But, a shaft has circular cross-section. Thus, following the same procedure as by them, present study first aims to develop a mathematical model for pure bending of shaft of circular cross-section as following paragraph describes briefly.

The non-linear stress-strain relation in tension and compression for the shaft material (superelasic SMA) is available in the Ph.D. thesis of Rahman (2001). Using that stress-strain relation and considering pure bending of shafts during whirling, following relationship will be developed

(i) Moment-curvature ($M - \varDelta$) relation.

(ii) Reduced modulus-curvature ($E_r - \varDelta$) relation.

Governing Equation of Shaft Deflection and Solution Technique

Governing equations of the Jeffcott rotor [Thomson et al. (2011), Rao (2012)] during whirl is determined considering dynamic equilibrium. Steady-state as well as transient vibration issues will be considered separately while solving the governing equations. In terms of whirl during transient period, integration technique will be used to find shaft response at a desired time. Using suitable initial boundary conditions and solving the governing equations shaft response at increasing time can be determined. While, exact solutions will be obtained for shaft whirl for the case of steady-state vibration.

(i) Shaft Response Considering Linearly Elastic Material

The governing equations will be solved for elastic shaft material and numerical & exact results (shaft response in terms of displacement, velocity, acceleration and the maximum stresses etc.) will be obtained. Both, synchronous as well as asynchronous whirl will be considered for finding the response.

(ii) Shaft Response Considering Material Non-linearity

Next, results (numerical and exact) will be obtained solving the governing equations considering material non-linearity of the shaft. Previously determined moment-curvature relation and reduced modulus-curvature relation will be used in this step of study. Again, synchronous as well asynchronous whirl will be considered for finding the response.

Differences between the results obtained in (i) and (ii) will be analyzed by changing some parameters like damping ratio (ξ), eccentricity ratio (w/e), spin ratio (β) & materials (Superelastic SMA & SS) etc. Change in shaft response for different conditions stated above will be recorded and discussed. Finally, an experimental set-up will be constructed to demonstrate whirling of shafts and possibly validate some of the results.

(iii) Selecting the Shaft Materials:

Upon unloading SMA can recover large strain (Figure 1.5) by virtue of superelasticity (SE) or pseudo elasticity (PE) through a hysteresis [Rahman (2001)]. However, conventional engineering material like steel invariably shows large inelastic plastic strain upon unloading due to material non-linearity effect.

Therefore, superelastic SMA shafts & Stainless steel (SS) shafts, both types are selected to predict and demonstrate material non-linearity effect due to severe shaft whirling.

CHAPTER 2
LITERATURE REVIEW

Whirling of rotating shaft is studied in rotor dynamics which is the branch of engineering that studies the lateral and torsional vibrations of rotating shafts, with the objective of predicting the rotor vibrations and containing the vibration level under an acceptable limit [Yoon et al. (2013)].

A large number of studies are reported in the literature dealing with the whirling of rotating shaft, out of which only a few are discussed. For example, Ankit et al. (2014) analyzed whirling speed and evaluate self-excited motion of the rotating shaft. Critical speed and self-excited vibration in which the exciting forces and induced motion are controlled by the motion itself is discussed here.

Swanson et al. (2005) gave a practical review of rotating machinery critical speeds and modes. Some important issues are discussed here like how relationship between resonance and natural frequencies, change of natural frequencies as shaft rotational speed changes. Pradeep et al. (2008) analyzed modal projections for synchronous rotor whirl. Here, synchronous whirl of an arbitrary axisymmetric rotor supported on ideal (rigid, mass less and frictionless) bearings is analyzed. The rotor is not assumed to be a shaft (i.e. a one-dimensional continuum) with or without objects attached to it.

Keshav (2014) did experimental investigation of shafts on whirling of shaft apparatus. He analyzed theoretical and practical frequencies of different shaft diameters. Kolenda and Marynarki (2012) analyzed whirling of asymmetric shaft under constant lateral force. This study deals with parametric vibrations of asymmetric shaft subjected to constant lateral force. Discrete and continuous undamped models of the vibrating system are considered under assumption that the rotational speed of the shaft is constant.

Whalley and Ameer (2009) have studied whirling prediction with geometrical shaft profiling. Here distributed parameter shaft-rotor models are considered. The

multivariable irrational, hyperbolic and circular function, input-output relationship for the system, is derived. Moreover conventional frequency response methods are employed in the determination of the critical speed condition.

Nelson (2007) analyzed lateral and torsional motion of spinning rotors with applications of Newton's and Euler's equations. This paper attempts to explain the dynamic behavior of spinning rotors without writing any equations.

Shyong et al. (2014) developed analytical solution for whirling speeds and mode shapes of a distributed-mass shaft with arbitrary rigid discs. This paper presents an approach for replacing the effects of each rigid disc mounted on the spin shaft by a lumped mass together with a frequency-dependent equivalent mass moment of inertia so that the whirling motion of a rotating shaft-disc system is similar to the transverse free vibration of a stationary beam and the technique for the free vibration analysis of a stationary beam with multiple concentrated elements can be used to determine the forward and backward whirling speeds, along with mode shapes of a distributed-mass shaft carrying arbitrary rigid discs.

Thomson et al. (2011) developed a general mathematical modeling to find out the shaft deflection. But for solving the equation, they only considered the synchronous whirl condition and simplified the equations. Rao et al. (2012) also developed mathematical modeling but like Thomson et al. (2011), they also considered synchronous whirl condition for solving the equations.

In all aforementioned work, for the sake of simplicity vibration of shafts has been limited mostly to synchronous whirl. Obviously in practical applications shaft may whirl in asynchronous mode. So rigorous analysis has to be done to understand asynchronous whirl of Jeffcott rotor.

Moreover, there may be situation where shaft deflection is so high at times where stresses in shaft may exceed elastic limit while whirling. But all aforementioned literature survey shows no research on whirling considering inelastic shaft material (that

is, the shaft material has a non-linear stress-strain relation and Hooke's law cannot be applied).

Timoshenko (1956) has developed a mathematical modeling of pure bending of rectangular beam the material of which does not follow Hooke's law. In order to simulate inelastic bending, moment-curvature relation and reduced modulus-curvature relation for a particular cross-section have been evaluated using known stress-strain curve of the material of the beam.

To the best of our knowledge, no work has been found out which deals with the combination of different types of whirls along with material non-linearity analysis of Jeffcott rotor. It is well known that the rotating shaft or bar often becomes unstable and finally bends or breaks down at a rotational speed near its natural frequency of lateral vibration, on account of so called whirling phenomena [Kokame et al. (1950)]. So it's necessary to find out at what shaft speed and shaft deflection, the material of shaft will exceed elastic limit.

Stainless Steel is one of the most durable metals. The minimum 12 percent chromium contained in stainless steel forms an invisible, protective, corrosion-resistant passive film on the surface [Farrissey (2004), kokame et al. (1950)]. Some types of stainless steel will retain its original appearance with no corrosion. Rahman & Kowser (2009) analyzed stainless steel leaf springs under quasi-static condition considering both material non-linearity and geometric non-linearity.

A shape-memory alloy (SMA, smart metal, memory metal, memory alloy, muscle wire, smart alloy) is an alloy that 'remembers' its original shape and that when deformed returns to its pre-deformed shape when heated. And cantilever beams with reducing cross-section along the span show much larger deflections compared to those of constant cross-section beams [Rahman & Kowser (2009)].

Therefore, to explore this interesting research area, SMA and SS both have been selected as shaft materials for a Jeffcott rotor that may whirl in a number of complicated modes.

With some background knowledge on the response of beams made of SMA and SS, both have been selected as shaft materials for a Jeffcott rotor that may whirl in a number of complicated modes, to explore this interesting research area.

CHAPTER 3

GOVERNING EQUATIONS

3.1 General

Following Thomson et al. (2011), governing equations of the system are derived from the free-body diagram given in Figure 3.1 [Thomson et al. (2011)]. After rearranging and employing necessary transformations, 2nd order differential equations are converted to first order differential equations. Runge-Kutta 4th order method of numerical integration is applied to solve those first order differential equations and transient solutions are obtained. While for steady-state vibration of the shaft, exact solutions are obtained from simplified form of the governing equations. It should be mentioned here that the terms 'results of transient/unsteady-state' have been used in this thesis to indicate results obtained by solving the original non-linear governing equations by numerical method. However, these numerical solutions are time dependent and cover both transient (initially) and steady-state (finally) vibration.

.

3.2 Governing Differential Equations for Whirling of the Jeffcott Rotor Shaft

A single disc of mass m symmetrically located on a shaft supported by two bearings is considered, which is shown in the Figure 3.1 [Thomson et al. (2011)]. The center of the mass G of the disc is at a distance e (eccentricity) from the geometric center S of the disc. The center line of the bearings intersects the plane of the disc at O, and the shaft center is deflected by $r = OS$.

It is assumed that the shaft (i.e., the line $e = SG$) to be rotating at a constant speed ω, and in the general case, the line $r = OS$ to be whirling at speed θ that is not equal to ω. For the equation of motion, acceleration of the mass center can be developed as follows:

$$a_G = a_S + a_{G/_S} \quad \text{………………………..} \quad (3.2.1)$$

Where a_s is the acceleration of S and $a_{G/_S}$ is the acceleration of G with respect to S. The later term is directed from G to S, because ω is constant. Resolving a_G in the radial

(or, i) and tangential directions (or, j), we have

$$a_G = [(\ddot{r} - r\dot{\theta}^2) - e\omega^2\cos(\omega t - \theta)]i + [(r\ddot{\theta} - 2\dot{r}\dot{\theta}) - e\omega^2\sin(\omega t - \theta)]j \quad \text{........}$$
(3.2.2)

Aside from the restoring force (kr) of the shaft, it is assumed that a viscous damping force ($c\dot{r}$) to be acting at S. The equations of motion resolved in the radial and tangential directions then become

$$-kr - c\dot{r} = m[\ddot{r} - r\dot{\theta}^2 - e\omega^2\cos(\omega t - \theta)]\text{..............} (3.2.3)$$
$$-cr\dot{\theta} = m\left[r\ddot{\theta} - 2\dot{r}\dot{\theta} - e\omega^2\dot{\sin}(\omega t - \theta)\right] \text{...........}(3.2.4)$$

Equations (3.2.3) and (3.2.4) are rearranged to

$$\ddot{r} + \frac{c}{m}\dot{r} + \left(\frac{k}{m} - \dot{\theta}^2\right)r = e\omega^2\cos(\omega t - \theta)\text{................}(3.2.5)$$
$$r\ddot{\theta} + \left(\frac{c}{m}r + 2\dot{r}\right)\dot{\theta} = e\omega^2\sin(\omega t - \theta) \text{.................}(3.2.6)$$

The symbols used denote,

ω = Shaft spin.

$\dot{\theta}$ = Shaft whirl speed.

e = Eccentricity.

kr = Restoring force due to bending stiffness.

$c\dot{r}$ = Radial damping force.

$cr\dot{\theta}$ = Tangential damping force.

3.3 An Approach to Solve the Governing Equations of Whirling of Jeffcott Rotor in Full Form

The general case of whirl as described by the foregoing equations comes under the classification of self-excited motion, where the exciting forces inducing the motion are controlled by the motion (that is, spin 'ω') itself. Because the variables in the last couple of non-linear equations are r and θ, the problem is that of 2DOF.

For transformations, let $r = Y_1$, $\dot{r} = Y_2$, $\theta = Y_3$ and $\dot{\theta} = Y_4$

$$r = Y_1 \ldots\ldots\ldots\ldots\ldots\ldots\ldots\ldots\ldots\ldots\ldots (3.3.1)$$

$$\frac{dY_1}{dt} = \dot{r} = Y_2 \ldots\ldots\ldots\ldots\ldots\ldots\ldots\ldots\ldots (3.3.2)$$

$$\theta = Y_3 \ldots\ldots\ldots\ldots\ldots\ldots\ldots\ldots\ldots\ldots (3.3.3)$$

$$\frac{dY_3}{dt} = \dot{\theta} = Y_4 \ldots\ldots\ldots\ldots\ldots\ldots\ldots\ldots (3.3.4)$$

With those transformations, governing equations of (3.2.5) and (3.2.6) can now be rewritten as a set of four first order ordinary differential equations (ODE) as follows:

$$\frac{dY_1}{dt} = \dot{r} = Y_2 \ldots\ldots\ldots\ldots\ldots\ldots\ldots\ldots\ldots\ldots\ldots(3.3.5)$$

$$\frac{dY_2}{dt} = e\omega^2 \cos(\omega t - Y_3) - \frac{c}{m} - \left(\frac{k}{m} - Y_4{}^2\right)Y_1 \ldots\ldots\ldots(3.3.6)$$

$$\frac{dY_3}{dt} = \dot{\theta} = Y_4 \ldots\ldots\ldots\ldots\ldots\ldots\ldots\ldots\ldots\ldots(3.3.7)$$

$$\frac{dY_4}{dt} = \frac{1}{Y_1}\left[e\omega^2 \sin(\omega t - Y_3) - \left(\frac{c}{m}Y_1 + 2Y_2\right)Y_4\right]\ldots\ldots\ldots(3.3.8)$$

Last four governing equations along with suitable boundary conditions are solved as an initial value problem by applying numerical method. Thus transient solutions for shaft whirl are obtained.

The magnitude of total force (P) acting on the Jeffcott rotor shaft due to whirl along with disc weight can be found out from the following Equation.

$$P = P_d + mg \ldots\ldots\ldots\ldots\ldots\ldots\ldots\ldots\ldots(3.3.9)$$

Where P_d is the dynamic load and mg = disc weight, and P_d can be obtained from following Equation.

$$P_d = \sqrt{(kr)^2 + (c\dot{r})^2 + (cr\dot{\theta})^2} \quad \ldots\ldots\ldots\ldots\ldots\ldots\ldots\ldots(3.3.10)$$

Dividing both sides of Equation 3.3.10 by mg (disc weight), we get

$$\frac{P_d}{mg} = \frac{\sqrt{(kr)^2 + (c\dot{r})^2 + (cr\dot{\theta})^2}}{mg} \quad \ldots\ldots\ldots\ldots\ldots\ldots\ldots\ldots\ldots\ldots(3.3.11)$$

Equation 3.3.11 represents the non-dimensional dynamic force acting at the shaft center due to whirling during transient/unsteady-state vibration.

3.4 Simplified Mathematical Modeling for Analysis of Steady-state Synchronous and Asynchronous Whirl of Jeffcott Rotor

The general case of whirl as described by the non-linear governing Equations 3.2.5 and 3.2.6 comes under the classification of self-excited motion as discussed earlier, where the exciting forces are induced by the motion itself. The problem is that of 2DOFS as the variables in these equations are r and θ.

Following simplifications are done in this chapter.

For steady-state motion, $\ddot{\theta} = \ddot{r} = \dot{r} = 0$

and for synchronous whirl condition, whirl speed $(\dot{\theta})$ = shaft spin (ω).

Due to above simplifications, the problem reduces to that of a SDOFS in r.

Previous studies [1, 4-8, 13-15, 17-19, 23] about shaft whirl are mostly about steady-state but synchronous whirl. So we have modified existing equations of steady-state synchronous whirl to some extent so that steady-state asynchronous whirl can also be analyzed from the similar exact solutions.

Thus, for the analysis of both steady-state synchronous and asynchronous whirl simultaneously, instead of $\dot{\theta} = \omega$, we considered $\dot{\theta} = \lambda\omega$ where λ is a real number. Thus we have,

$$\lambda = \text{Whirl ratio} = \frac{\dot{\theta}}{\omega}$$

$$\dot{\theta} = \lambda\omega \ \dots\dots\dots\dots\dots\dots\dots\dots\dots\dots\dots..\dots\dots\dots..(3.4.1)$$

And on integrating, we obtain

$$\theta = \lambda\omega t - \phi$$

$$\omega t - \theta = \omega t - \lambda\omega t - \phi$$

$$\omega t - \theta = \omega t(1 - \lambda) + \phi\dots\dots\dots\dots\dots\dots\dots\dots(3.4.2)$$

Under these circumstances, the phase angle between eccentricity e and whirling amplitude r is considered as

$$\delta = \omega t - \theta = \omega t(1 - \lambda) + \phi \dots\dots\dots\dots\dots\dots\dots(3.4.3)$$

With $\ddot{\theta} = \ddot{r} = \dot{r} = 0$, governing Equations 3.2.5 and 3.2.6 reduce to

$$\left(\frac{k}{m} - \lambda^2\omega^2\right)r = e\omega^2\cos[\omega t(1 - \lambda) + \phi]\dots\dots\dots\dots(3.4.4)$$

$$\frac{c}{m}r\lambda\omega = e\omega^2\sin[\omega t(1 + \lambda) + \phi]\dots\dots\dots\dots\dots(3.4.5)$$

Dividing Equation 3.4.5 by Equation 3.4.4, we obtain the following Equation for the phase angle

$$\tan[\omega t(1 - \lambda) + \phi] = \frac{\frac{c}{m}\lambda\omega}{(\frac{k}{m} - \lambda^2\omega^2)}\dots\dots\dots\dots\dots\dots(3.4.6)$$

$$\tan\delta = \frac{2\xi\beta\lambda}{1 - \lambda^2\beta^2}\dots\dots\dots\dots\dots\dots\dots\dots\dots\dots\dots\dots\dots(3.4.7)$$

$$\delta = \tan^{-1}\frac{2\xi\beta\lambda}{1 - \lambda^2\beta^2}\dots\dots\dots\dots\dots\dots\dots\dots\dots\dots\dots\dots(3.4.8)$$

Where δ (phase angle), critical speed $\omega_n = \sqrt{\frac{k}{m}}$, and damping ratio $\xi = \frac{c}{c_c}$.

Where,

$c_c = (2 \times m \times \omega_n)$. Noting from the vector triangle of Figure 3.2,

$$\cos\delta = \frac{\left(\frac{k}{m} - \lambda^2\omega^2\right)}{\sqrt{\left(\frac{k}{m} - \lambda^2\omega^2\right)^2 + \left(\frac{c}{m}\omega\lambda\right)^2}}\dots\dots\dots\dots\dots\dots\dots(3.4.9)$$

And substituting into the first Equation 3.4.4 gives the amplitude Equation

$$r = \frac{me\lambda^2\omega^2}{\sqrt{(k - m\lambda^2\omega^2)^2 + (c\lambda\omega)^2}}\dots\dots\dots\dots\dots\dots\dots\dots\dots(3.4.10)$$

Employing $\beta = \frac{\omega}{\omega_n}$ in Equation 3.4.10,

$$r = \frac{e\lambda^2\beta^2}{\sqrt{(1-\lambda^2\beta^2)^2+(2\xi\beta\lambda)^2}}\quad\ldots\ldots\ldots\ldots..\ldots\ldots\ldots\ldots..(3.4.11)$$

$$\frac{r}{e} = \frac{\lambda^2\beta^2}{\sqrt{(1-\lambda^2\beta^2)^2+(2\xi\beta\lambda)^2}}\quad\ldots\ldots\ldots\ldots\ldots\ldots\ldots\ldots..(3.4.12)$$

Equation (3.4.12) represents non-dimensional whirl amplitude at steady-state in which $\lambda = 1$ and $\lambda = -1$ stand for synchronous and anti-synchronous whirl, respectively. While, $\lambda \neq \pm 1$ represents steady-state asynchronous whirl.

Equations 3.4.8, 3.4.9 and 3.4.11 indicate that the eccentricity line $e = SG$ leads the displacement line $r = OS$ by the phase angle δ, which depends on the amount of damping and the spin ratio ω/ω_n. When the rotation speed coincides with the critical speed $\omega_n = \sqrt{k/m}$, or the natural frequency of the shaft in lateral vibration, a condition of resonance is encountered in which the amplitude is restrained only by the damping.

The magnitude of total force (P) acting on the Jeffcott rotor shaft due to whirl along with disc weight can be found out form the following Equation

$$P = P_d + mg\quad\ldots\ldots\ldots\ldots\ldots\ldots\ldots\ldots.(3.4.13)$$

Where P_d is the dynamic load and mg is the disc weight and P_d is produced due to whirl only, and can be obtained from

$$P_d = \sqrt{(kr)^2 + (c\lambda\omega r)^2}\quad\ldots\ldots\ldots\ldots..\ldots..(3.4.14)$$

Dividing both sides of Equation 3.4.14 by kr (Restoring force), we get

$$\frac{P_d}{kr} = \sqrt{1 + \left(\frac{c\lambda\omega}{k}\right)^2}\quad\ldots\ldots\ldots\ldots\ldots..\ldots..(3.4.15)$$

Defining, critical damping coefficient, $c_c = 2m\omega_n$ $\ldots\ldots\ldots\ldots\ldots.\ldots.(3.4.16)$

Damping ratio, $\qquad \xi = \dfrac{c}{c_c}$ ……………...…………...(3.4.17)

Spin ratio, $\qquad \beta = \dfrac{\omega}{\omega_n}$ …………………………..(3.4.18)

Using Equations (3.4.16 – 3.4.18) in Equation 3.4.15, we get,

$$\frac{P_d}{kr} = \sqrt{1 + (2\xi\beta\lambda)^2} \quad …………..……..(3.4.19)$$

Dividing both sides of Equation 3.4.14 by *mg* (disc weight), we get

$$\frac{P_d}{mg} = \frac{\sqrt{(kr)^2 + (c\lambda\omega r)^2}}{mg} \quad …………..……..(3.4.20)$$

Thus, Equation 3.4.20 represents the non-dimensional force acting on the shaft center due to steady-state whirl, in contrast to Equation 3.3.11 that represents the same but due to whirling during transient/unsteady-state vibration.

3.5 Handling of Material Non-linearity

For materials having non-linear stress-strain relations Timoshenko (1956) derived the $M - \Delta$ and $E_r - \Delta$ relations for a rectangular beam section. He first defined the term reduced modulus, E_r for inelastic bending of beams.

Following Timoshenko (1956), it is assumed that the cross-section of the shaft remains plane during pure bending; hence elongations and contractions of longitudinal fibers are proportional to their distances from the neutral surface. Further assuming that during bending there exists the same relation between stress and strain as in the case of simple tension and compression, the stresses produced can be found out by a bending moment of a given magnitude. Considering the shaft of circular cross-section in Figures 3.3 & 3.4, it is assumed that the radius of curvature of the neutral surface produced by the moments M is equal to ρ. In such a case the unit elongation of a fiber at a distance y from the neutral surface is

$$\varepsilon = \frac{y}{\rho} \ldots\ldots\ldots\ldots\ldots\ldots\ldots\ldots\ldots\ldots(3.5.1)$$

Denoting h_1 and h_2 (Figure 3.4) the distances from the lower and the upper surfaces of the beam respectively to the neutral axis, we find that the elongation in the utmost fibers are

$$\varepsilon_1 = \frac{h_1}{\rho}, \varepsilon_2 = -\frac{h_2}{\rho} \ldots\ldots\ldots\ldots\ldots\ldots\ldots\ldots(3.5.2)$$

It is seen that the elongation or contraction of any fiber is readily obtained provided we know the position of the neutral axis, say ratio $\frac{h_1}{h_2}$, and the radius of curvature ρ. These two quantities can be found from the two equations of statics:

$$\int \sigma dA = \int_{-h_2}^{h_1} \sigma dA = 0 \ldots\ldots\ldots\ldots\ldots\ldots\ldots(3.5.3)$$

$$\int \sigma y dA = \int_{-h_2}^{h_1} \sigma y dy = M \ldots\ldots\ldots\ldots(3.5.4)$$

The first of these equations states that the sum of normal forces acting on a cross-section of the beam vanishes, since those forces represent a couple. The second equation states that the moment of the same forces with respect to the neutral axis is equal to the bending moment M.

Equation (3.5.3) is now used for determining the position of the neutral axis. For finding the area dA at first (Figure 3.4), we consider equation of the circle

$$x^2 + y^2 = w^2, (w = \text{radius of the circle}) \dots\dots\dots\dots\dots(3.5.5)$$

$$x = \sqrt{w^2 - y^2}\dots\dots\dots\dots\dots\dots\dots\dots\dots\dots(3.5.6)$$

Here,
$$dA = bdy \dots\dots\dots\dots\dots\dots\dots\dots\dots\dots\dots(3.5.7)$$

$$b = 2x = 2\sqrt{w^2 - y^2}\dots\dots\dots\dots\dots\dots\dots\dots(3.5.8)$$

Again
$$dA = bdy = 2\sqrt{w^2 - y^2}\, dy\dots\dots\dots\dots\dots\dots(3.5.9)$$

Now, employing dA in Equation 3.5.3, we get

$$\int \sigma dA = 2 \int_{-h_2}^{h_1} \sigma \sqrt{w^2 - y^2}\, dy = 0\dots\dots\dots\dots\dots\dots(3.5.10)$$

From Equation (3.5.1)

$$y = \rho\varepsilon \dots\dots\dots\dots\dots\dots\dots\dots\dots(3.5.11)$$

$$dy = \rho d\varepsilon \dots\dots\dots\dots\dots\dots\dots\dots(3.5.12)$$

Therefore, Equation 3.5.9 becomes

$$dA = 2\sqrt{w^2 - \rho^2\varepsilon^2}\,\rho d\varepsilon\dots\dots\dots\dots\dots\dots\dots(3.5.13)$$

Employing Equation 3.5.13 in 3.5.10, we get,

$$\int \sigma dA = 2 \int_{-h_2}^{h_1} \sigma \sqrt{w^2 - y^2}\, dy = 2\rho^2 \int_{\varepsilon_2}^{\varepsilon_1} \sigma \sqrt{(\tfrac{w}{\rho})^2 - \varepsilon^2}\, d\varepsilon = 0\dots\dots\dots(3.5.14)$$

Hence the position of the neutral axis is such that the integral $\int_{\varepsilon_2}^{\varepsilon_1} \sigma \sqrt{(\frac{w}{\rho})^2 - \varepsilon^2}\, d\varepsilon$

vanishes.

Therefore, $$\int_{\varepsilon_2}^{\varepsilon_1} \sigma \sqrt{(\frac{w}{\rho})^2 - \varepsilon^2}\, d\varepsilon = 0 \dots\dots\dots\dots\dots\dots(3.5.15)$$

Equation 3.5.15 is rewritten as

$$\int_{\varepsilon_2}^{0} \sigma \sqrt{(\frac{w}{\rho})^2 - \varepsilon^2}\, d\varepsilon = \int_{0}^{\varepsilon_1} \sigma \sqrt{(\frac{w}{\rho})^2 - \varepsilon^2}\, d\varepsilon \dots\dots\dots(3.5.16)$$

Integral on the left hand side of the Equation 3.5.16 represents normal forces acting on the compression region of the shaft and right hand side of the equation represents normal forces acting on the tension region of the shaft.

To determine the neutral axis position, we use the curve AOB (Figure 3.5a) which represents the $(\sigma - \varepsilon)$ diagrams in tension and compression for the material of the shaft, and we denote $\varDelta$, the sum of the absolute values of the maximum elongation and the maximum contraction, which is

$$\varDelta = |\varepsilon_1| + |\varepsilon_2| = \left|\frac{h_1}{\rho}\right| + \left|\frac{h_2}{\rho}\right| = \frac{h}{\rho} = \frac{d}{\rho} \dots\dots\dots\dots\dots\dots(3.5.17)$$

$$\rho = \frac{d}{\varDelta} \dots\dots\dots\dots\dots\dots\dots\dots\dots\dots\dots\dots\dots\dots\dots\dots\dots(3.5.18)$$

$$\rho = \frac{d}{|\varepsilon_1|+|\varepsilon_2|} \dots\dots\dots\dots\dots\dots\dots\dots\dots\dots\dots\dots\dots\dots(3.5.19)$$

Using Equation 3.5.19 in Equation 3.5.15, we get

$$\int_{\varepsilon_2}^{\varepsilon_1} \sigma \sqrt{\left(\frac{w}{\frac{d}{|\varepsilon_1|+|\varepsilon_2|}}\right)^2 - \varepsilon^2}\, d\varepsilon = 0 \dots\dots\dots\dots\dots\dots(3.5.20)$$

Or, $$\int_{\varepsilon_2}^{\varepsilon_1} \sigma \sqrt{\left(\frac{|\varepsilon_1|+|\varepsilon_2|}{2}\right)^2 - \varepsilon^2}\, d\varepsilon = 0 \dots\dots\dots\dots\dots\dots(3.5.21)$$

Since, integral of Equation 3.5.21 has no closed form solution, numerical solution technique has been used. As stress-strain curve of superelastic SMA is asymmetric in tension and compression beyond proportional limit,

Therefore,
$$|\varepsilon_1| \neq |\varepsilon_2|$$

Therefore, from the stress-strain curve $|\varepsilon_2|$ is chosen. And for any chosen values of $|\varepsilon_2|$, by applying numerical integration method, $|\varepsilon_1|$ is found out which can make the integral zero. In this manner we obtain strain ε_2 and ε_1 in the utmost fibers; Equation 3.5.2 then gives

$$\frac{h_1}{h_2} = \left|\frac{\varepsilon_1}{\varepsilon_2}\right| \ldots\ldots\ldots\ldots\ldots\ldots\ldots\ldots\ldots\ldots\ldots\ldots\ldots(3.5.22)$$

This determines the position of neutral axis. Observing that elongations ε are proportional to the distance from the neutral axis, we conclude that the curve AOB (Figure 3.5a) also represents the distribution of bending stresses along the depth of the beam, if h is substituted for Δ.

Therefore, the equation of moment at any of the point on the shaft is,

$$M = \int \sigma y dA = 2\rho^3 \int_{\varepsilon_2}^{\varepsilon_1} \sigma\varepsilon \sqrt{\left(\frac{w}{\rho}\right)^2 - \varepsilon^2} \, d\varepsilon \ldots\ldots\ldots..(3.5.23)$$

Applying numerical integration method to Equation 3.5.23, moments are known. Value of stress in Equation 3.5.23 is taken from corresponding value of strain from stress-strain curve.

If the stress-strain curve is known for a specific material, then considering the value of strain (piece-wise linear) from the diagram, value of corresponding stress can be found out.

Equation of straight line for $(x - y)$ coordinate,

$$y = vx + z \quad\text{……………...…..}(3.5.24)$$

Here, v is the gradient of the straight line.

Similarly for $(\sigma - \varepsilon)$ curve,

$$\sigma_{i+1} = v\varepsilon_{i+1} + \sigma_i \text{…..…………..}(3.5.25)$$

Equations 3.5.23 and 3.5.25 give,

$$M = 2\rho^3 \int_{\varepsilon_2}^{\varepsilon_1} \left[(v\varepsilon_{i+1} + \sigma_i)\sqrt{\left(\frac{w}{\rho}\right)^2 - \varepsilon^2} \right] \varepsilon d\varepsilon \text{………………..}(3.5.26)$$

Incorporating moment of inertia (I) in Equation 3.5.26, we get,

$$M = \frac{I}{\rho} \times \frac{128p}{\pi d\Delta^3} \int_{\varepsilon_2}^{\varepsilon_1} \left[(v\varepsilon_{i+1} + \right.$$

$$\left. \sigma_i)\sqrt{\left(\frac{w}{\rho}\right)^2 - \varepsilon^2} \right] \varepsilon \, d\varepsilon \text{………..………}(3.5.27)$$

Let, moment of inertia,

$$I = \frac{\pi d^4}{64} \quad\text{………………..…….…..….………}(3.5.28)$$

Linear moment-curvature relation,

$$M = \frac{EI}{\rho} \text{………….……………......………}(3.5.29)$$

If Equations (3.5.27) and (3.5.29) are compared, then for bending of shaft following , we conclude that beyond the proportional limit, the curvature produced by a moment M can be calculated from the equation,

$$M = \frac{E_r I}{\rho} \text{………………….…......…………}(3.5.30)$$

Here E_r is the reduced modulus. Now comparing Equations 3.5.27 and 3.5.30, the value of E_r (reduced value) can be obtained as follows.

$$E_r = \frac{128\rho}{\pi d \Delta^3} \int_{\varepsilon_2}^{\varepsilon_1} \left[(v + \sigma_i)\sqrt{\left(\frac{w}{\rho}\right)^2 - \varepsilon^2} \right] \varepsilon \, d\varepsilon \ldots\ldots\ldots\ldots(3.5.31)$$

The integral in this expression represents the moment with respect to the vertical (σ) axis through the origin O of the shaded area shown in Figure 3.5a. Since the ordinate of the curve in the figure represents stresses, and the abscissas, strain, the integral and also E_r have the dimension of GPa, i.e., the same dimension as the modulus E. The magnitude of E_r for a given material is a function of Δ or of h/ρ. Taking several values of Δ and using each time the curve in Figure 3.5a as was previously explained, we determine for each value of Δ the corresponding utmost elongations ε_1 and ε_2, and from Equation 3.5.31 the corresponding value of E_r as a function of ($\Delta = h/\rho$) is obtained.

Equations (3.5.26) and (3.5.31) can be solved by applying numerical method to obtain values of bending moment and reduced modulus for different values of Δ.

From the actual true stress-strain diagram (Figure 3.5b) random values of strain ε_2 from the compression region is chosen like that from Figure 3.5a and by using Equation 3.5.21 and by applying trial and error method, values of strain ε_1 at tension region is found out for which result of the integral of Equation 3.5.21 becomes zero each time. This determines the position of neutral axis and, value of total strain Δ as well. Romberg integration technique [Romberg (1955)] is used to solve this problem in Matlab.

Using values of ε_1 and ε_2 in Equation 3.5.17, value of Δ and corresponding ρ is found out from Equation 3.5.18 as well. Now, taking several values of Δ and using Equations 3.5.26 and 3.5.31, values of corresponding bending moment and reduced modulus are obtained. Again Romberg method of integration (1955) is used in matlab to solve Equations 3.5.26 and 3.5.31. Finally, Figures of $E_r - \Delta$ and M – are obtained for superelastic SMA shaft.

CHAPTER 4
RESULTS AND DISCUSSION

4.1 General Discussion

Whirling shaft's responses for different conditions (steady, synchronous and asynchronous etc.) are obtained in terms of exact and numerical solutions considering linearly elastic shaft material (Sections 4.2 for SMA and 4.5 for SS). In Section 4.3 and 4.4 effect of material non-linearity (w.r.t. Figures 3.5b, 4.1, 4.2) on the SMA shaft's response are also analyzed. Transient vibration during whirling is studied in section 4.6. Soundness of the mathematical scheme is proven in this section as well. In all cases viscous damping of different intensity is considered. It is assumed damping ratio (ξ) will be quite low (0.05) when the shaft whirls through air. However, if the shaft whirls in liquid (water or, oil) other values of damping ratio of 0.1-0.5 might be more realistic.

In this dissertation the terms 'Transient' and 'Unsteady-state' are interchangeably used to indicate time dependent solutions. In similar fashion, words 'Superelastic SMA' and 'SMA' are used interchangeably to indicate a smart material that can regain original size and shape from an apparently plastically deformed state.

It should be mentioned here that the terms 'results of transient/unsteady-state' have been used in this thesis to indicate results obtained by solving the original non-linear governing equation by numerical method. These numerical solutions are time dependent and cover both transient (initially) and steady-state (finally) vibration.

Experimental issue of SS shaft whirling is discussed in section 4.7.

Mathematical model that is developed in section 3.5 is used to obtain bending moment (M) vs. Δ and reduced modulus (E_r) vs. Δ curves. In this research, actual stress-strain curve of superelastic shape memory alloy (SMA) shaft of diameter of 2 mm (Figure 3.5b) obtained by Rahman (2001), is used to find the $E_r - \Delta$ (Figure 4.1) and M

– Δ (Figure 4.2) relations. These relations are used to include material non-linearity issue of the whirling shaft in Section 4.3.

4.2 Analysis of Steady-state Whirl of Jeffcott Rotor (Superelastic SMA Shaft)

This section deals with linearly elastic shaft material of Jeffcott Rotor that whirls as a single degree of freedom system (SDOFS). Equation 3.4.12 is solved to obtain non-dimensional whirling amplitude (r/e). Using Equation 3.4.15, non-dimensional dynamic force (P_d/mg) acting at the midpoint of the shaft is found out. Non-dimensional whirling amplitude and non-dimensional dynamic force acting on the disc center are found to be dependent on spin ratio (β), whirl speed ratio (λ) and the damping ratio (ξ).

Steady-state exact results are obtained for following specifications of the shaft:

Shaft length (L) = 200 mm, shaft dia (d) = 2 mm, disc mass, (m) = 300 g, modulus of

elasticity (E) = 65 GPa, linearly elastic bending stiffness of the shaft ($k = 48EI/L^3$) = 306.31 N/m, eccentricity of disc mass (e) = 4.5 mm, natural frequency (ω_n) = 31.95 rad/s.

4.2.1 Synchronous Whirl Considering Linearly Elastic Materials

From Figure 4.3 non-dimensional whirling amplitude vs. spin ratio relation can be seen. It is observed that increased damping greatly reduces whirling amplitude (r/e). For ξ = 0.05, maximum whirling amplitude is 10 whereas in case of ξ = 0.5, maximum whirling amplitude is 1.09. In case of low damping ratio (0.05 & 0.1), high whirling amplitude is observed at spin ratio of unity, because of resonance. For large value of spin ratio, value of whirling amplitude (r/e) remains constant which is approximately equal to unity for any damping ratio. Theoretically, this point is verified in Appendix - A.

Non-dimensional dynamic force vs. spin ratio considering different damping ratio is also obtained (Figure 4.4). Here, it is observed that, for low damping ratio (0.05 and 0.1) at a spin ratio of around unity, forces are very high. However, for β > 1.414 forces

notably decrease. But in case of high damping ratio (0.3 and 0.5), up to β = 1.414, forces are minimum and after that it is increasing monotonously. It is because damping forces contribute more to the force (P_d) acting on the shaft.

Another interesting finding from Figure 4.4 is that all curves intersect each other for a specific value of spin ratio (β = 1.414). Theoretically, this point is verified in Appendix - B.

4.2.2 Asynchronous Whirl Considering Linearly Elastic Materials

Non-dimensional whirling amplitude (r/e) as a function of spin ratio for different whirl speed ratio are obtained as in Figures 4.5 - 4.11. From Figure 4.5, it is observed that at resonance, the maximum r/e for any whirl speed ratio is 10, the same for all cases, and it is theoretically proved in Appendix - C. Interestingly, resonance occurs at different spin ratio for different values of whirl speed ratio. Higher the whirl speed ratio, lower the value of spin ratio that corresponds to the maximum r/e. For example, from Figure 4.5, maximum r/e occurs at spin ratio of unity for whirl speed ratio of unity. Whereas, it occurs at spin ratio of 0.5 for whirl speed ratio of 2. Results of steady-state synchronous whirl are placed in the same Figures for comparison only. From Figures 4.5 - 4.8, same pattern of r/e can be seen though the damping ratio is different for each of the figure. But the maximum r/e decreases as the damping ratio increases. As for instance, Figure 4.5 shows that the maximum r/e is 10 for damping ratio of 0.05 but it is 5 and 1.62 for damping ratio of 0.1 and 0.3 in Figures 4.6 & 4.7, respectively.

From Figures 4.5 - 4.11, it is also observed that as spin ratio increases beyond resonance, r/e approaches to unity for any value of whirl speed ratio. Theoretically it is verified in Appendix - A.

Non-dimensional dynamic force (P_d/mg) is a function of damping ratio, whirl speed ratio and spin ratio. Any change in these quantities will change the amount of force acting on the shaft which will determine whether the shaft will be deformed beyond elastic limit or not. From Figures 4.12 - 4.18, it is observed that if the damping ratio is constant, then for any value of whirl speed ratio, maximum P_d/mg produced

during resonance is constant but it's occurring at different spin ratio. Moreover, increased damping reduces P_d/mg at a great extent thus keeping the shaft material linearly elastic. In Figure 4.12, maximum P_d/mg at resonance is 4.71 when the damping ratio is 0.05. But, it is 2.39 and 0.985 for corresponding damping ratio of 0.1 and 0.3, respectively (Figures 4.13 & 4.14). From Figure 4.15, where damping ratio is very high (0.5), for any value of whirl speed ratio, dynamic force is increasing with increasing spin ratio.

Another interesting observation can be noted from Figures 4.12 - 4.15. From Figure 4.12, when the damping ratio is quite low (0.05), dynamic force (P_d/mg) is low even at quite high spin ratio. But from Figures 4.13 - 4.15, as the spin ratio is increasing so does the dynamic force. This is because increased damping ratio contributes more to the total force (P) acting on the shaft centre.

For large values of whirl speed ratio and spin ratio, the total force (P) is very large (Figures 4.17 & 4.18) and may lead to inelastic deformation of the material. So careful choice of spin ratio, whirl speed ratio and damping ratio can keep the total force (P) acting on the shaft at a safe limit.

4.3 Steady-state Synchronous and Asynchronous Whirl Considering Material Non-linearity

As mentioned material non-linearity issue has been conveniently incorporated in terms of $\sigma - \varepsilon$ (Figure 3.5b), $E_r - \Delta$ (Figure 4.1) and $M - \Delta$ (Figure 4.2) relations for the shaft material.

Modulus of elasticity (E) of shape memory alloy material that is considered for this simulation is 65 GPa [Rahman (2001)]. From Figure 4.1, it is observed that $E_r = E = 65$ GPa up to $\Delta = 0.012$. Therefore, superelastic SMA shaft will exhibit linearly elastic behavior up to $\Delta = 0.012$. For $\Delta > 0.012$, E_r starts decreasing as material non-linearity effect starts and the stress applied on the shaft material exceeds elastic limit of the stress-strain curve (Figure 3.5b). So, material non-linearity effect indicates that the shaft undergoes strain which is no more proportional to stress. The lowest value of E_r that is

calculated is 16.9 GPa for a total strain of 0.226. In such a case the shaft will show less bending stiffness (as, $E_r << E$).

If $M - \varDelta$ curve (Figure 4.2) of shape memory alloy is analyzed, it can also be seen that, up to $\varDelta = 0.012$ bending moment curve is a straight line but after that it is increasing with a decreasing slope. And, bending moment is 0.3041 Nm corresponding to $\varDelta = 0.012$. So, if the bending moment is more than 0.3041 Nm, then shaft will exhibit material non-linearity effect. For this research, $M = 0.3041$ Nm, is termed as the *threshold bending moment* (bending moment after which shaft exhibits material non-linearity). This is because, if the value of $\varDelta$ is more than 0.012, shaft undergoes strain which is no more proportional to stress.

In Figure 4.2, the maximum bending moment is $M_f = 1.5$ Nm. According to linearly elastic model for the same bending moment corresponding elastic strain ($\varDelta_l$) will be only 0.059. But by considering material non-linearity effect, for the same intensity bending moment of $M_f = 1.5$ Nm, actual total strain is $\varDelta_f = 0.226$ as seen from Figure 4.2. This shows actual strain is much larger than assumed by linear elastic model. In turn, this point proves the necessity of taking into account the material non-linearity effect.

It should be mentioned here that upon unloading, SMA can recover large strain by virtue of super/pseudo elasticity through a hysteresis [Rahman (2001)]. Therefore, large deformation for SMA can be termed as non-linearly elastic deformation. However, conventional engineering material like stainless steel (SS) invariably shows large inelastic/plastic strain upon unloading due to material non-linearity effect [Rahman (2001)].

For analyzing effect of material non-linearity on a whirling shaft, moment vs. shaft length of a particular shaft is considered using shaft whirl parameters of section 4.1. With reference to Figure 4.12, the maximum value of non-dimensional dynamic force acting at the shaft center due to whirl is 4.71 and corresponding total force (P) acting at the shaft mid-span is 16.80 N. Therefore, corresponding maximum bending moment ($M = PL/4$) at the shaft center is 0.84 Nm, much more than the threshold value.

From the bending moment vs. shaft length diagram (Figure 4.19) of superelastic SMA shaft under consideration, length of the section from 0.0362 m to 0.1638 m is experiencing non-linearly elastic deformation because corresponding bending moment is higher than the threshold bending moment (0.3041 Nm). Corresponding value of Δ for threshold bending moment is 0.012. Corresponding strain ε_2 (compressive) is 0.005725 and strain ε_1 (tensile) is 0.006178. While, corresponding compressive stress from Figure 3.5b (non-linear $\sigma - \varepsilon$ curve of SMA shaft) is 362.81 MPa and tensile stress 389.42 MPa. The maximum compressive stress and tensile stress at shaft mid-span is 917.474 MPa and 606.542 MPa, respectively.

Range of spin ratio causing deformation beyond proportional limit can be determined from Figure 4.4. For example, threshold bending moment is 0.3041 Nm for β = 0.79 to 1.35. So, shaft should not be run within this range for prolonged period. Again, if high damping ratio is considered, shaft spin ratio greater than 1.73 is to be avoided to avoid deformation beyond elastic limit.

Whirling shaft's elastic curve can be known from M/EI vs. shaft length (Figure 4.20) considering material linearity as well as non-linearity effects. Since reduced modulus (E_r) is known, therefore, the term M/E_rI can be evaluated for any point on the shaft axis. Therefore, M/E_rI vs. shaft length is incorporated in Figure 4.20 to analyze the material non-linearity effect. Two theorems of area moment method (Appendix - D) are applied to evaluate the shaft's elastic curve. The maximum deflection of the shaft is an important point of concern. Figure 4.21 shows the predicted shapes of the shaft considering linearly elastic as well as non-linearly elastic shaft materials. Maximum deflection at shaft mid-span considering the material as linearly elastic is 54.9 mm but it is 127.8 mm when material non-linearity is considered (Figure 4.21).

4.4 Effect of Reduced Modulus (E_r) on Jeffcott Rotor's Natural Frequency (ω_n)

Points on the shaft will have different bending moments when it is whirling. When bending moment at any point along the shaft length exceeds the threshold bending moment, corresponding Young's modulus will be lower than that for initial linearly elastic model (Figure 4.1). As a whole, the resultant bending stiffness (k) will decrease. But, natural frequency depends on k as explained below,

$$\delta \text{ (shaft deflection)} = \frac{PL^3}{48EI}$$

$$\text{Therefore, } k = \frac{P}{\delta} = \frac{48EI}{L^3} \text{ and, } \omega_n = \sqrt{\frac{k}{m}} = \sqrt{\frac{48EI}{mL^3}}$$

For $\lambda = 1$, resonance occurs when $\omega = \omega_n$. As E reduces to E_r, therefore ω_n will also reduce to $\sqrt{\frac{48E_rI}{mL^3}}$. Obviously, resonance will occur at a lower speed than that expected by linearly elastic model.

4.5 Analysis of Steady-State Synchronous & Asynchronous Whirl of Jeffcott Rotor (Stainless Steel Shaft)

Exact theoretical results (Figures 4.22 – 4.30) are obtained for non-dimensional whirling amplitude (r/e) and non-dimensional dynamic force (P_d/mg) acting on the shaft center as a function of spin ratio (β), whirl speed ratio (λ) and damping ratio (ξ).

Specifications of the stainless steel shaft are as follows:

Shaft length, $L = 890$ mm, shaft diameter, $d = 8$ mm, disc mass, $m = 300$ g, modulus of elasticity, $E = 202$ GPa, linearly elastic bending stiffness, $k = 2765.365$ N/m, eccentricity of disc mass, $e = 4.5$ mm, natural frequency, $\omega_n = 96.01$ rad/s.

Here, value of eccentricity of disc mass (e) is chosen by comparing it with the diameter of circular disc to keep it realistic. Shaft's linearly elastic bending stiffness (k) is calculated using the formula $[k = \left(\frac{48EI}{L^3}\right)]$.

4.5.1 Analysis on Synchronous Whirl

From Figure 4.22, it is observed that increased damping ratio greatly reduces r/e. For $\xi = 0.05$, maximum r/e is 10 whereas in case of $\xi = 0.5$, maximum r/e is 5. In case of low damping ratio (0.05 & 0.1), high r/e occurs at a spin ratio of unity, because of resonance. However, for large value of spin ratio, value of r/e approaches to unity for any damping ratio. Since, results are presented in non-dimensional form, r/e vs. β Figures are similar for superelastic SMA shafts and stainless steel shafts.

P_d/mg vs. β curves considering different damping ratio are shown in Figure 4.23. Here, it is observed that, for spin ratio of around unity, for low damping ratio like 0.05 and 0.1, maximum P_d/mg is very high (42.495 and 21.561, respectively). But for $\beta > 1.414$ forces notably decrease. In case of high damping ratio, 0.3 and 0.5, P_d/mg increases monotonously.

From Figure 4.23, all P_d/mg vs. β curves intersect each other for a particular value of spin ratio ($\beta = 1.414$) similar to the case of SMA shaft (Figure 4.4).

4.5.2 Analysis of Asynchronous Whirl

r/e vs. β Figures of stainless steel for different whirl speed ratio and damping ratio are skipped here. This is because results are exactly same as respective Figures of steady-state asynchronous whirl of shape memory alloy shaft (Figures 4.5 - 4.11). This is because value of r/e is governed by damping ratio, spin ratio and whirl speed ratio.

P_d/mg vs. β Figures as a function of damping ratio, whirl speed ratio and spin ratio (Figures 4.24 - 4.30) are obtained for stainless steel shaft. These Figures show similar pattern as in Figures 4.12 - 4.18 for shape memory alloy shafts. The only difference is magnitude of dynamic forces (P_d/mg) of SS shaft is comparatively larger

than SMA shaft as the physical and geometrical parameters are different for two types of shafts.

4.6 Analysis of Unsteady-state Whirl of Jeffcott Rotor

In this chapter, firstly, the validation of the code is done in section 4.6.1. Next, transient vibration results are presented for SMA and SS shafts.

4.6.1 Code Validation

A solved problem from Thomson et al. [2011] is simulated by using the code developed for this thesis. Statement of the problem: if, critical speed ω_n to be reached with an initial whirl amplitude for a shaft which is undergoing synchronous whirl with zero damping, then amplitude builds up linearly (Appendix - F).

Following initial boundary conditions (at $t = 0$ s) are chosen randomly as shown below:

Whirl amplitude (r) = 1 mm, radial velocity ($\dot{r}$) = 100 mm/s, angular displacement

(θ) = 0 rad, whirling speed ($\dot{\theta}$) = 0 rad.

Above chosen initial conditions are used in subsequent chapters. Other specifications for the code validation are same as previously stated in section 4.2. Disc mass of (300 g and 400 g) are considered for these simulation. Corresponding natural frequencies are 31.95 and 27.67 rad/s, respectively. From Figure 4.31 (for disc mass = 300 g), it is observed that amplitude is building up linearly which exactly matches with the results in Thomson et al. (2011) (Appendix – F). Simulation with 400 g disc mass shows similar result, which is not shown here for the sake of brevity. So, soundness of the matlab code is proven partially. More such proofs will be shown in subsequent discussion of results.

4.6.2 Transient Vibration of Superelastic SMA Shaft

SMA shaft specifications considered for this section are as that of section 4.2. Additionally, different eccentricity of disc mass (e) = 4.5, 11, 20, 25, 30 mm are considered. And boundary conditions are same as stated in section 4.6.1.

It should be mentioned here that the terms 'results or, solutions of transient/unsteady-state' have been used in this thesis to indicate results obtained by solving the original non-linear governing equation by numerical method. However, these numerical solutions are time dependent and contain both transient (initially) and steady-state (finally) vibration. For example, from Figures 4.32 - 4.36, it can be seen that, shafts show transient vibration up to specific time (transient period). As transient period diminishes, r/e approaches a constant value for the rest of the time indicating steady-state period of vibration. However, transient vibration pattern is different for different values of β.

For better understanding of transient phenomena during whirling, r/e vs. β curve is presented in (Figure 4.37). To construct such Figure, maximum values of previous $\frac{r}{e}vs.t$ curves (Figures 4.32 - 4.36) are taken and corresponding r/e vs. β curve for different damping ratio is constructed (Figure 4.37). It is observed form Figure 4.37 that, increased damping ratio reduces r/e greatly but eventually it increases as the spin ratio increases.

Some fundamentally 2DOFS behave as a SDOFS. As for instance, Houdaille damper, a 2DOFS, exhibits a single resonant speed [Thomson et. al. (2011)]. Similarly, original Jeffcott rotor system is a 2DOFS in r and θ. So, there should be two resonant speeds and 2 distinct peaks should appear in r/e vs. β (Figure 4.37) curve. However, Figure 4.37 shows a single peak corresponding to resonance at $\beta = 1$.

If Figure 4.3 (based on steady-state assumption) and Figure 4.37 (based on unsteady– state assumption) are compared, it is seen that at resonance ($\beta = 1$), r/e assumes a distinct peak value for $\xi = 0.05$ and 0.1. Interestingly, the peak value is almost equal for both steady-state and transient vibration cases. In turn, it proves soundness of

the entire scheme because steady-state solutions are exact and transient solutions are obtained by numerical method. However, beyond resonance steady-state solution approaches unity for large value of β while transient solutions go on increasing.

For understanding steady-state phenomena from results of transient vibration, r/e vs. β curve is presented in (Figure 4.38). To construct such Figure values of r/e at apparently steady-state period from previous r/e vs. t curves (Figures 4.32 - 4.36) are taken and corresponding r/e vs. β curve (Figure 4.38) for different damping ratio is constructed. If Figure 4.3 (exact solutions based on steady-state assumption) and Figure 4.38 (results obtained by numerical method and without any steady-state assumption) are compared, they show very good match which again prove the soundness of the numerical scheme.

Effect of ξ and e on whirl amplitude (r) can be visualized from Figures 4.39 - 4.42. At resonance distinct peaks are seen for low damping (Figures 4.39 & 4.40). Peaks at resonance disappear with increasing damping (Figures 4.41 & 4.42). In all cases r increases with β. Also increased value of e increases r.

Figures 4.43 & 4.44 show $\dot{\theta}$ & $\dot{r}$ respectively during transient vibration. In Figure 4.45, dynamic force (P_d) for transient vibration is calculated adding radial restoring force (kr) and radial damping force ($\dot{c}r$) and tangential damping force ($cr\dot{\theta}$) at the same instant. The time at which r becomes the maximum is recorded and at the same instant $\dot{r}$ and $\dot{\theta}$ are known from Figures 4.43 & 4.44, respectively. Next, two damping forces are evaluated and finally, Figure 4.45 is constructed. In Figure 4.45, maximum P_d is 13.8 N and corresponding force P is 16.8 N. Since corresponding moment at shaft mid-span exceeds the threshold value, it will exhibit material non-linearity effect.

4.6.3 Transient Vibration of Stainless Steel Shaft

Stainless steel shaft specifications are stated in section 4.5. However, different eccentricity of disc mass (e) = 4.5, 11, 20, 25 & 30 mm are considered. The boundary conditions are same as stated in section 4.6.1.

From Figures 4.46 - 4.50, it can be seen that, shafts show transient vibration up to specific time (transient period). As transient period diminishes, *r/e* approaches a constant value for the rest of the time indicating steady-state vibration. However, transient vibration pattern is different for different values of *β*.

Using Figures 4.46 - 4.50, *r/e* vs. *β* curves in Figure 4.51 is obtained following the same procedure that is used to obtain Figure 4.37 for superelastic SMA shaft. It is observed that increased damping ratio greatly reduces *r/e* but eventually it increases with the *β*. The pattern is similar to that of SMA shaft (Figure 4.37). Interestingly, the maximum *r/e* at resonance are same for both SMA and SS shafts if same values of eccentricity, damping ratio and spin ratio are considered. However, for spin ratio other than unity *r/e* will be different during transient vibration.

Steady-state *r/e* vs. *β* curve (Figure 4.52) from *r/e* vs. *t* curves (Figures 4.46 - 4.50) is obtained following the same procedure that is followed in case of superelastic SMA shaft (Figure 4.38). If, Figure 4.22 (based on steady-state assumption) and Figure 4.52 (steady-state results obtained from numerical solution) are compared, they show excellent match which again prove the validity of the entire mathematical scheme. P_d/mg vs. *β* (Figure 4.53) shows pattern similar to that of superelastic SMA shaft (Figure 4.45). From Figure 4.53, the maximum stress is 553.59 MPa (corresponding to resonant amplitude for $\xi = 0.05$ and considering linearly elastic model). Though threshold bending moment of SS is not available, the stress corresponding to resonant amplitude is so high that it is likely to cross elastic limit of commercially available SS. This point is evident from experiment.

4.7 Experiment

4.7.1 Experimental Set-up

A set-up made of MS plate with a 0.5 hp Single Phase AC motor, is constructed mainly to demonstrate whirling of shaft. Secondly, inelastic deformation of shaft material (material non-linearity effect) can also be demonstrated from experiment. The setup is shown in Figures 4.54 and 4.55. Shaft material chosen for this experimental demonstration is stainless steel with following parameters.

Shaft length, L = 890 mm, diameter, d = 6 mm & 8 mm, disc mass, m = 250 g

(Figure 4.56), modulus of elasticity, E = 202 GPa, linearly elastic bending stiffness

of the shaft material $k = \frac{48EI}{L^3}$ = 874.98 N/m for (shaft dia = 6 mm), 2765.37 N/m for

(shaft dia = 8 mm).

4.7.2 Observation from Experiment

The stainless steel shafts with different diameters are used to perform the experiment and to observe the response at different shaft speed. Here damping ratio is practically very low because only air is providing the opposing force. Whether the shaft is deformed inelastically during whirling can be observed from Figures 4.57 - 4.60. Theoretically, this point of elastic or inelastic deformation can be explained with the help of load-spin ratio curve as shown in Figure 4.53 together with the threshold bending moment for experimental shaft material. Unfortunately, because of unavailability of proper instrument, the stress-strain ($\sigma - \varepsilon$) curve and hence the $M - \Delta$ and $E_r - \Delta$ relations could not be obtained for the experimental shaft material (SS). As a result the threshold bending moment could not be calculated. Hence, an 'imaginary' threshold bending moment is assumed to explain inelastic shaft deformation due to large amplitude whirl of the SS shaft.

During experiment, when the shaft (dia = 8 mm, disc mass = 250 g) is run at a low speed 253 rpm (ω_n = 1004.33 rpm, β = 0.25), the corresponding shaft whirl was very low. Less vibration and less whirling amplitude are observed from the experiment. After the rotation, shaft straightness didn't change which shows elastic recovery (Figure 4.57). This point can be explained following Figure 4.53 considering ξ = 0.05 (low damping, comparable to experiment). At β = 0.25, corresponding (r/e) = 0.32, r = 1.45 mm, P_d/mg = 1.36 N and M = 0.89 Nm. Here, bending moment (M = 0.89 Nm) is assumed to be less than threshold bending moment. As a result, the shaft shows elastic recovery (Figure 4.57).

Similarly, following Figure 4.53, for ξ = 0.05 and β = 1.13 (in the vicinity of resonance), shaft dia = 8 mm, corresponding (r/e) = 5.92, r = 26.63 mm, P_d/mg = 30.2 and therefore, M = 19.78 Nm. The maximum stress is 553.59 MPa (considering linearly elastic model). Though threshold bending moment of SS is not available, the maximum stress (553.59 MPa) corresponding to resonant amplitude is so high that it is likely to cross elastic limit of commercially available SS. This point is evident from experiment showing inelastic deformation of the test piece (Figure 4.58). So, it can be claimed that the numerical result shown in Figure 4.53 is indirectly validated by experimental results as in Figure 4.58.

Figure 4.59 shows the test piece is deformed. Following Figure 4.53, for ξ = 0.05 and β = 2.29, shaft dia = 8 mm, corresponding (r/e) = 3.6, r = 16.19 mm, P_d/mg= 18.36, M = 12.02 Nm. Here, bending moment is greater than threshold bending moment leading to inelastic deformation (Figure 4.59).

Similarly, Figure 4.60 shows the test piece is deformed. For ξ = 0.05 and β =0.94, shaft dia = 6 mm, corresponding (r/e) = 6.48, r = 29.14 mm, P_d/mg = 10.44, M = 6.84 Nm. Here, bending moment must be greater than threshold bending moment again leading to inelastic deformation (Figure 4.60).

CHAPTER 5
CONCLUSIONS AND RECOMMENDATIONS

Response of a shaft has been analyzed comprehensively considering effect of material non-linearity and all practically possible modes of whirl of a Jeffcott rotor due to eccentricity of mass. Soundness of the developed mathematical scheme and computer code has been amply demonstrated. Chapter wise, following salient conclusions can be drawn at the end of research.

5.1 Steady-State Synchronous & Asynchronous Whirl of Jeffcott Rotor

It is found that increased damping greatly reduces whirling amplitude (r/e). For any damping ratio, maximum r/e is occurred at spin ratio of unity, because of resonance. However, for large value of spin ratio, value of r/e approaches to unity.

Interestingly, all P_d/mg vs. β curves intersect each other for a specific value of spin ratio $\beta = 1.414$. Shaft response is notably different on two sides of the intersecting point.

As far as asynchronous whirl is concerned, interestingly, resonance is taking place at different spin ratio for different values of whirl speed ratio. Higher the whirl speed ratio, lower the value of spin ratio that corresponds to the maximum r/e.

5.2 Steady-state Whirl Considering Material Non-linearity

Material non-linearity issue is incorporated in terms of $\sigma - \varepsilon$, $M - \Delta$ and $E_r - \Delta$ relations for the shaft material. It is found that when whirl amplitude is large enough actual strain is much larger than assumed by linear elastic model. Also modulus of elasticity decreases significantly as strain increases.

As material non-linearity is taken into account, some portion of the shaft is found to experience stresses (different magnitude in tension and compression) beyond proportional limit. For a particular SMA shaft, the maximum deflection at shaft center considering the material as linearly elastic is 54.9 mm but it is 127.8 mm when material non-linearity is considered. Another important point is that, resonance will occur at a lower speed than that expected by linearly elastic model.

5.3 Unsteady-state Whirl of Jeffcott Rotor

If r/e vs. β Figure obtained from both steady-state and unsteady-state assumption are compared, it is seen that at resonance ($\beta = 1$), r/e assumes a distinct peak value if ξ is kept low. Interestingly, the peak value is almost equal for both exact solutions (steady-state results) and transient vibration results. In turn, it proves soundness of the entire scheme because steady-state solutions are exact and transient solutions are obtained by numerical method. However, beyond resonance steady-state solution approaches unity for large value of β while transient solutions go on increasing. Beyond resonance, r increases with β. Also increased eccentricity e increases r. Peaks at resonance disappear with increasing damping ratio.

5.4 Experiment

Stainless steel shafts with different diameters are used to perform the experiment and responses at different shaft speeds are observed. Whether the shaft is deformed inelastically during whirling are observed from photographs. These points of elastic or, inelastic deformations can be explained in terms of threshold bending moment and theoretical/numerical results obtained in this thesis.

5.5 Recommendations for Future Work

The following recommendations can be made for future works based on the experience gained while achieving the set objectives of this thesis.

(1) Jeffcott Rotor shafts' cross-sections are not always perfectly circular due to manufacturing imperfections. Effect of imperfect cross-sections on whirling can be considered in future studies.

(2) More experimental studies with sophisticated instrumentation can be carried out to verify the results obtained from numerical analysis from this thesis.

(3) In this study, whirling has been considered only due to mass eccentricity. Other factors (for example, gyroscopic effect, unbalanced centrifugal forces, elastic hysteresis of shaft material etc.) can be considered for further analysis.

(4) Simply supported end-conditions of the shafts have been considered here. Different boundary conditions can be considered for further analysis.

(5) Resonance speed will change due to material non-linearity. This point can also be explored in future.

(6) Because of unavailability of proper instrument, the stress-strain ($\sigma - \varepsilon$) curve and hence the $M - \Delta$ and $E_r - \Delta$ relations could not be obtained for the experimental shaft material (SS). As a result the threshold bending moment could not be calculated. Next study can address this point rigorously to explain inelastic shaft deformation due to large amplitude whirl of the shaft.

REFERENCES

[1] Ankit, J.D., Devendra, A.P., Pranav, B.P. (2014), "Analysis of whirling speed and Evaluation of self-excited motion of the rotating shaft," IJESRT, ISSN:2277-9655: pp.784-787.

[2] Crocker M. J., (1998), "Handbook of Acoustics", John Wiley & Sons, Inc.

[3] Farrissey L., (2004) "Metal Shafts: Designs To Meet The Required Performance",
Galway, Ireland, Creganna Medical Devices.

[4] Keshav B. T. (2014), "Experimental Investigation of Shafts on Whirling of Shaft Apparatus", International Journal of Science, Engineering and Technology Research (IJSETR), Volume 3, Issue 8.

[5] Kokame Z., Katase A., Yano S., (1950),"On The Whirling of Rotating Shaft at High Rotational Speed." Text version. http://hdl.handle.net/2433/74158.

[6] Kolenda J. Marynarki A. W., (2012), "Whirling of Asymmetric Shaft Under Constant Lateral Force", ROK LIII NR 3 (190).

[7] Nelson M., (2007), "Rotor dynamics without equations." International Journal of COMADEM, 10(3), pp. 2-10.

[8] Pradeep, M., Jog, C.S., Anindya, C., "Modal projections for synchronous rotor whirl, "Proc. R. Soc. A (2008) 464, 1739-1760.

[9] Rahman, M. A., (2001), "Behavior of Superelastic SMA Columns Under Compression and Torsion." Ph.D. Thesis, Tohoku University, Sendai, Japan, 2001.

[10] Rahman, M. A., Kowser, M. A. (2007), "Nonlinear analysis of cantilever shape memory alloy beams of variable cross-section". Smart Materials & Structures (IOP Publishing Ltd., UK) 16, pp. 531-540.

[11] Rahman, M. A., Akanda, S. R., Hossain, M. A. (2008), "Effect of cross-section geometry on the response of an SMA column". Journal of Intelligent Material Systems and Structures (SAGE Publications, UK), Feb 2008: vol. 19pp.243-252.

[12] Rahman M. A. and Kowser M.A., (2009), "Inelastic deformations of stainless steel leaf springs-experiment and non-linear analysis," Meccanica, no. DOI 10.1007/s11012-009-9270-7.

[13]   Rajiv T., (2014), "Jeffcott Rotor Model", Theory & Practice of Rotor dynamics(Web), NPTEL, http://nptel.ac.in/courses/112103024/4.

[14]   Rajiv T., (2017), "Rotor Systems: Analysis and Identification", Taylor & Francis.

[15]   Rao, S.S. (2012), Mechanical Vibrations, Miami: Pearson Education, Inc.

[16]   Romberg, W. (1955), "Vereinfachte numerische Integration", Det Kongelige Norske Videnskabers Selskab Forhandlinger, Trondheim, 28 (7): 30–36.

[17]   Shyoung J. W., Tang F. L., Shaw H. J. (2014), "Analytical Solution for Whirling Speeds and Mode Shapes of a Distributed-Mass Shaft With Arbitrary Rigid Discs", J. Appl. Mech 81(3), 0345031–03450310, doi: 10.1115/1.4024670.

[18]   Swanson E., Powell C. D., Weissman S.,"A Practical Review of Rotating Machinery Critical Speeds and Modes." Sound & Vibration 2005.

[19]   Thomson W.T., Dahleh M.D., Padmanabhan, C., (2011), "Theory of Vibration with Applications", Pearson Education, Inc.

[20]   Timoshenko S., (1955), "Vibration Problem in Engineering", Third edition.

[21]   Timoshenko S., (1956)," Strength of Materials, Part II, Advanced Theory & Problems", Third Edition, D. Van Nostrand Company, Inc.

[22]   Yoon, S.Y., Lin, Z., Allaire, P.E. (2013), "Control of Surge in Centrifugal Compressors by Active Magnetic Bearings, Theory and Implementation", (XXI), 275 P., Springer.com/978-1-4471-4239-3.

[23]   Whalley R. Ameer A. A., (2009), "Whirling Prediction With Geometrical Shaft Profiling", Elsevier, Volume 33, Issue 7, pp. 3166-3177.

FIGURES
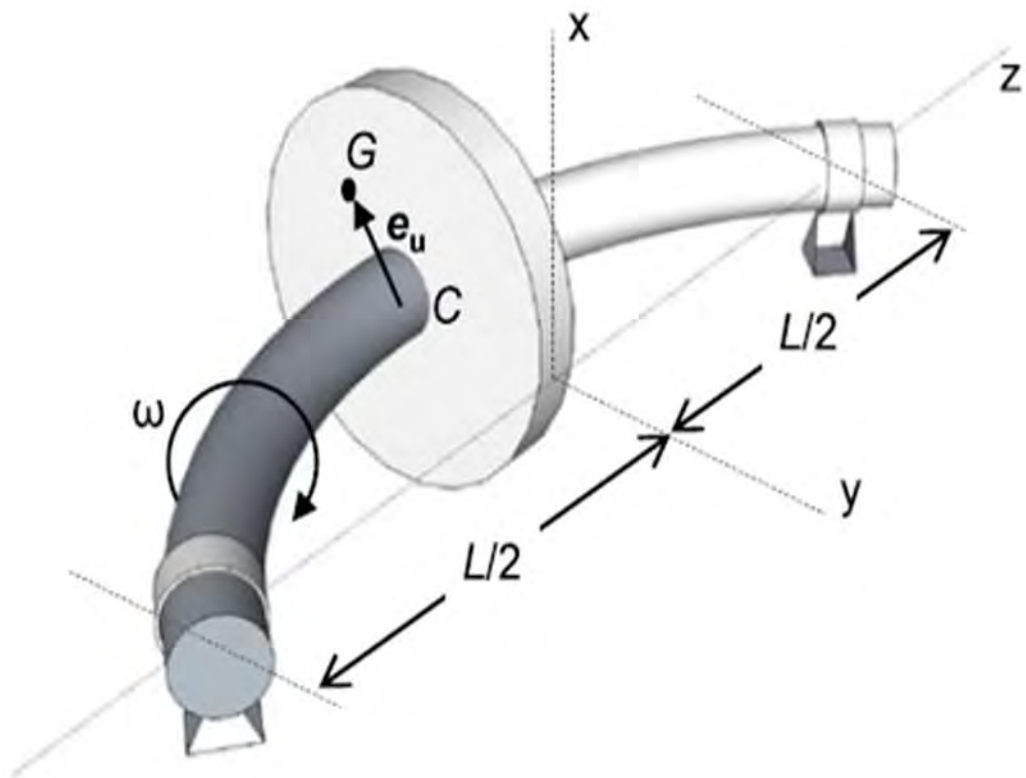
Figure 1.1: Jeffcott rotor model.
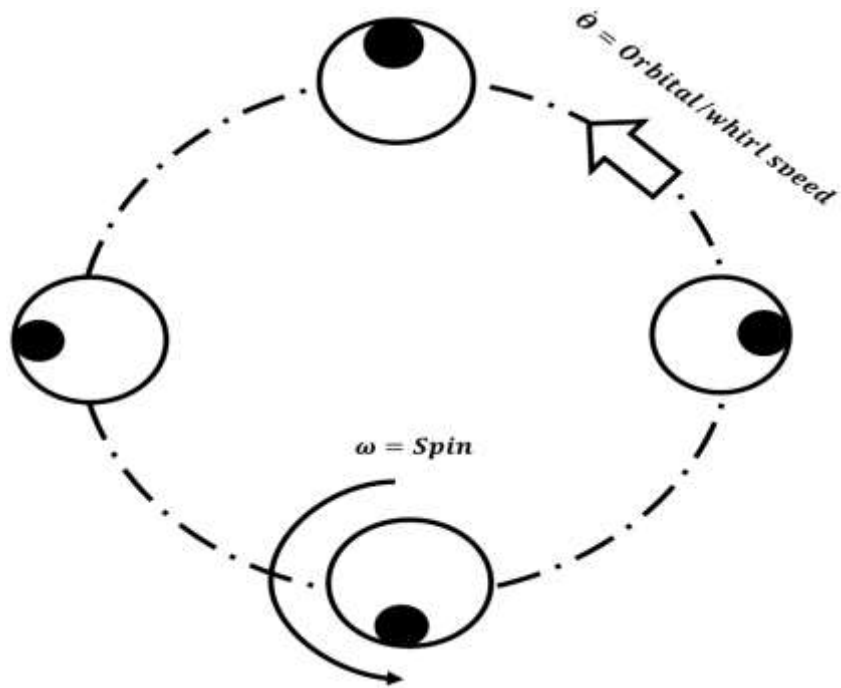
Figure 1.2: Definition of whirl parameters. Whirl speed ratio, $\lambda = \dfrac{\dot{\theta}}{\omega}$, $\lambda = 1$ for synchronous whirl, $\lambda \neq 1$ for asynchronous whirl.
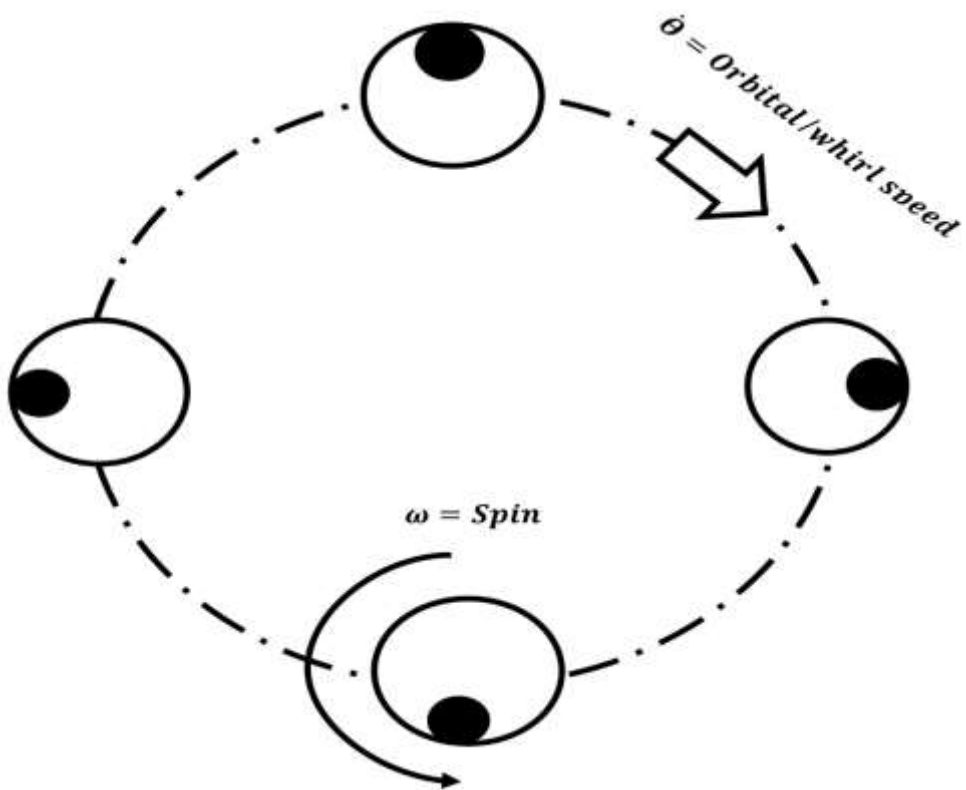
Figure 1.3: Anti-synchronous whirl $\left(\lambda = \dfrac{\dot{\theta}}{\omega} = -1 \right)$.
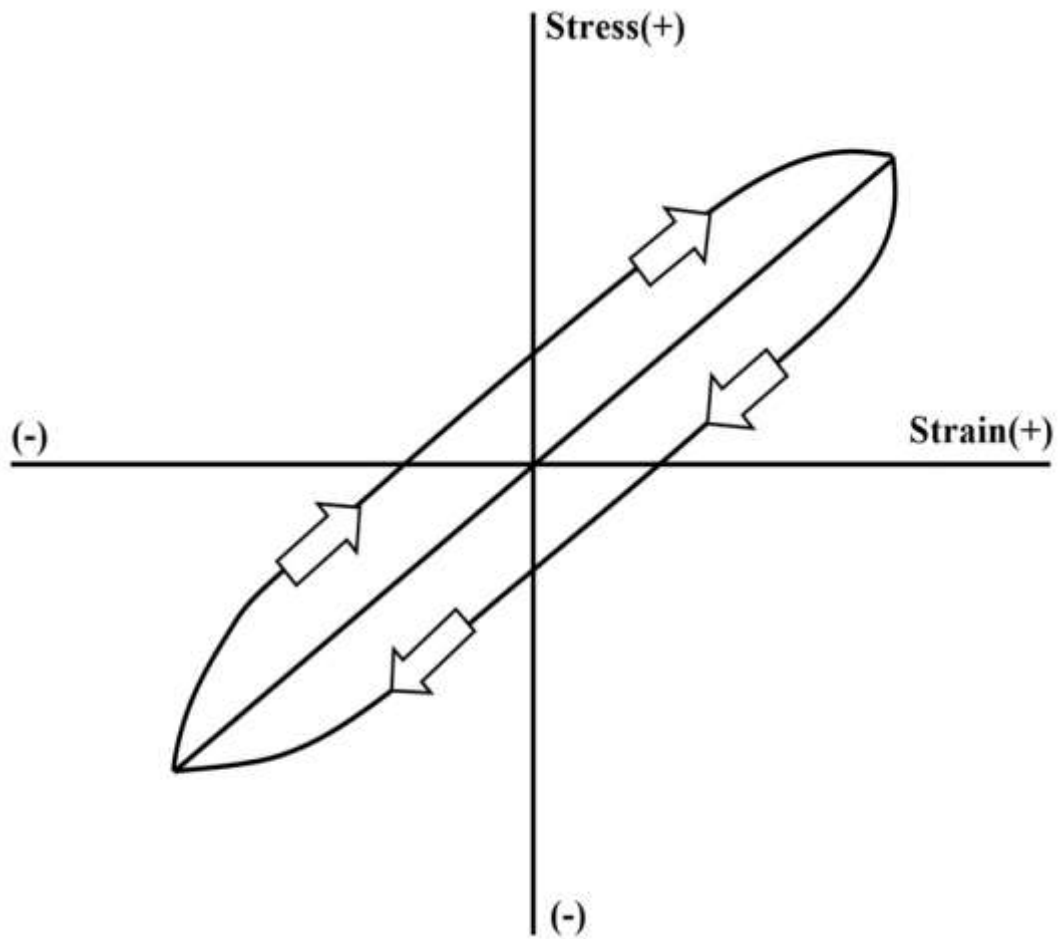
Figure 1.4: Stress-strain diagram for material possessing elastic hysteresis characteristics.
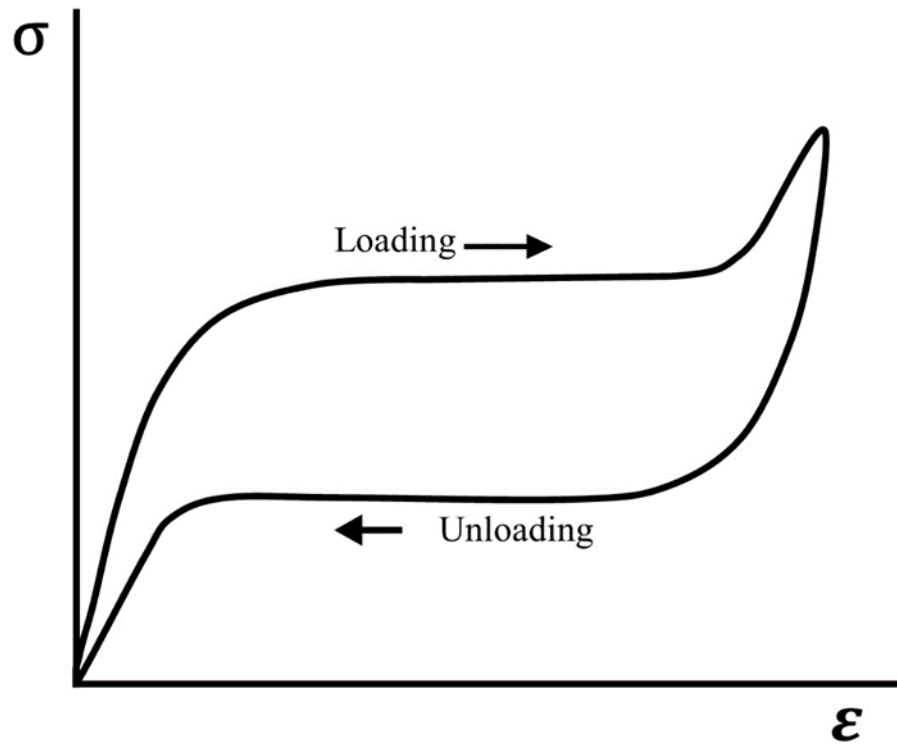
Figure 1.5: Fictitious stress-strain curve showing superelastic SMA's shape and size recovery through a nonlinear hysteresis.
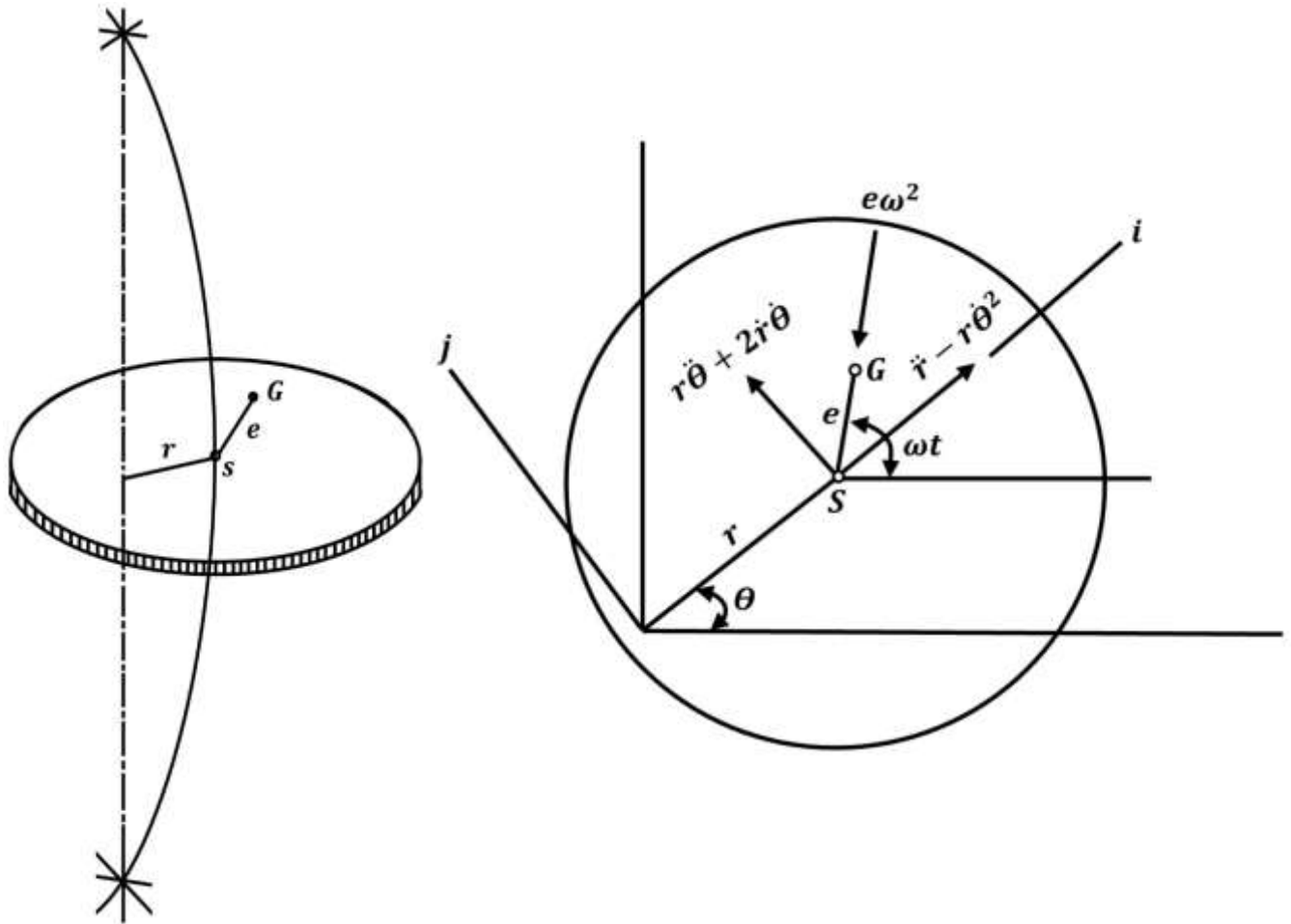
Figure 3.1: Whirling of rotating shaft [Thomson et al. (2011)].
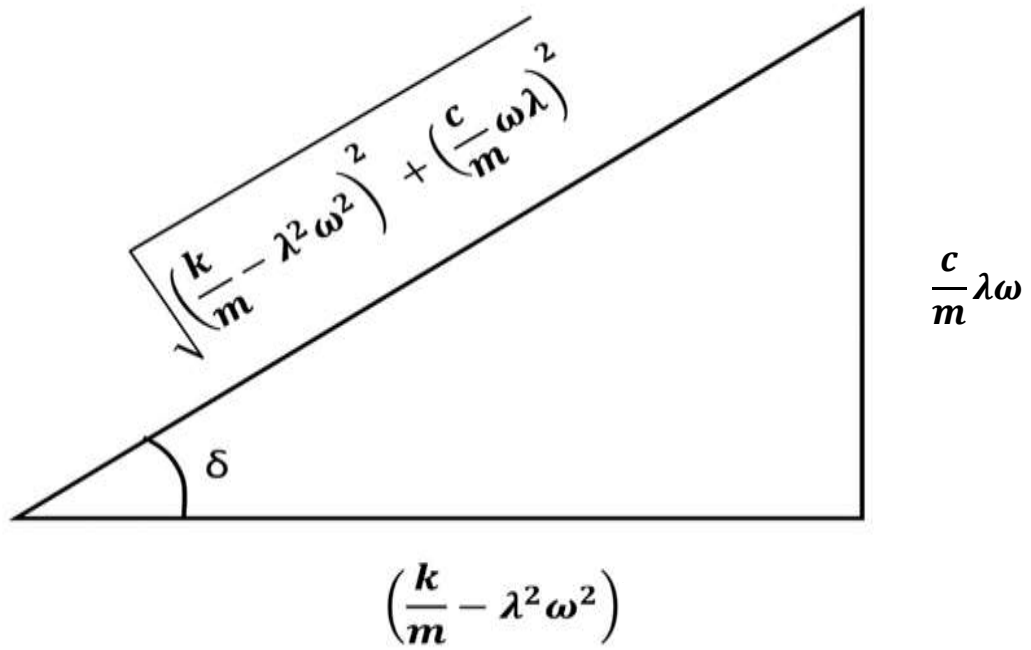
Figure 3.2: Vector triangle of forces acting on the shaft for steady-state whirl.
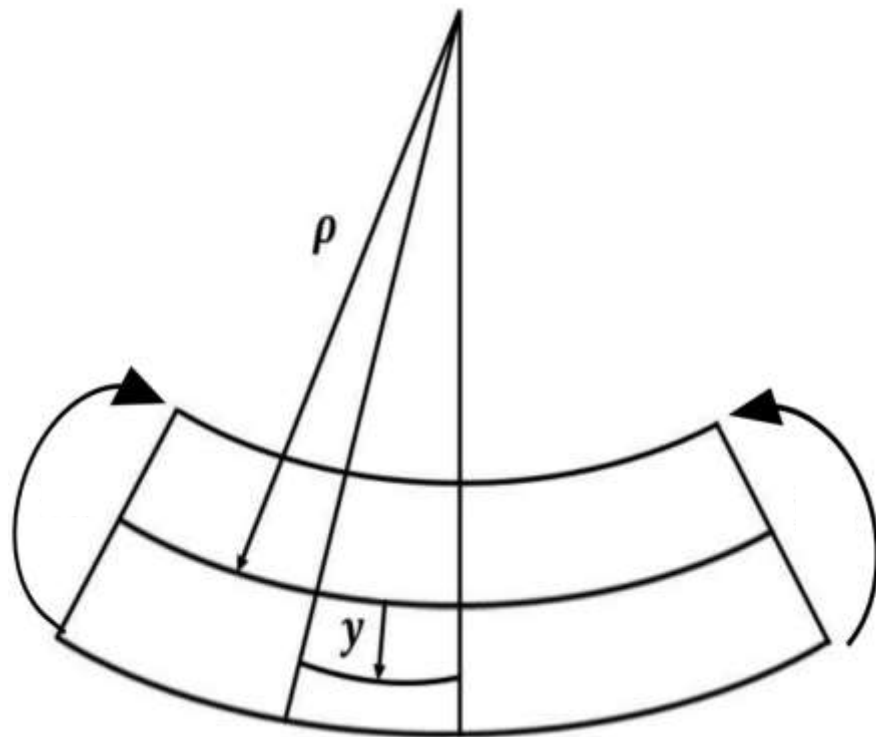
Figure 3.3: Bending of the shaft.
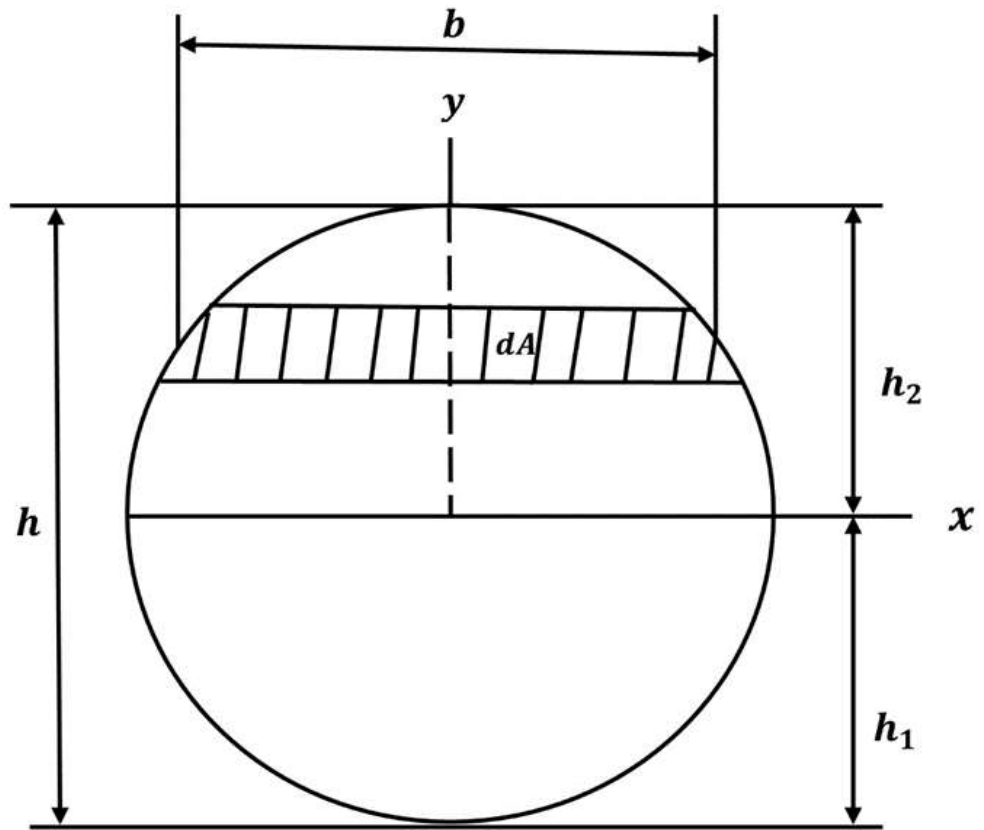
Figure 3.4: Circular cross-section of the shaft.
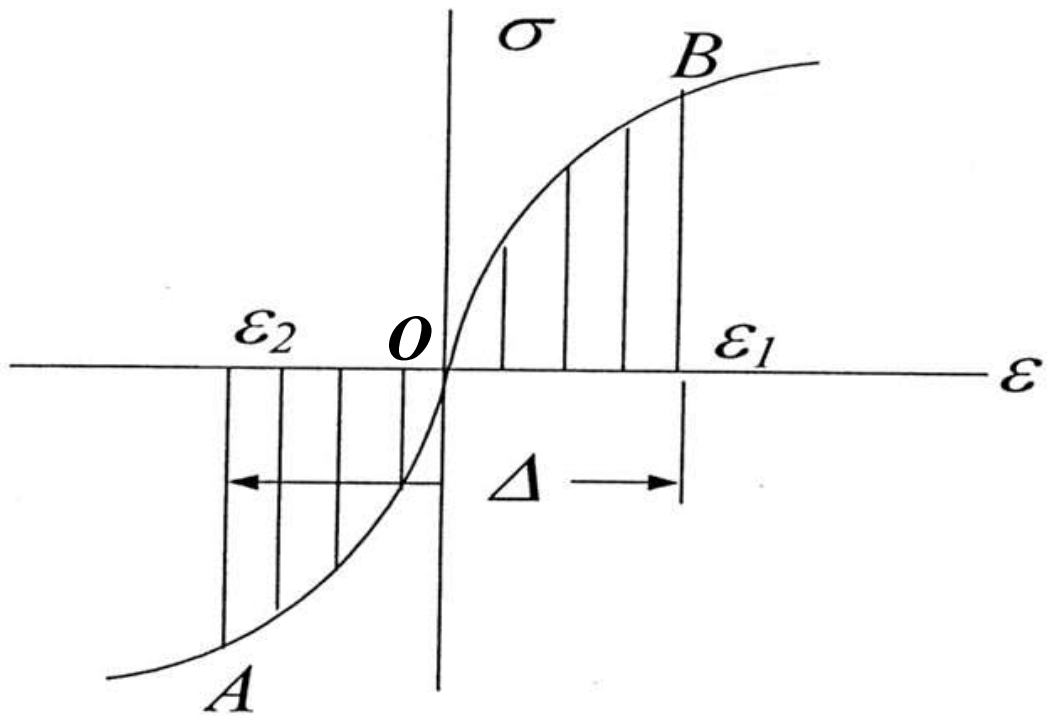
Figure 3.5a: Fictitious non-linear $\sigma - \varepsilon$ curve under tension & compression showing material non-linearity.
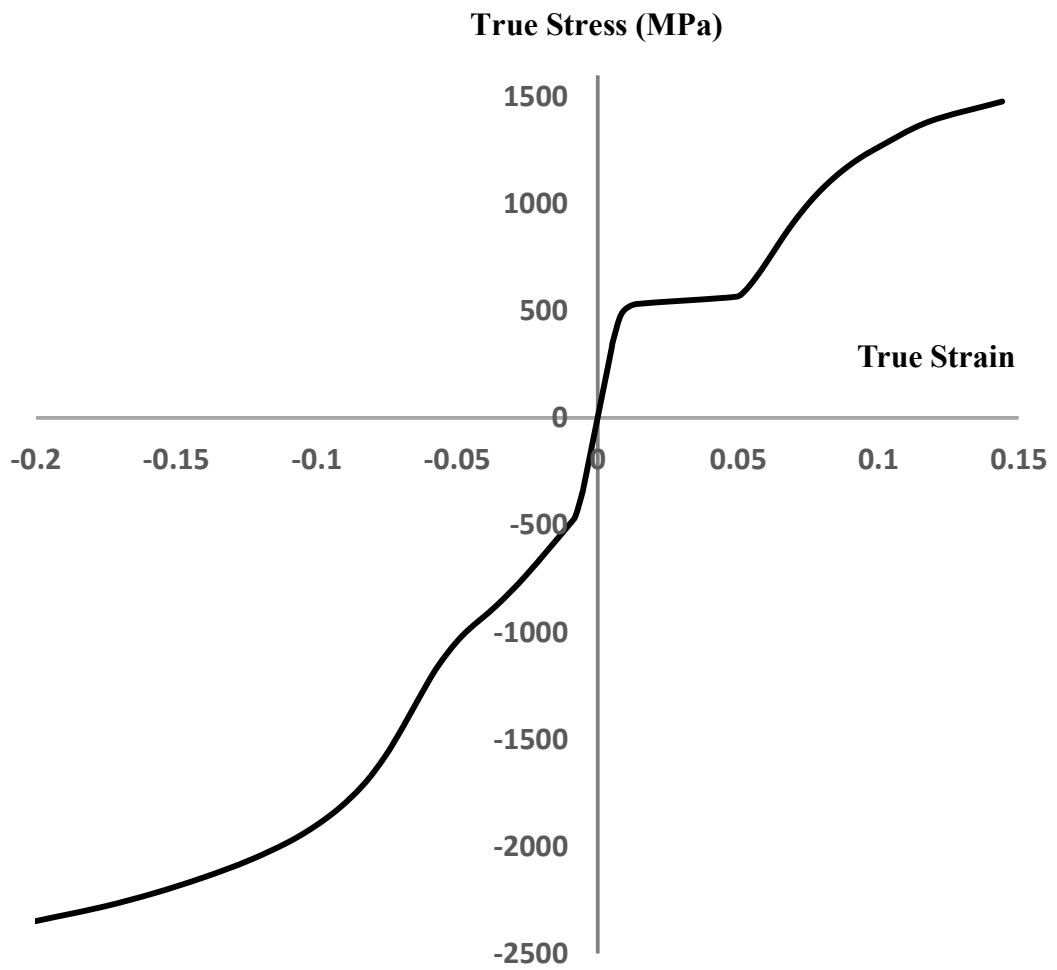
Figure 3.5b: Actual stress-strain curve of superelastic SMA (dia = 2 mm), showing asymmetric behavior in tension and compression [Rahman, M. A. (2001)].
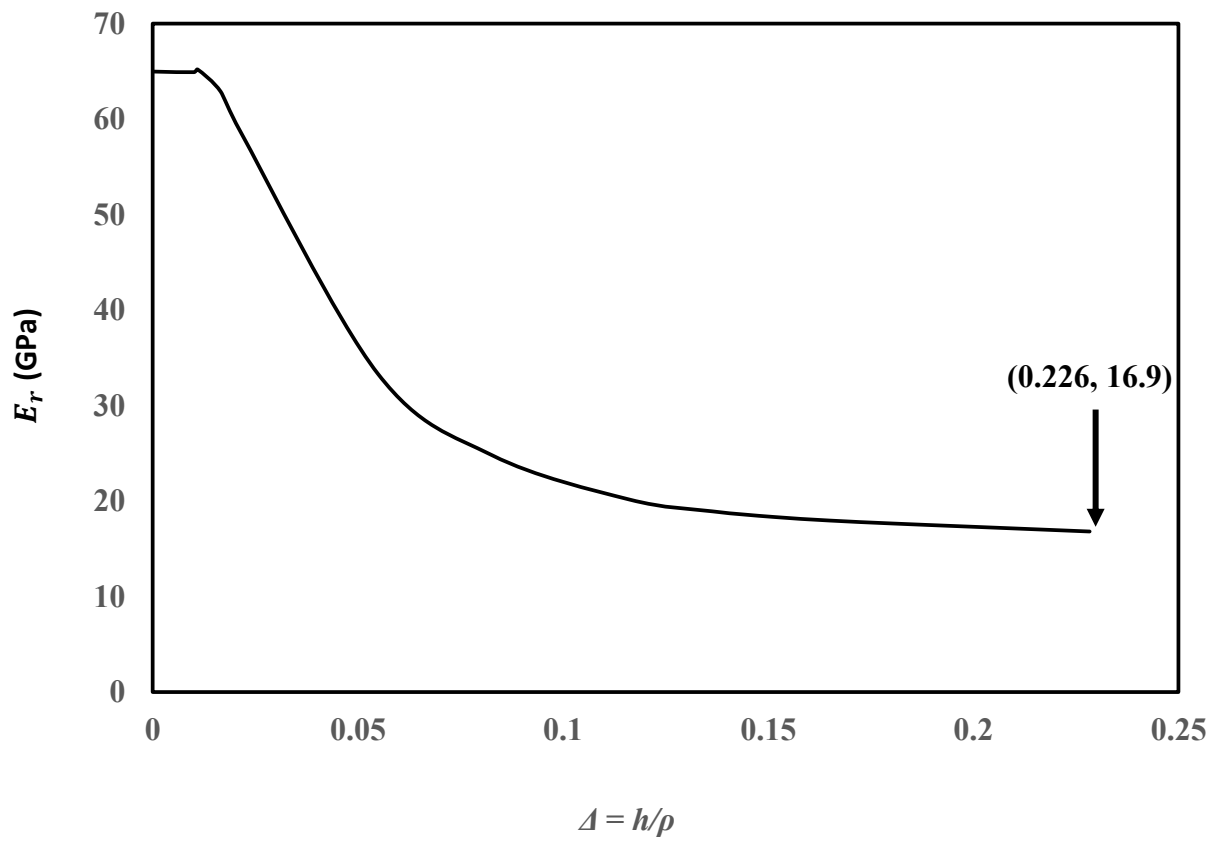
Figure 4.1: Reduced modulus vs. *Δ* curve of superelastic SMA shaft.
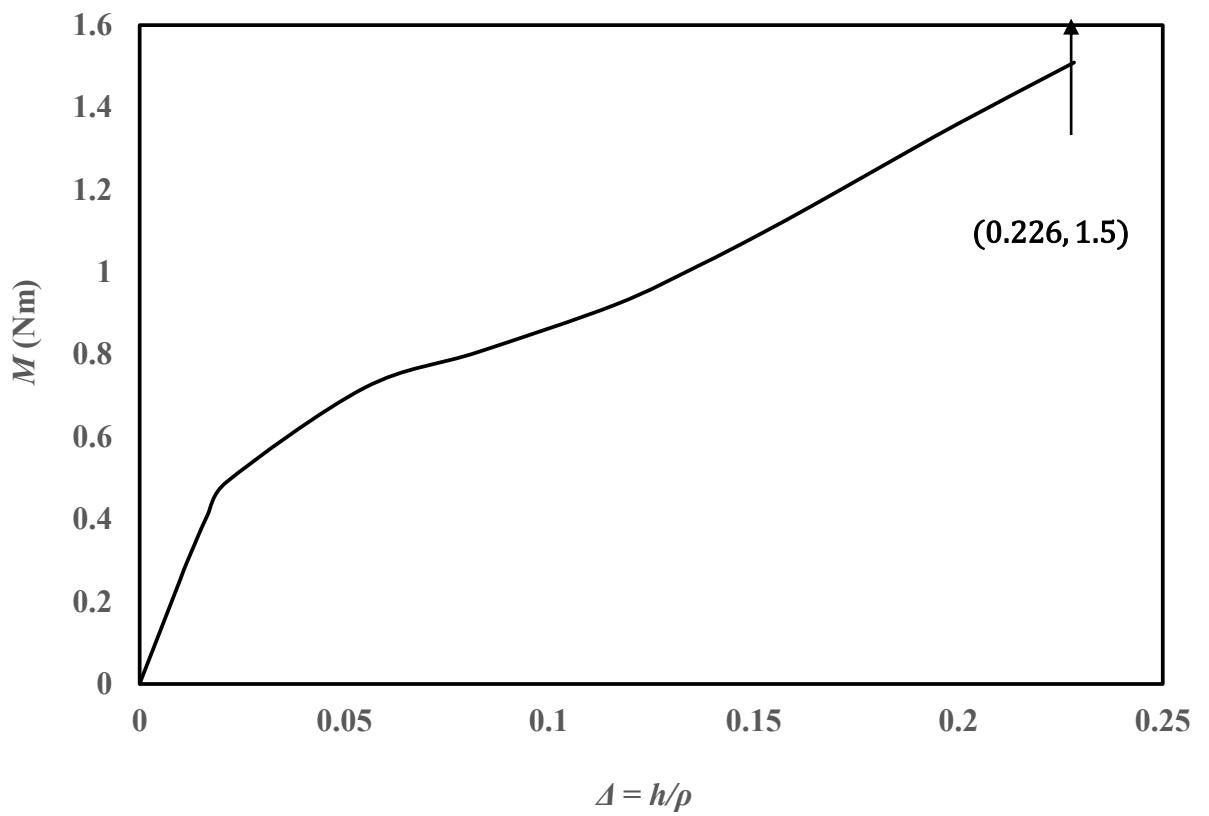
Figure 4.2: Bending moment, M vs. $\varDelta$ curve of superelastic SMA shaft.
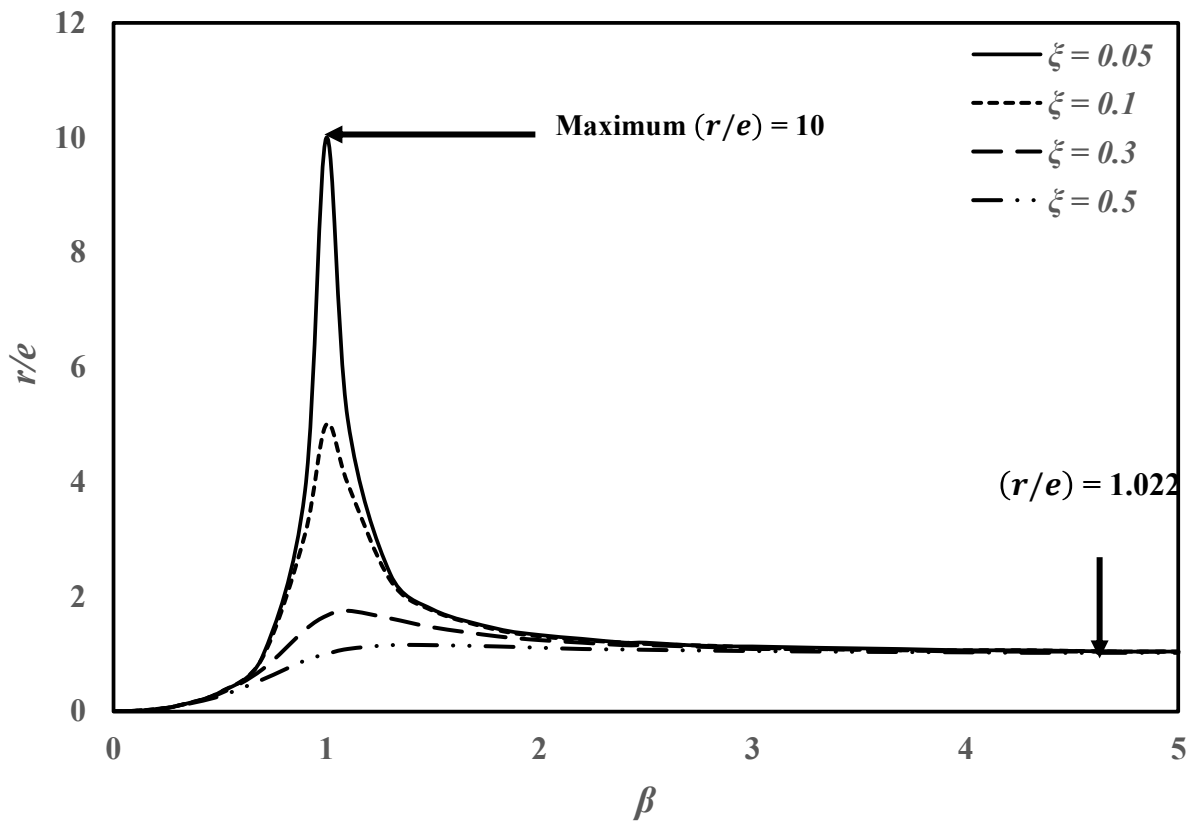
Figure 4.3: Steady-state non-dimensional whirling amplitude (r/e) vs. spin ratio (β) for different damping ratio (ξ) for synchronous whirl condition for superelastic SMA shaft [Shaft specification w.r.t section 4.2].
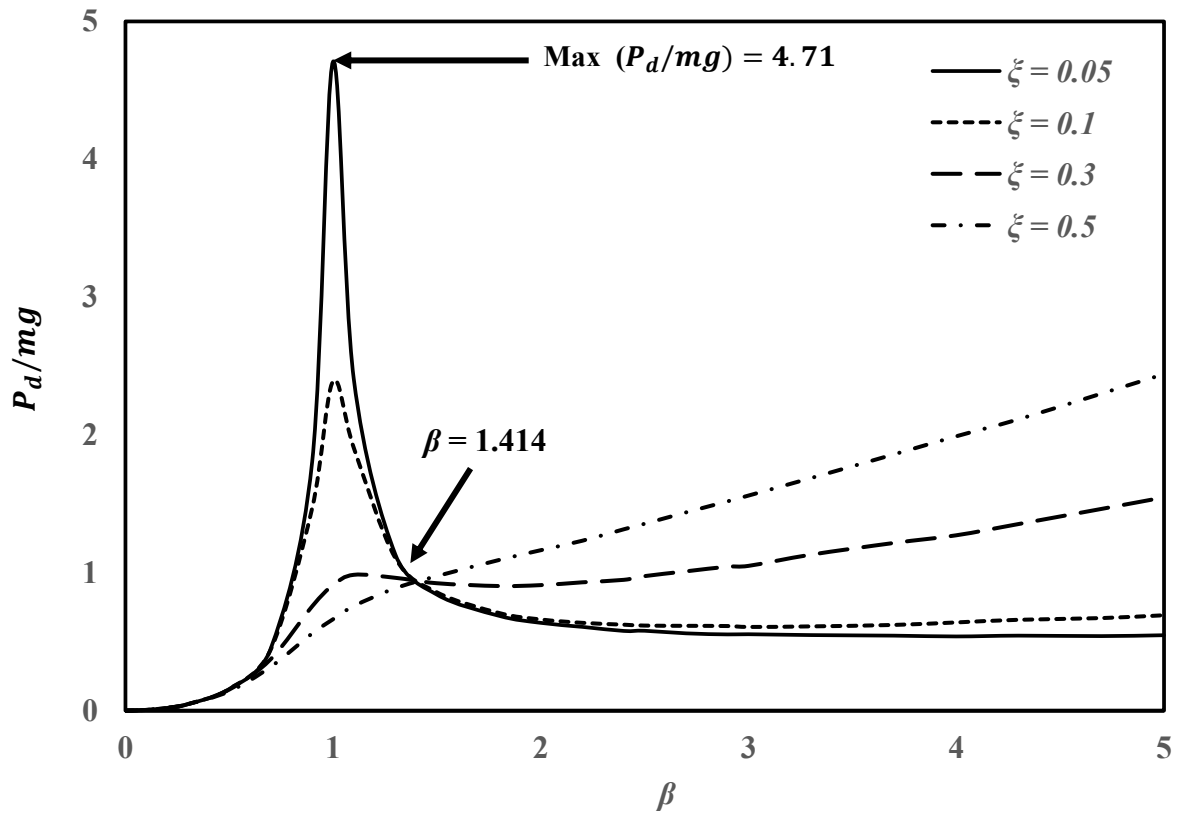
Figure 4.4: Steady-state non-dimensional dynamic force (P_d/mg) at shaft center vs. spin ratio (β) for different damping ratio (ξ) for synchronous whirl condition for superelastic SMA shaft [Shaft specification w.r.t section 4.2].
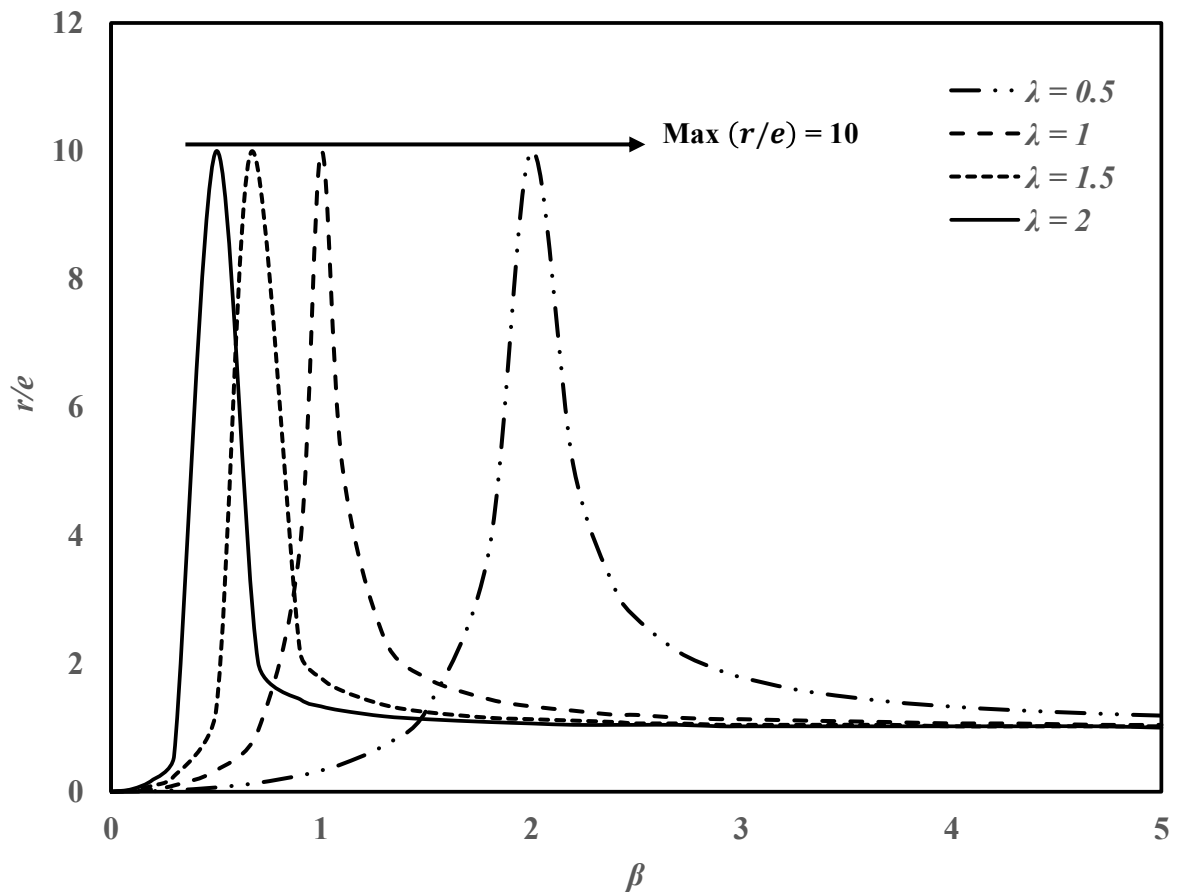
Figure 4.5: Steady-state non-dimensional whirling amplitude (r/e) vs. spin ratio (β) for different asynchronous whirl conditions for superelastic SMA shaft [Shaft specification w.r.t section 4.2, $\xi = 0.05$].
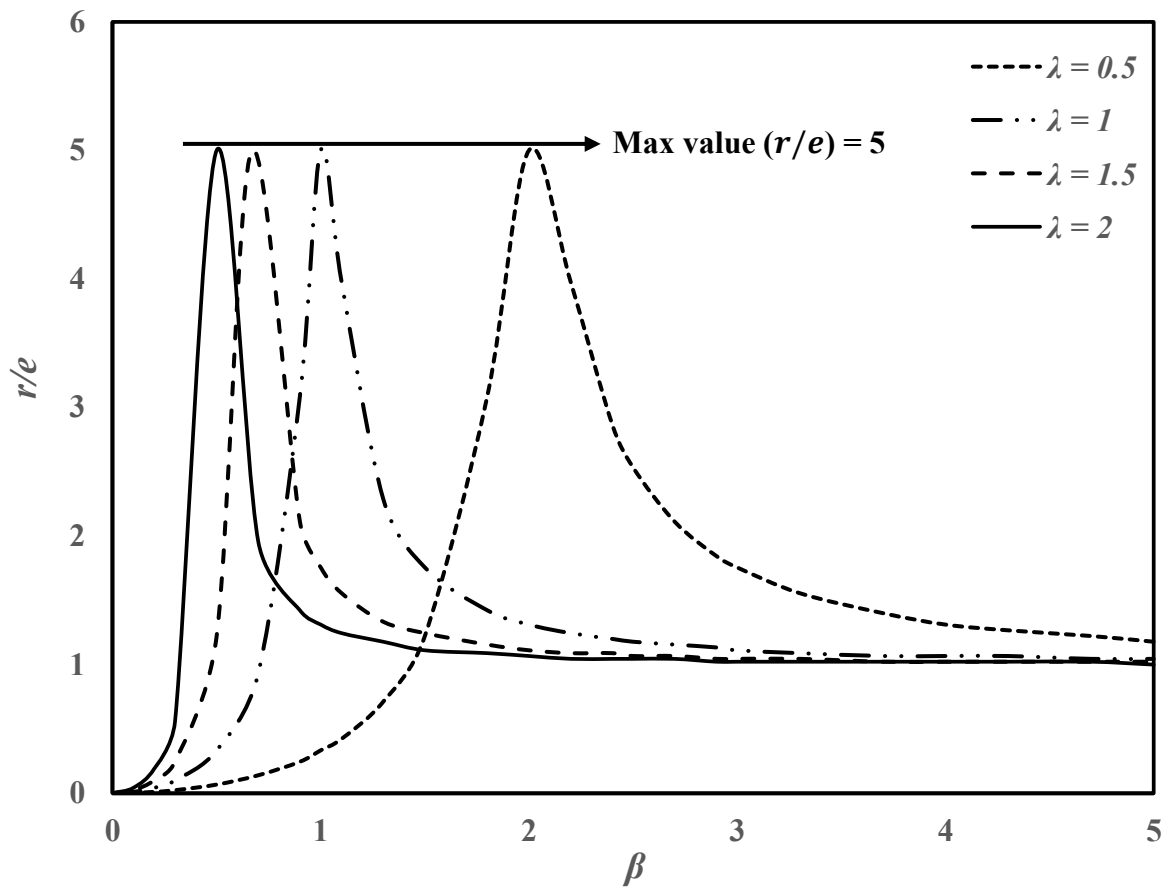
Figure 4.6: Steady-state non-dimensional whirling amplitude (r/e) vs. spin ratio (β) for different asynchronous whirl conditions for superelastic SMA shaft [Shaft specification w.r.t section 4.2, $\xi = 0.1$].
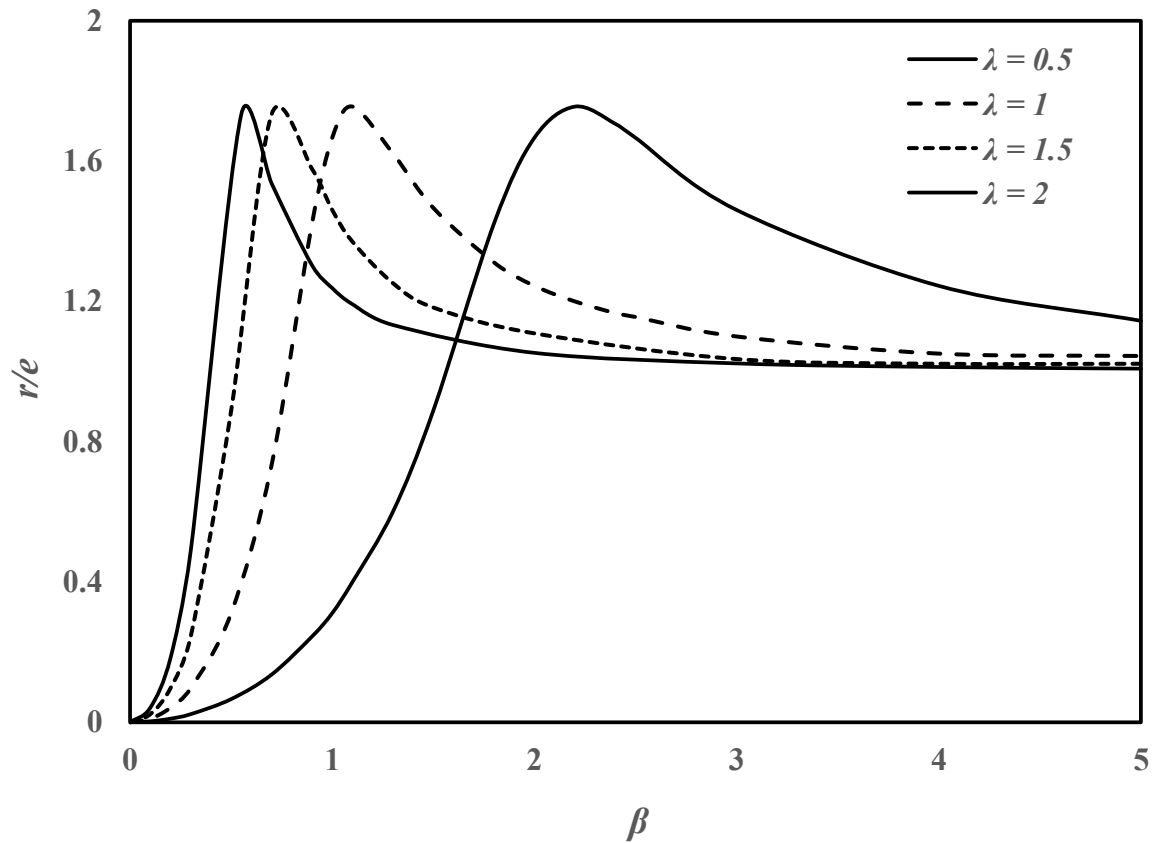
Figure 4.7: Steady-state non-dimensional whirling amplitude (r/e) vs. spin ratio (β) for different asynchronous whirl conditions for superelastic SMA shaft [Shaft specification w.r.t section 4.2, $\xi = 0.3$].
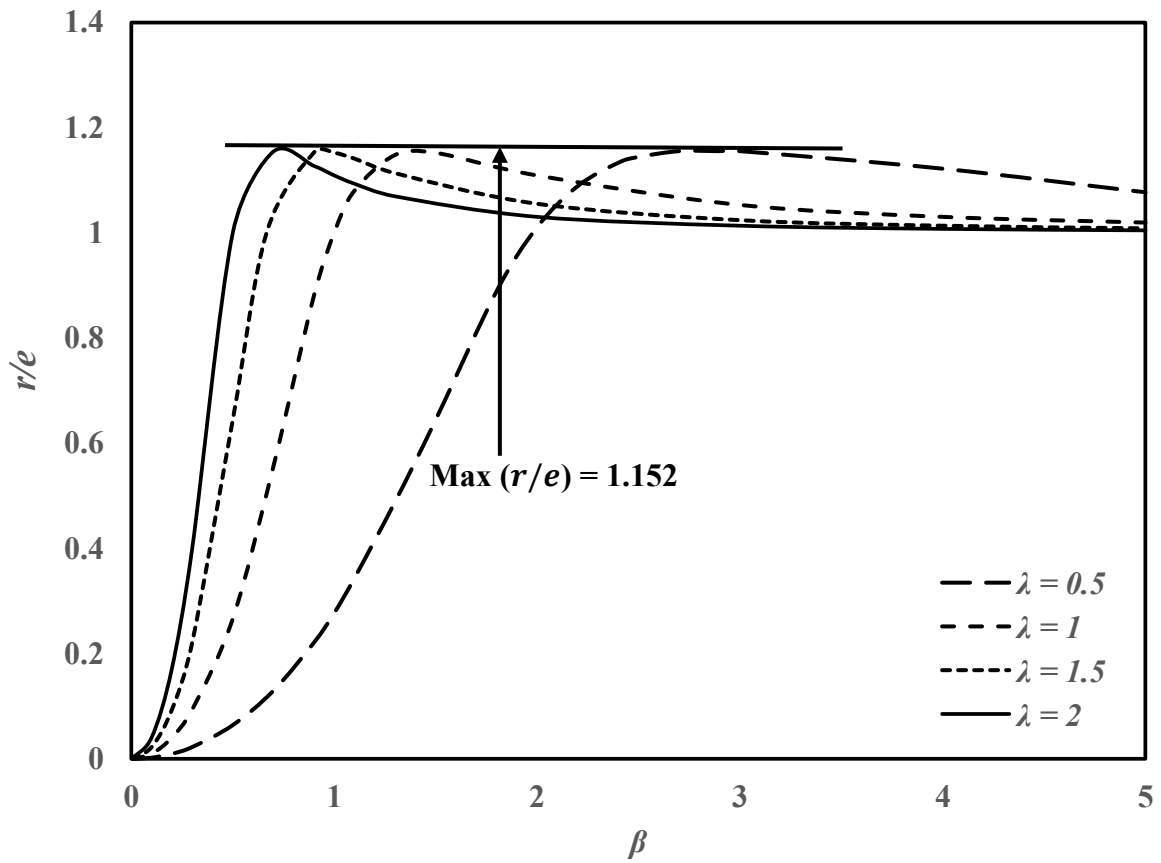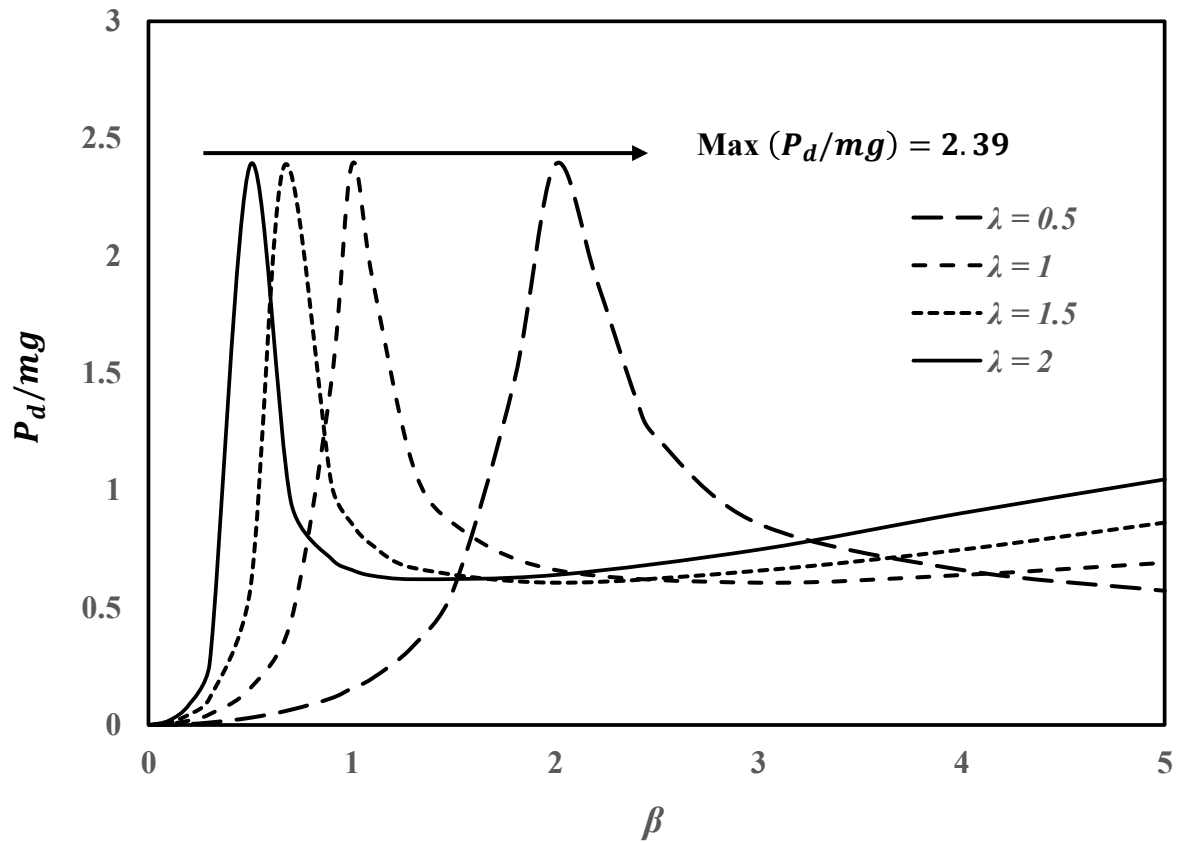
Figure 4.8: Steady-state non-dimensional whirling amplitude (r/e) vs. spin ratio (β) for different asynchronous whirl condition for superelastic SMA shaft [Shaft specification w.r.t section 4.2, ξ=0.5].
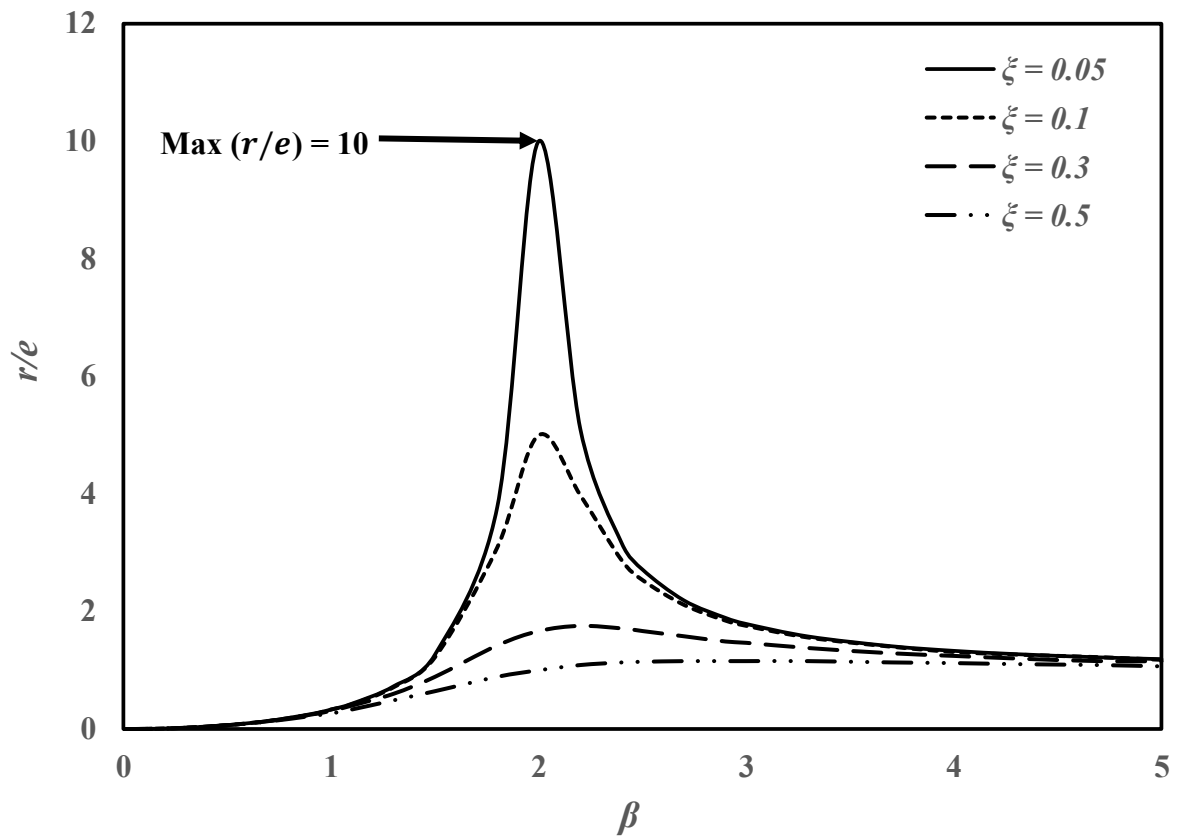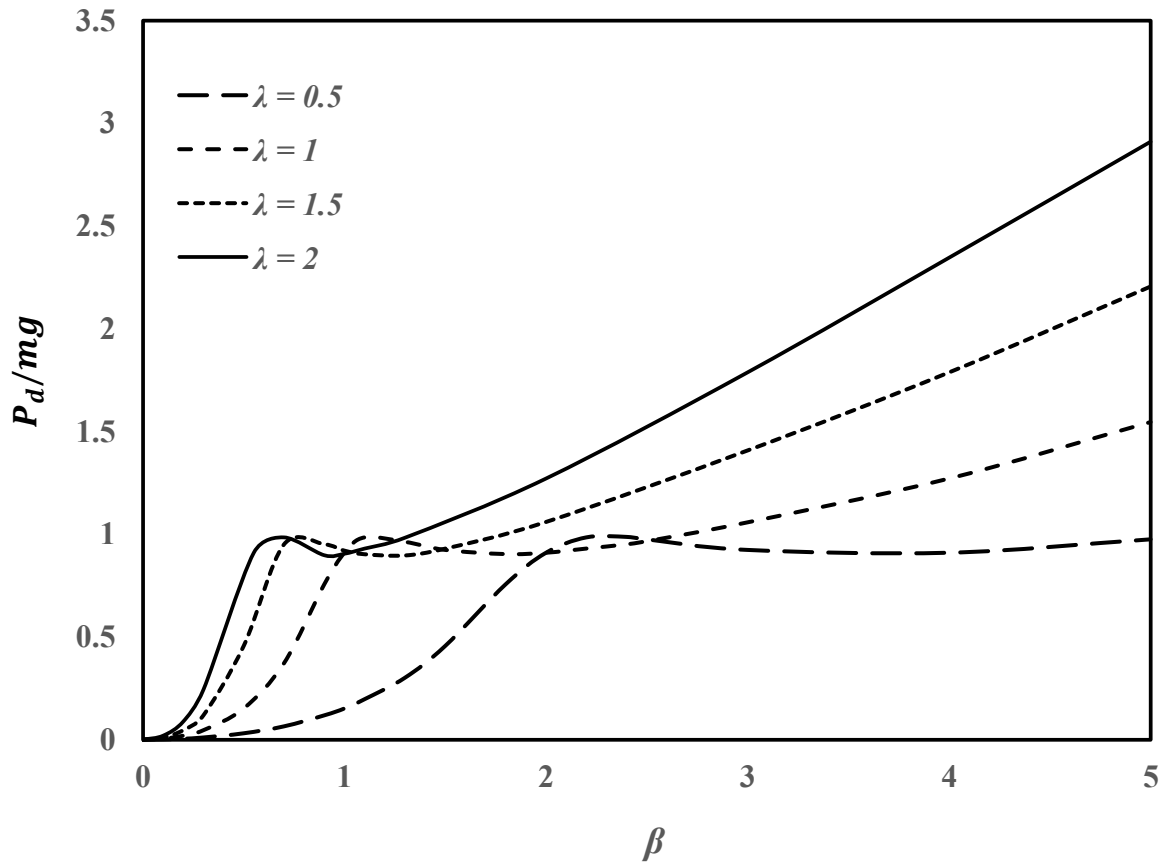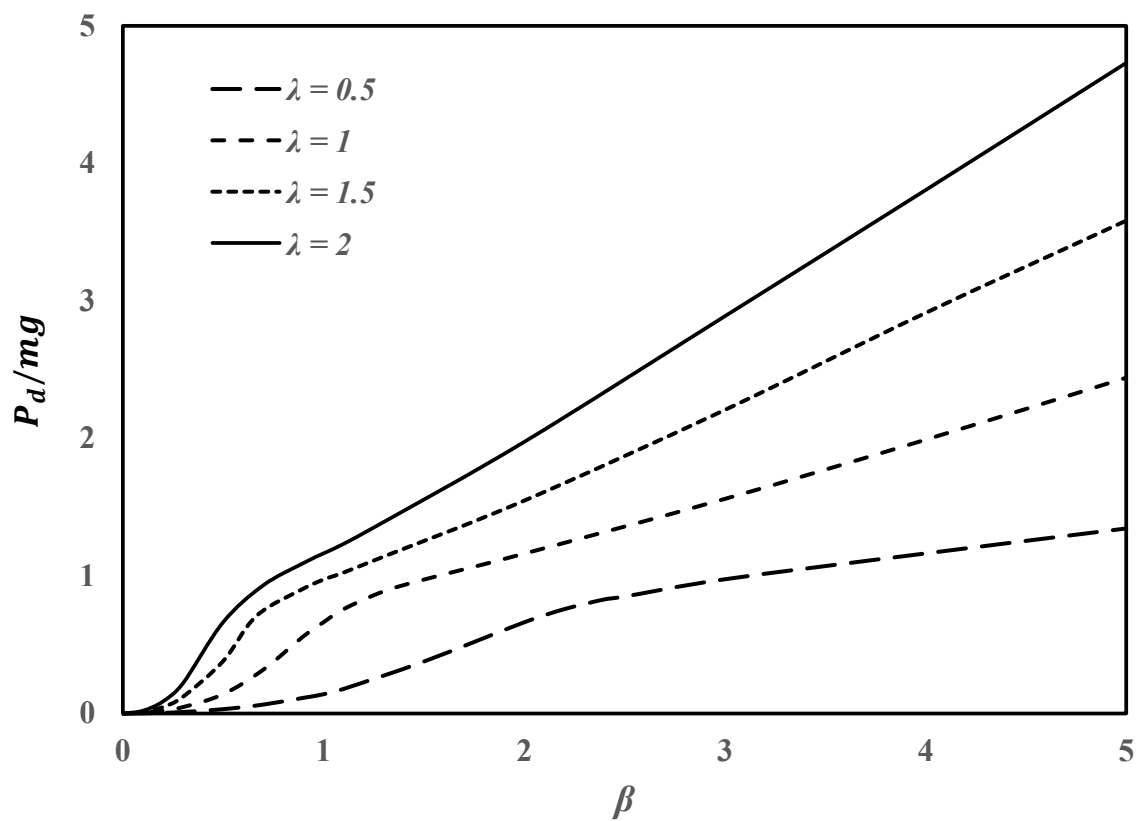
Figure 4.9: Steady-state non-dimensional whirling amplitude (r/e) vs. spin ratio (β) for asynchronous whirl condition ($\lambda = 0.5$) for different damping ratio (ξ) for superelastic SMA shaft [Shaft specification w.r.t section 4.2].
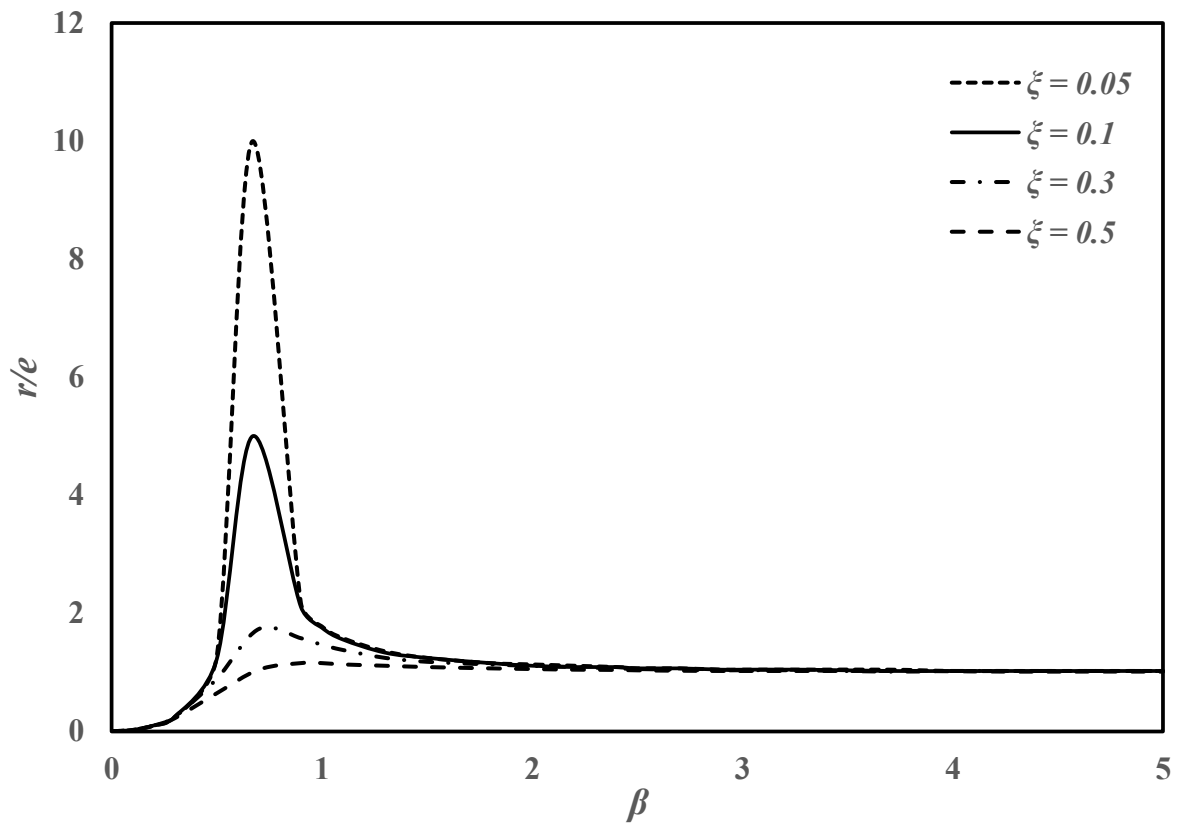
Figure 4.10: Steady-state non-dimensional whirling amplitude (r/e) vs. spin ratio (β) for asynchronous whirl condition ($\lambda = 1.5$) for different damping ratio (ξ) for superelastic SMA shaft [Shaft specification w.r.t section 4.2].
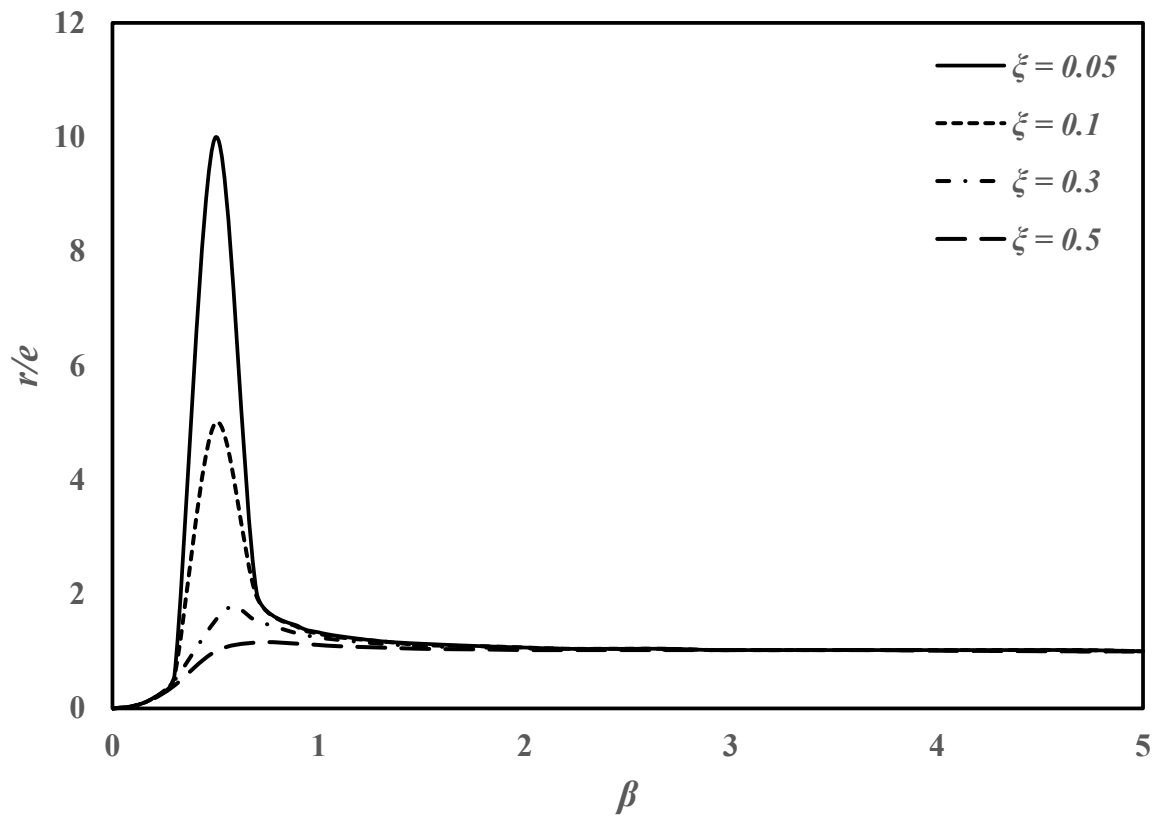
Figure 4.11: Steady-state non-dimensional whirling amplitude (r/e) vs. spin
Ratio (β) for asynchronous whirl condition ($\lambda = 2$) for different
Damping ratio (ξ) for superelastic SMA shaft [Shaft specification
w.r.t. section 4.2].
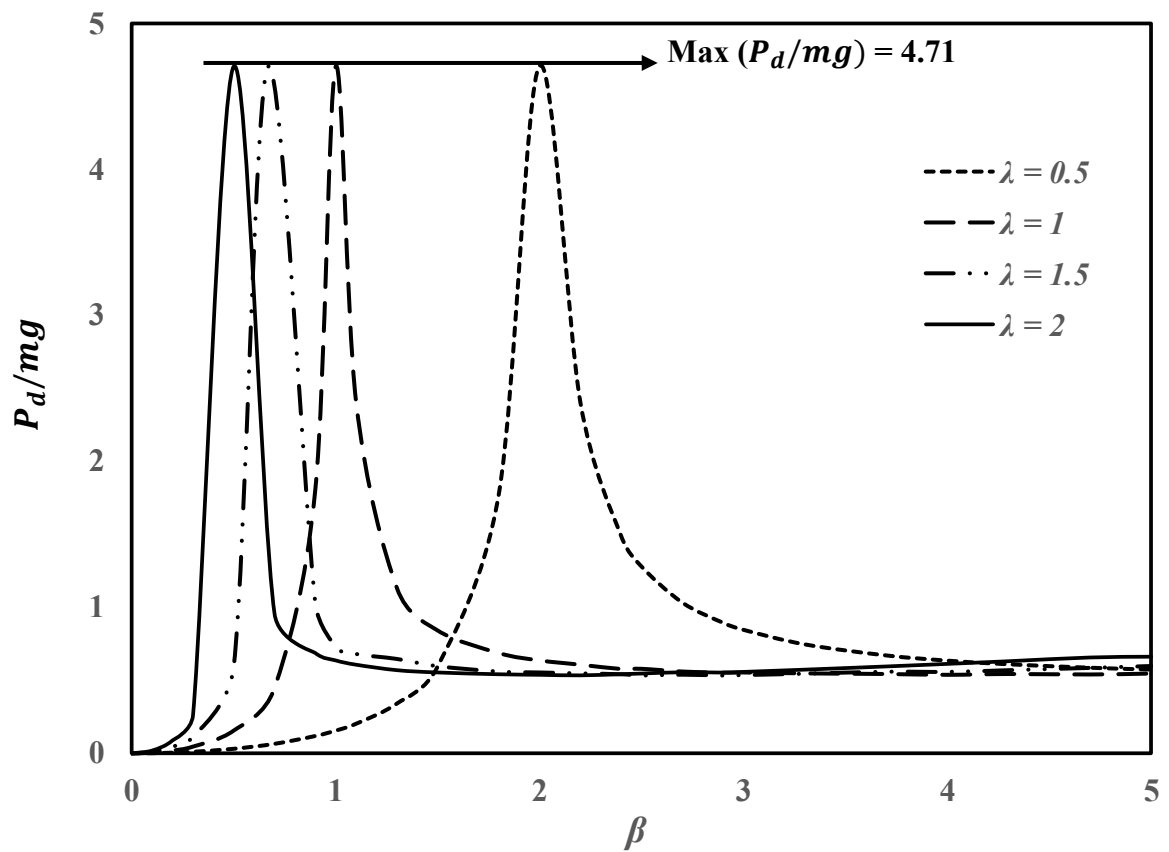
Figure 4.12: Steady-state non-dimensional dynamic force (P_d/mg) vs. spin ratio (β) for different asynchronous whirl conditions for superelastic SMA shaft [Shaft specification w.r.t section 4.2, $\xi = 0.05$].
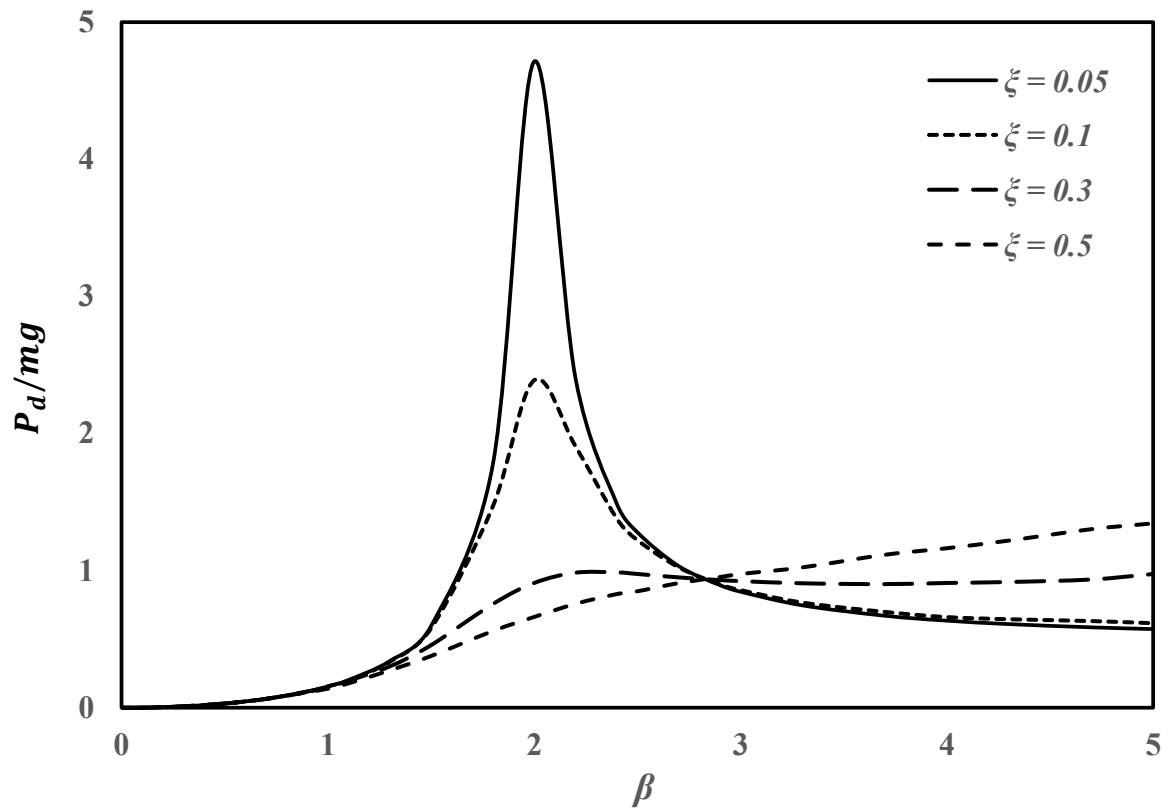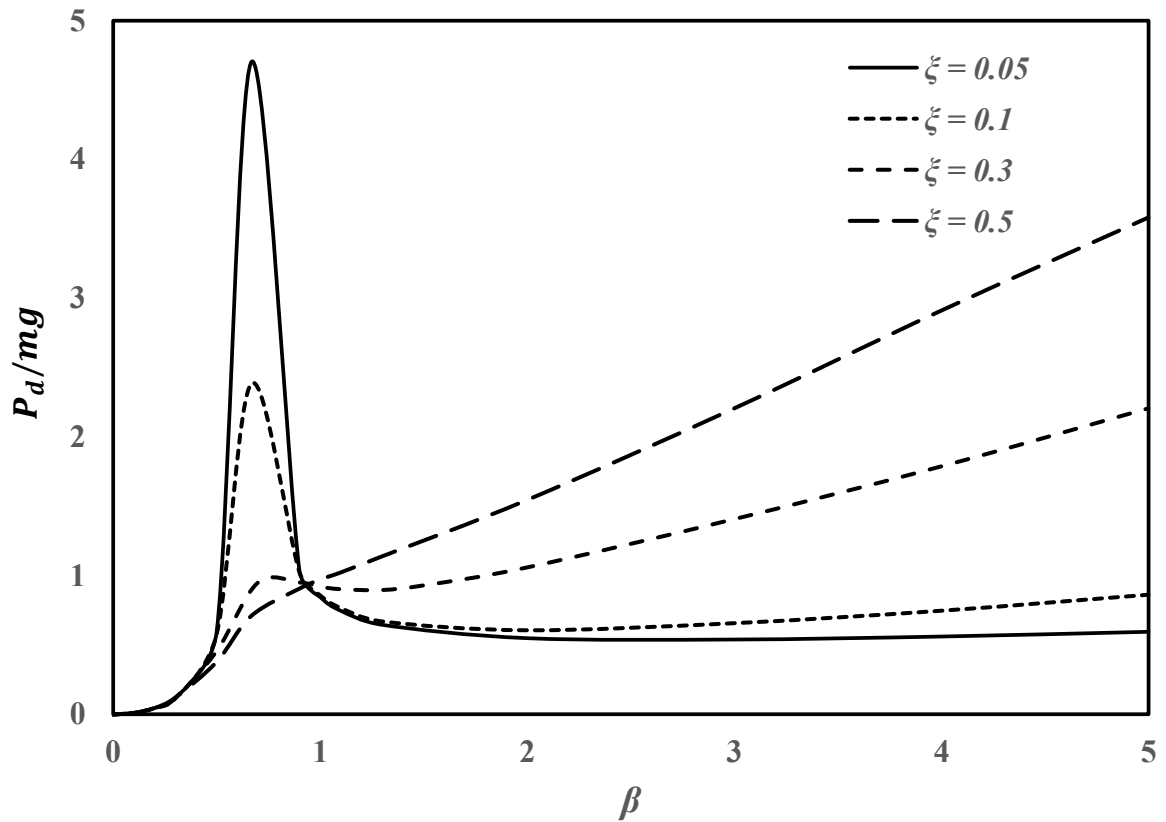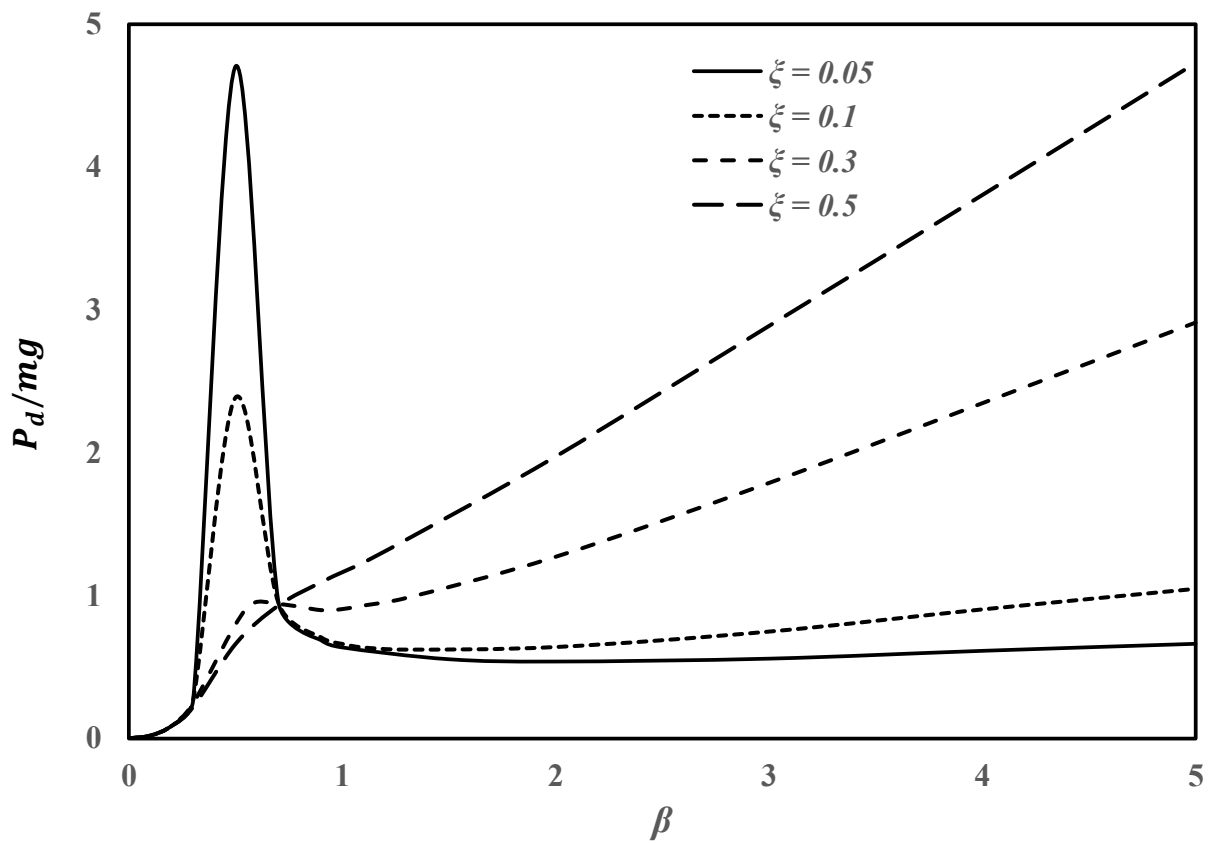
Figure 4.13: Steady-state non-dimensional dynamic force (P_d/mg) vs. spin ratio (β) for different asynchronous whirl conditions for superelastic SMA shaft [Shaft specification w.r.t section 4.2, $\xi = 0.1$].

Figure 4.14: Steady-state non-dimensional dynamic force (P_d/mg) vs. spin
ratio (β) for different asynchronous whirl conditions for
superelastic SMA shaft [Shaft specification w.r.t section 4.2, $\xi =$
0.3].

Figure 4.15: Steady-state non-dimensional dynamic force (P_d/mg) vs. spin ratio (β) for different asynchronous whirl conditions for superelastic SMA shaft [Shaft specification w.r.t section 4.2, $\xi = 0.5$].

Figure 4.16: Steady-state non-dimensional dynamic force (P_d/mg) vs. spin
ratio (β) for asynchronous whirl condition ($\lambda = 0.5$) for different
damping ratio (ξ) for superelastic SMA shaft [Shaft specification
w.r.t section 4.2].

Figure 4.17: Steady-state non-dimensional dynamic force (P_d/mg) vs. spin ratio (β) for asynchronous whirl condition ($\lambda = 1.5$) for different damping ratio (ξ) for superelastic SMA shaft [Shaft specification w.r.t section 4.2].

Figure 4.18: Steady-state non-dimensional dynamic force (P_d/mg) vs. spin ratio (β) for asynchronous whirl condition ($\lambda = 2$) for different damping ratio (ξ) for superelastic SMA shaft [Shaft specification w.r.t section 4.2].
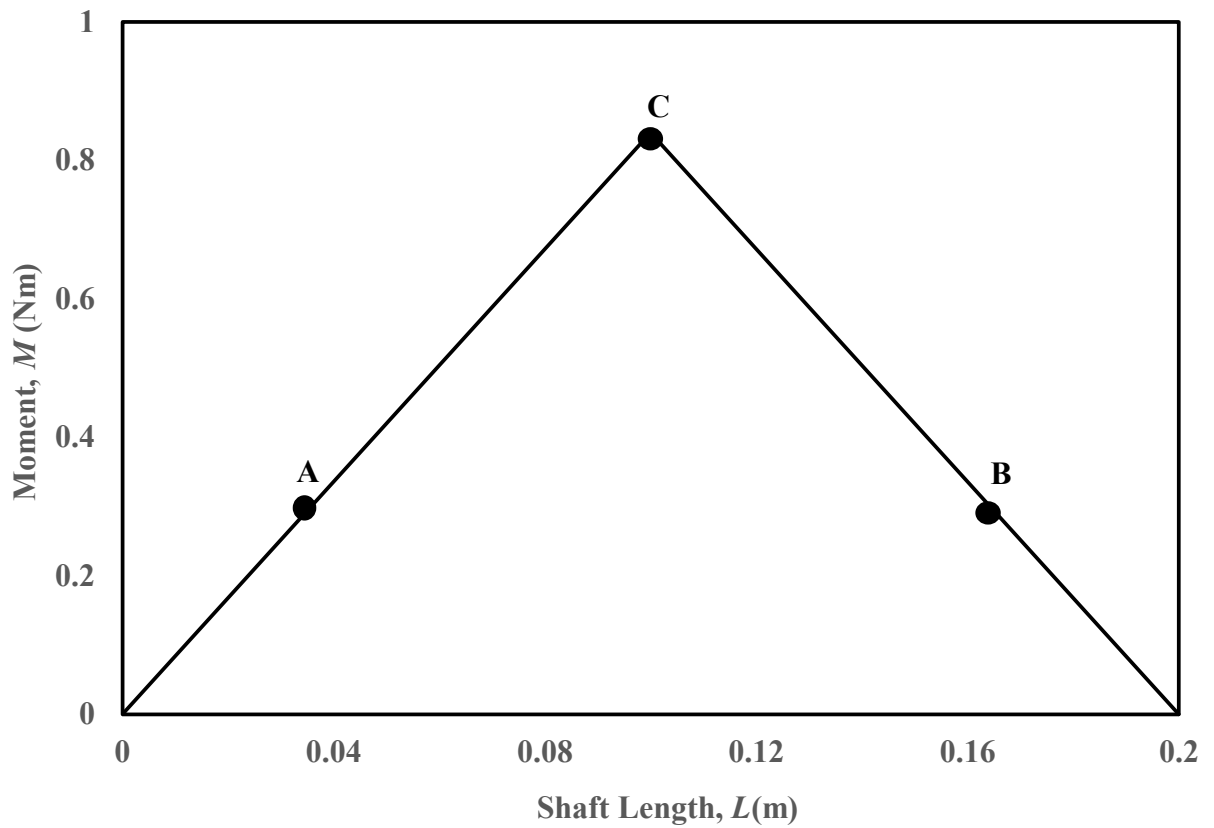
Figure 4.19: Bending moment (M) vs. shaft length (L) for superelastic SMA shaft w.r.t. Figure 4.5 & 4.12. $[\left(\frac{r}{e}\right) = 10, \left(\frac{P_d}{mg}\right) = 4.71, P = P_d + mg = 16.8\ N.]$ Threshold moment at point A & B = 0.3041 Nm. Compressive & tensile stress at A & B = 362.81 & 389.424 MPa respectively. Maximum bending moment at mid-span (Point C) of shaft = 0.84 Nm. Compressive & tensile stress at C = 917.474 and 606.542 MPa respectively.
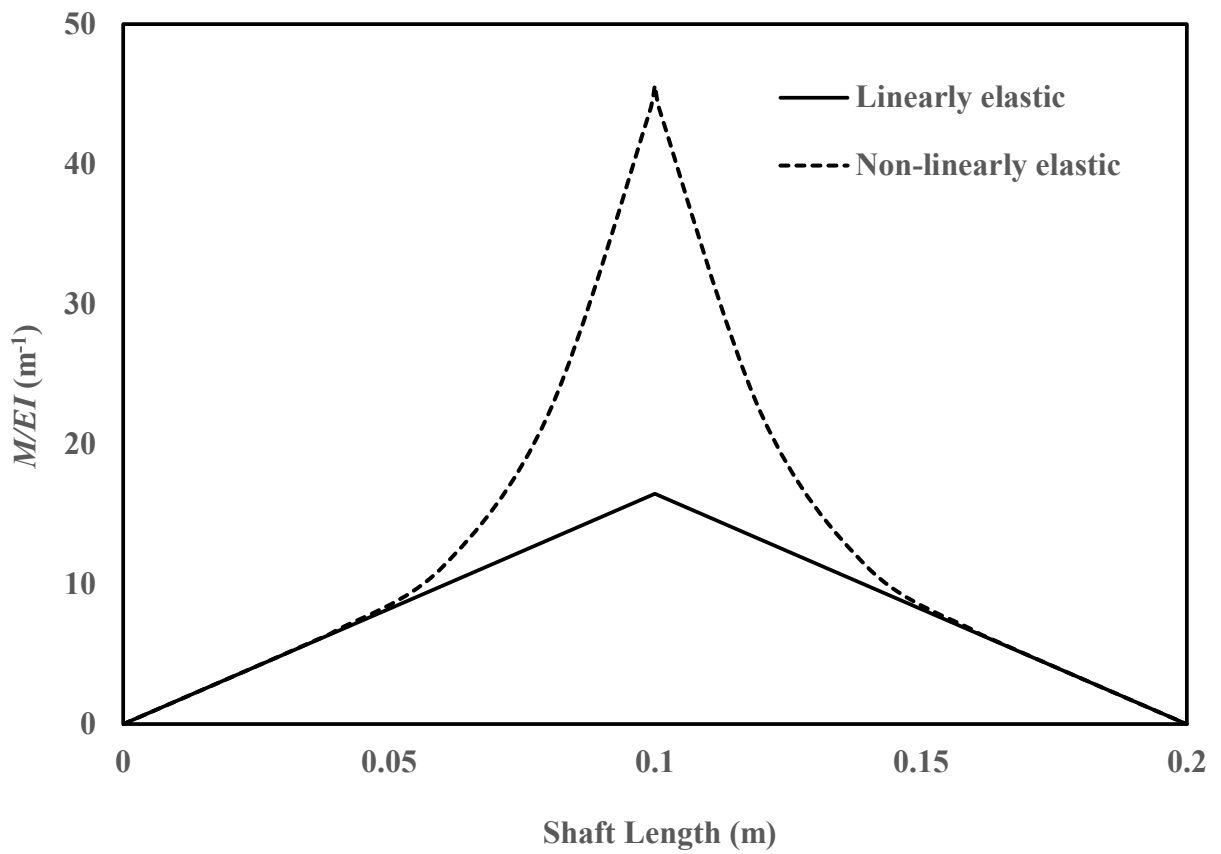
Figure 4.20: Bending moment (*M/EI*) vs. shaft length (*L*) of superelastic SMA shaft w.r.t. Figures 4.1 & 4.19.
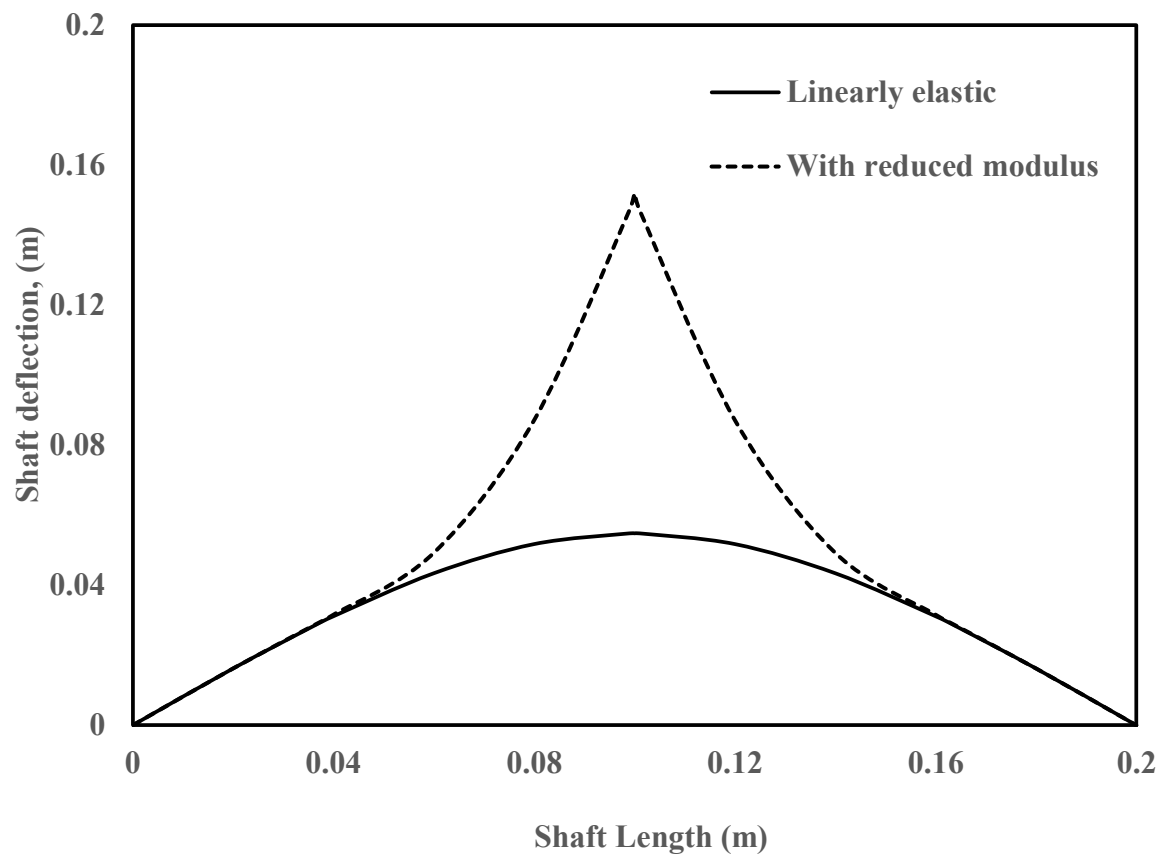
Figure 4.21: Shaft deflection vs. shaft length considering both linear and

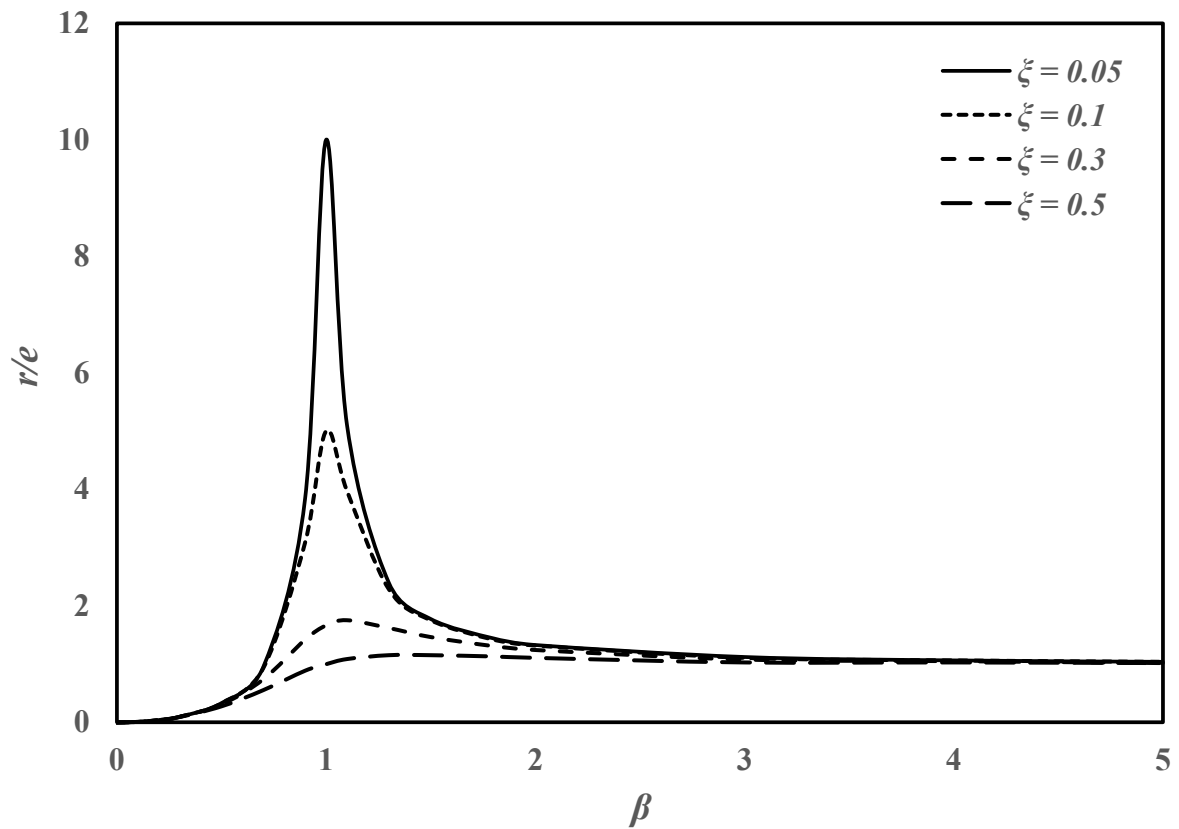non - linear model for SMA shaft w.r.t Figure 4.20.

Figure 4.22: Steady-state non-dimensional whirling amplitude (r/e) vs. spin ratio (β) for different damping ratio (ξ) for synchronous whirl condition for Stainless steel shaft [Shaft specification w.r.t section 4.5].
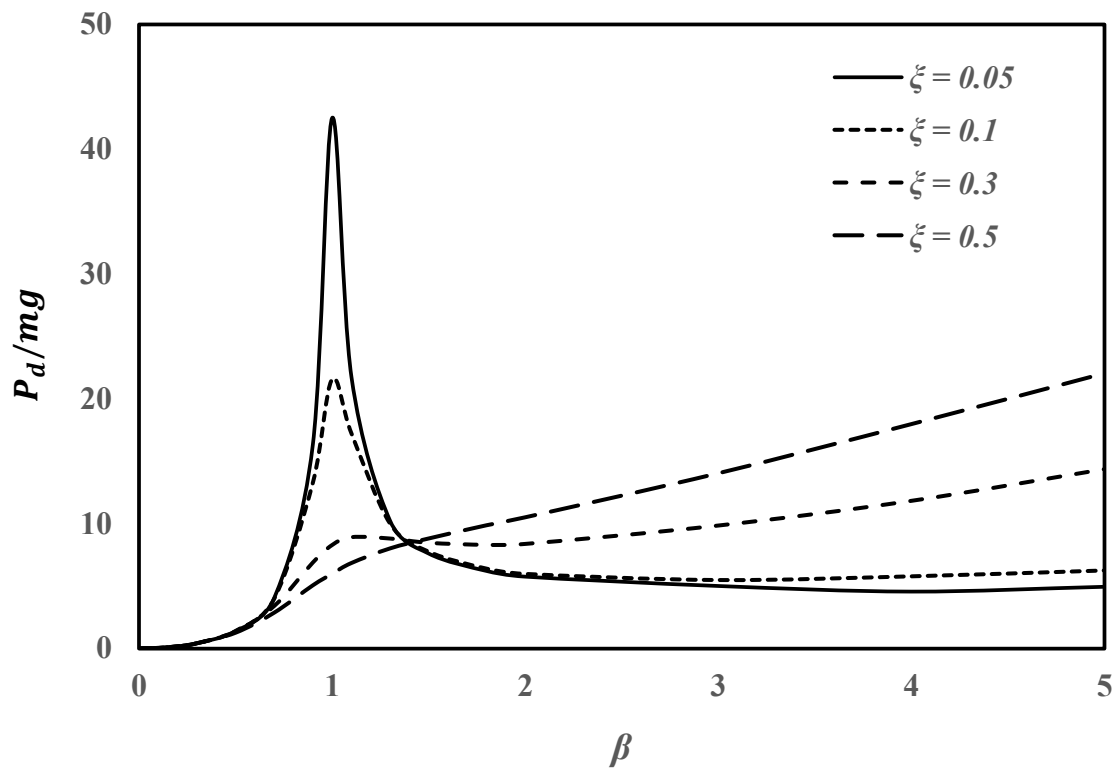
Figure 4.23: Steady-state non-dimensional dynamic force (P_d/mg) at shaft center vs. spin ratio (β) for different damping ratio (ξ) for synchronous whirl condition for Stainless steel shaft [Shaft specification w.r.t section 4.5].
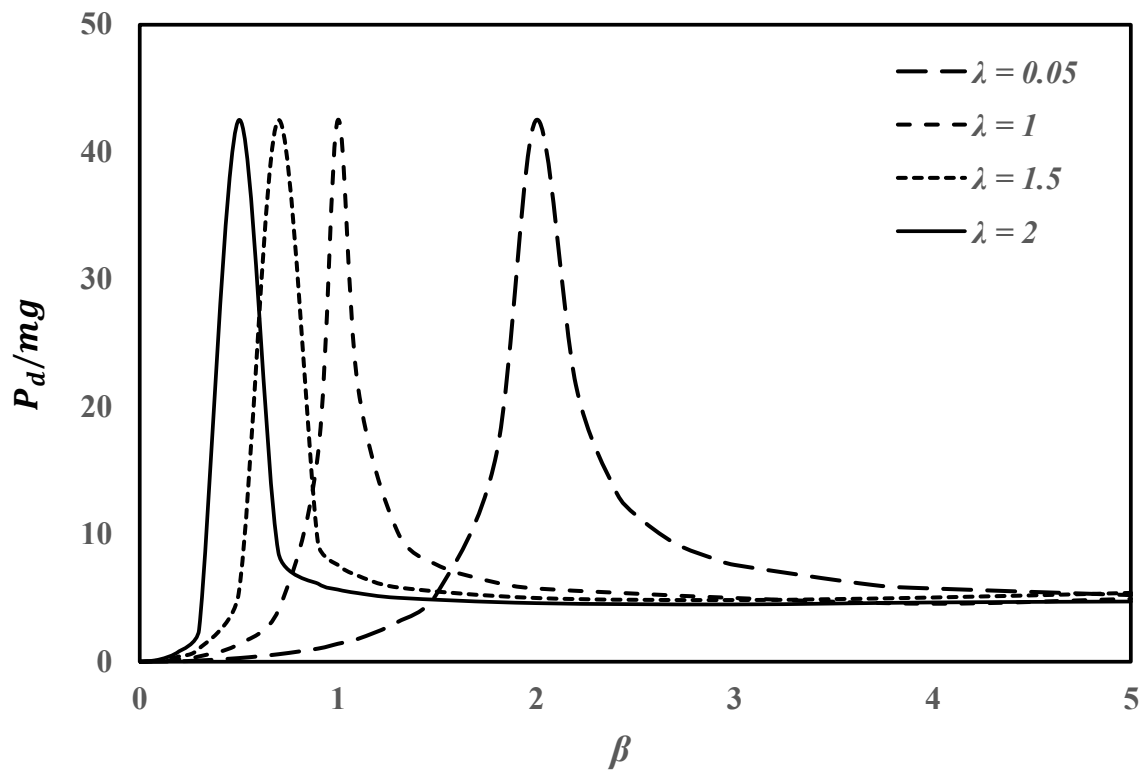
Figure 4.24: Steady-state non-dimensional dynamic force (P_d/mg) vs. spin ratio (β) for different asynchronous whirl conditions for Stainless steel shaft [Shaft specification w.r.t section 4.5, $\xi = 0.05$].
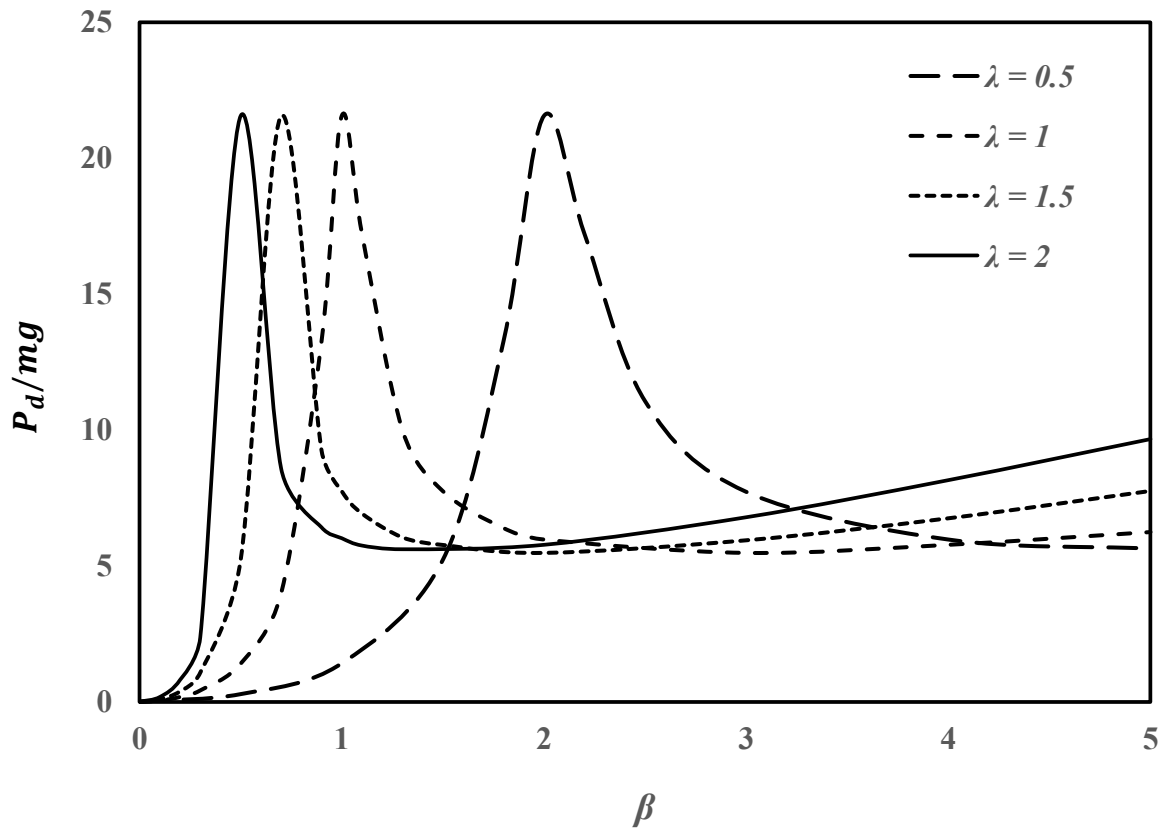
Figure 4.25: Steady-state non-dimensional dynamic force (P_d/mg) vs. spin ratio (β) for different asynchronous whirl conditions for Stainless steel shaft [Shaft specification w.r.t section 4.5, $\xi = 0.1$].
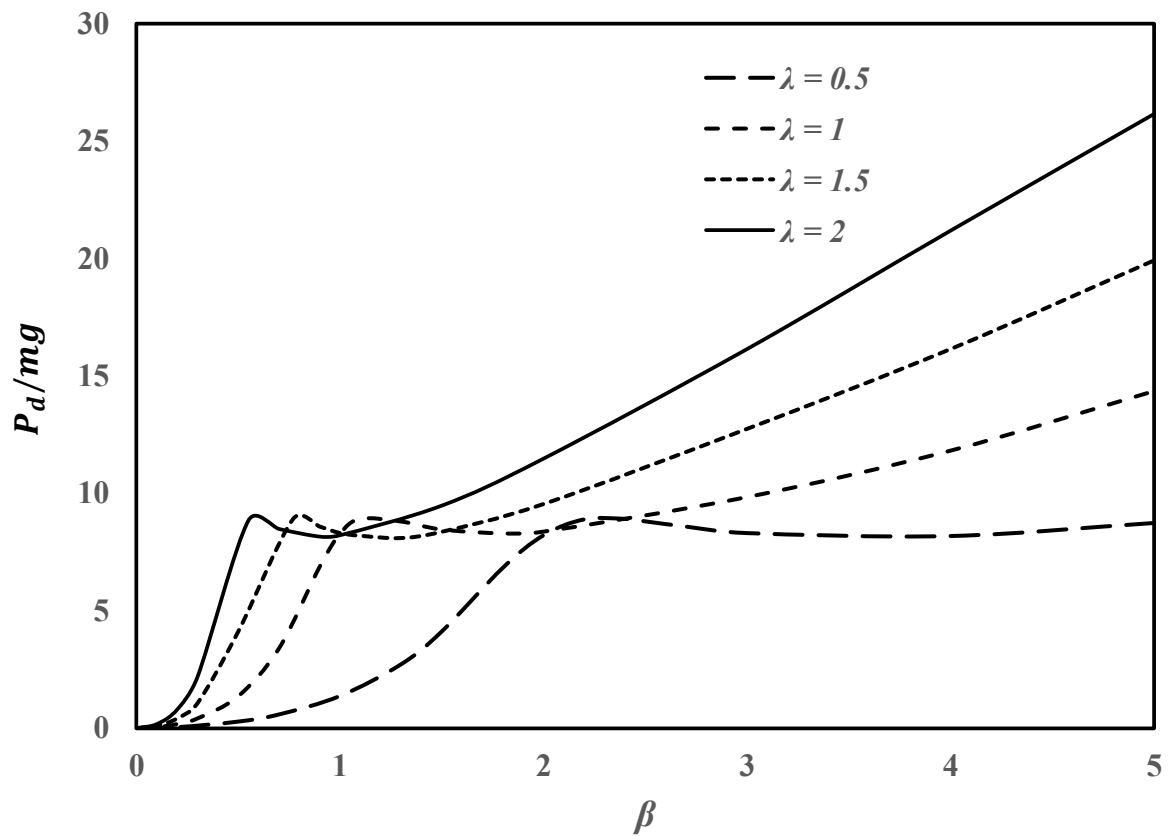
Figure 4.26: Steady-state non-dimensional dynamic force (P_d/mg) vs. spin ratio (β) for different asynchronous whirl conditions for Stainless steel shaft [Shaft specification w.r.t section 4.5, $\xi = 0.3$].
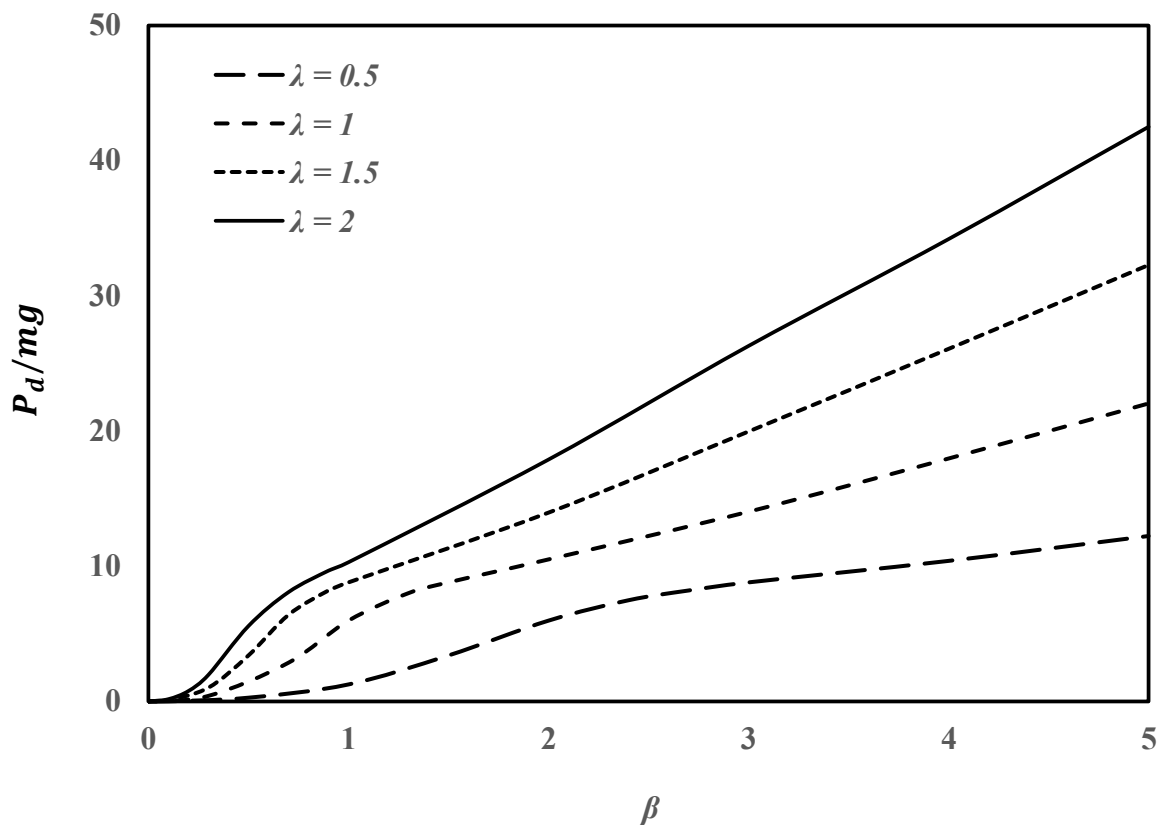
Figure 4.27: Steady-state non-dimensional dynamic force (P_d/mg) vs. spin Ratio (β) for different asynchronous whirl conditions for Stainless steel shaft [Shaft specification w.r.t section 4.5, $\xi = 0.5$].
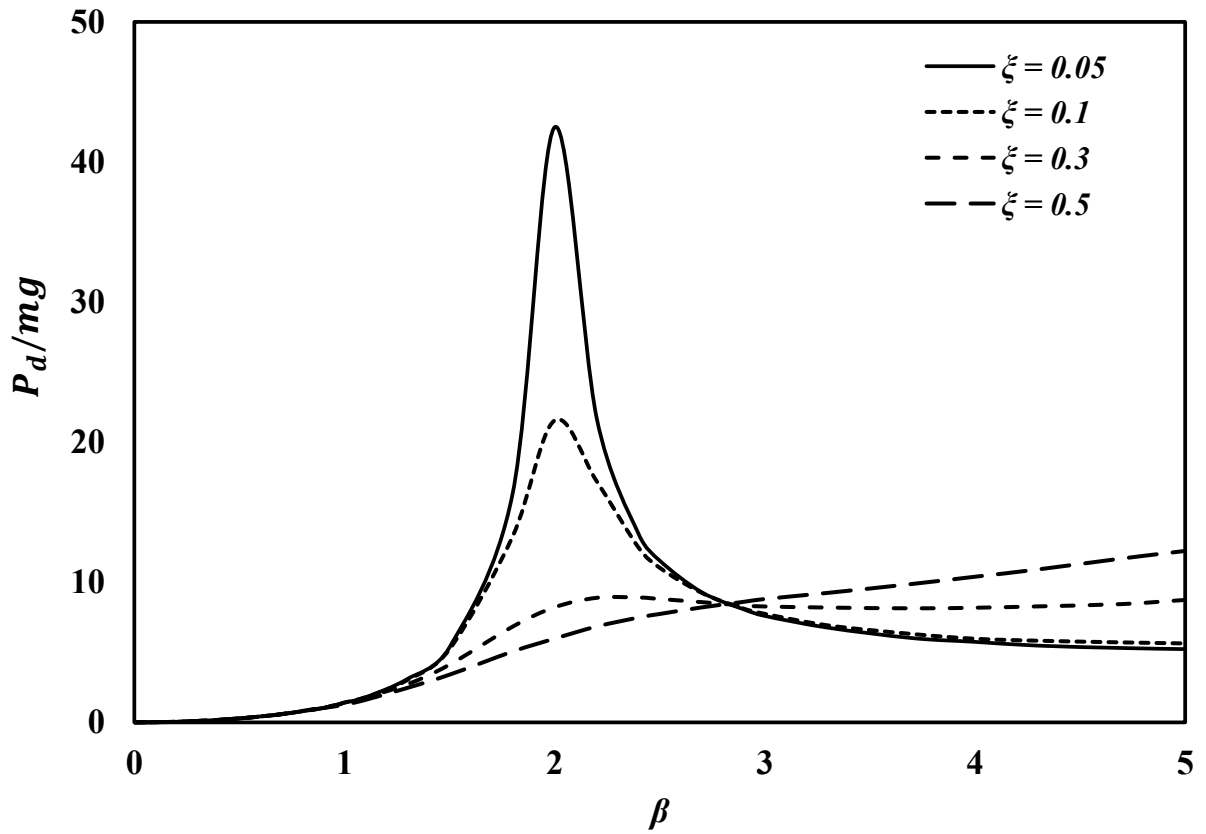
Figure 4.28: Steady-state non-dimensional dynamic force (P_d/mg) vs. spin ratio (β) for asynchronous whirl condition ($\lambda = 0.5$) for different damping Ratio (ξ) for Stainless steel shaft [Shaft specification w.r.t section 4.5].

Figure 4.29: Steady-state non-dimensional dynamic force (P_d/mg) vs. spin ratio (β) for asynchronous whirl condition ($\lambda = 1.5$) for different damping ratio (ξ) for Stainless steel shaft [Shaft specification w.r.t section 4.5].
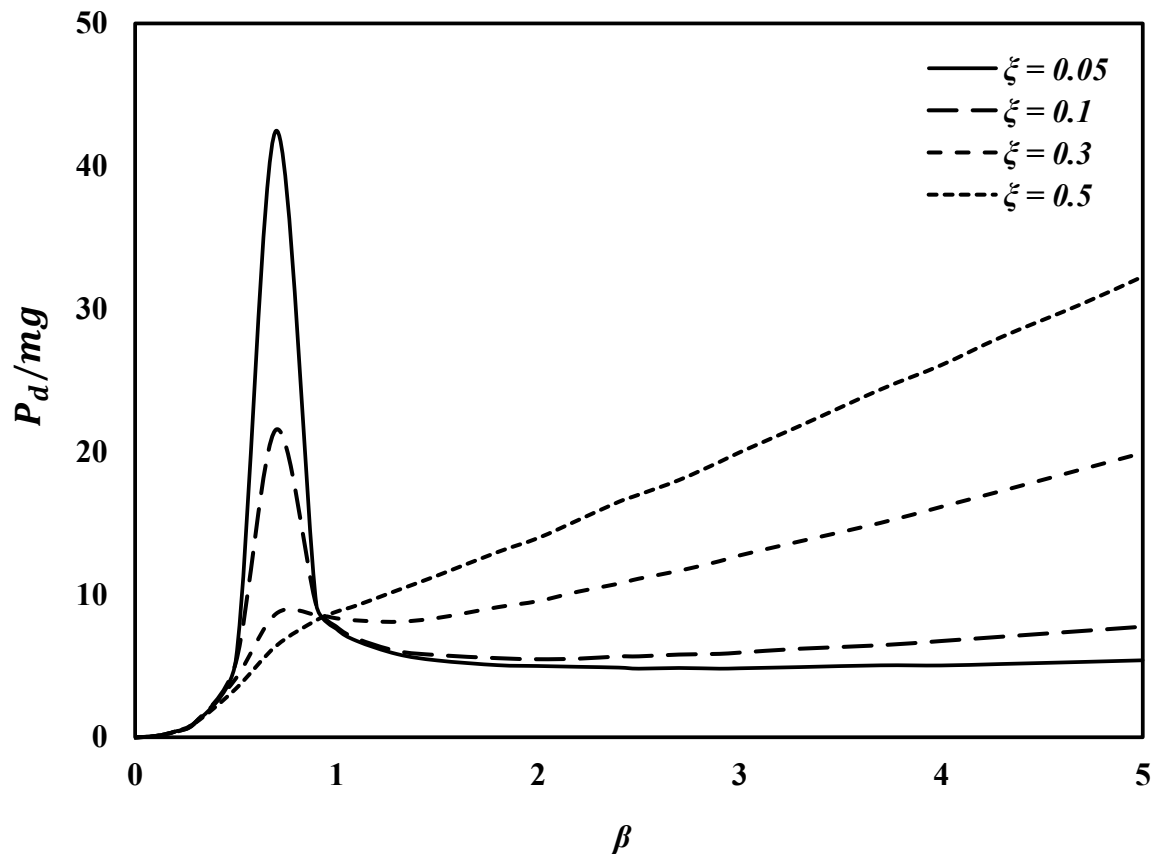
Figure 4.30: Steady-state non-dimensional dynamic force (P_d/mg) vs. spin ratio (β) of asynchronous whirl condition ($\lambda = 2$) for different damping ratio (ξ) for Stainless steel shaft [Shaft specification w.r.t section 4.5].
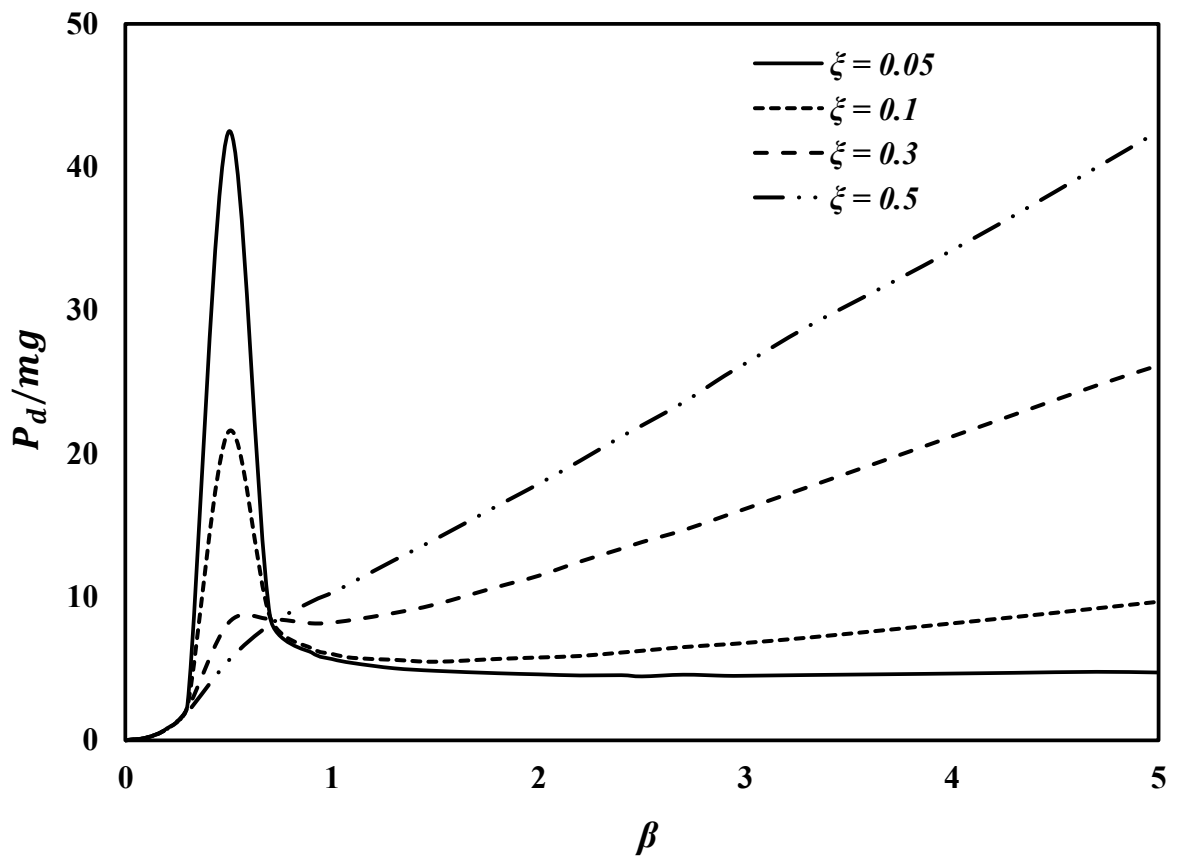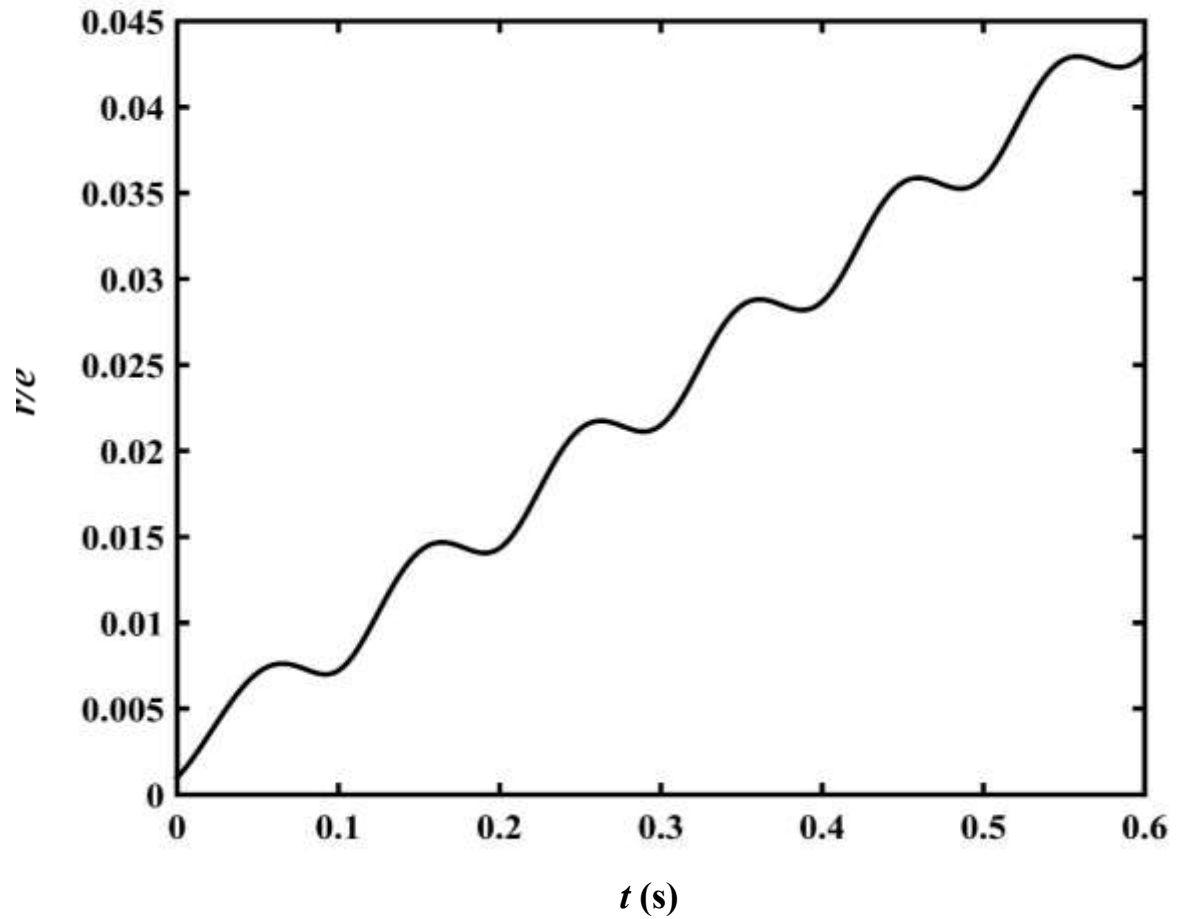
Figure 4.31: Ever increasing, linear whirling amplitude (r) vs. time curve for superelastic SMA shaft [Shaft specification w.r.t section 4.2, $m = 300$ g, $\xi = 0$, $\beta = 1$].
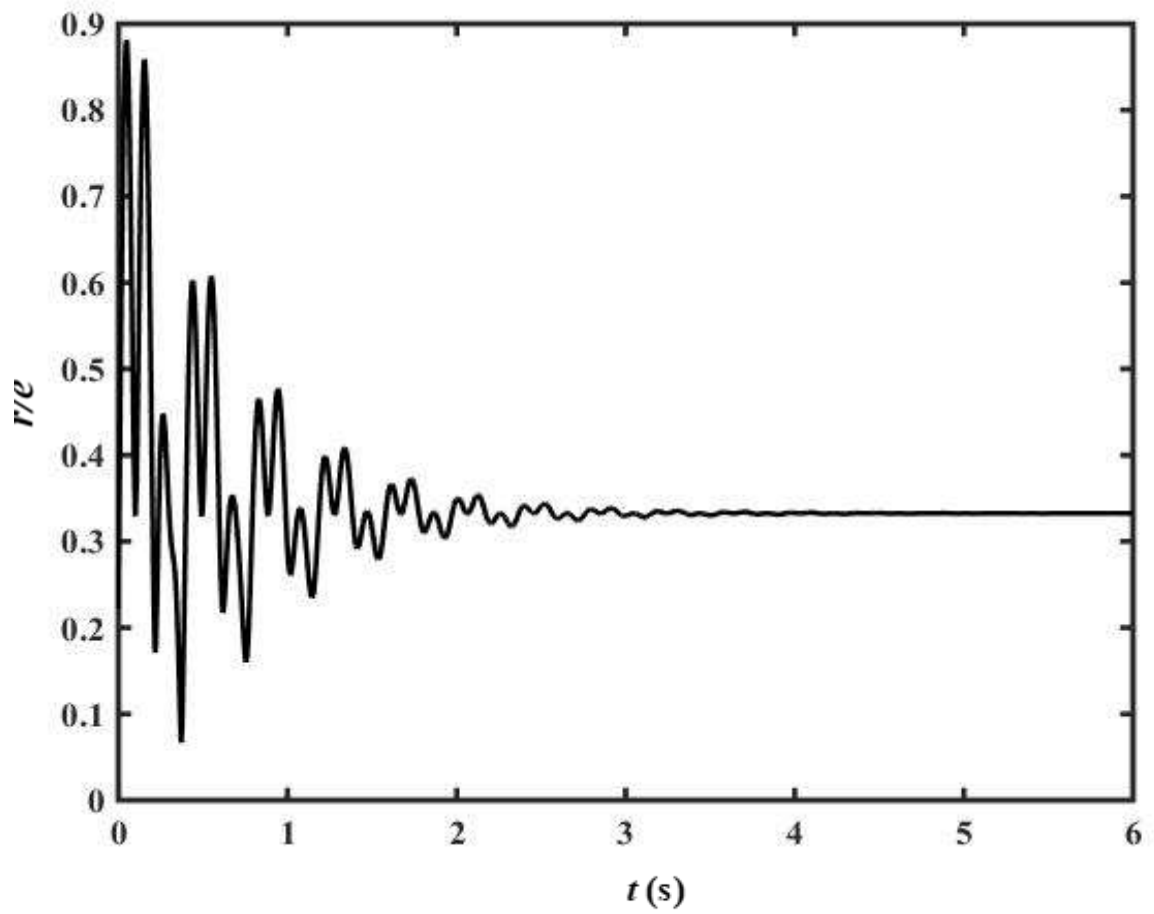
Figure 4.32: Unsteady-state whirl analysis: Non-dimensional whirling amplitude (r/e) vs. time curve for superelastic SMA shaft [Shaft specification w.r.t section 4.2, m = 300 g, ξ = 0.05, β = 0.5].

Figure 4.33: Unsteady-state whirl analysis: Non-dimensional whirling amplitude (r/e) vs. time curve for superelastic SMA shaft [Shaft specification w.r.t section 4.2, m = 300 g, ξ = 0.05, β = 1].

Figure 4.34: Unsteady-state whirl analysis: Non-dimensional whirling amplitude (r/e) vs. time curve for superelastic SMA shaft [Shaft specification w.r.t section 4.2, m = 300 g, ξ = 0.05, β = 1.5].

Figure 4.35: Unsteady-state whirl analysis: Non-dimensional whirling amplitude (r/e) vs. time curve for superelastic SMA shaft [Shaft specification w.r.t section 4.2, $m = 300$ g, $\xi = 0.05$, $\beta = 2$].
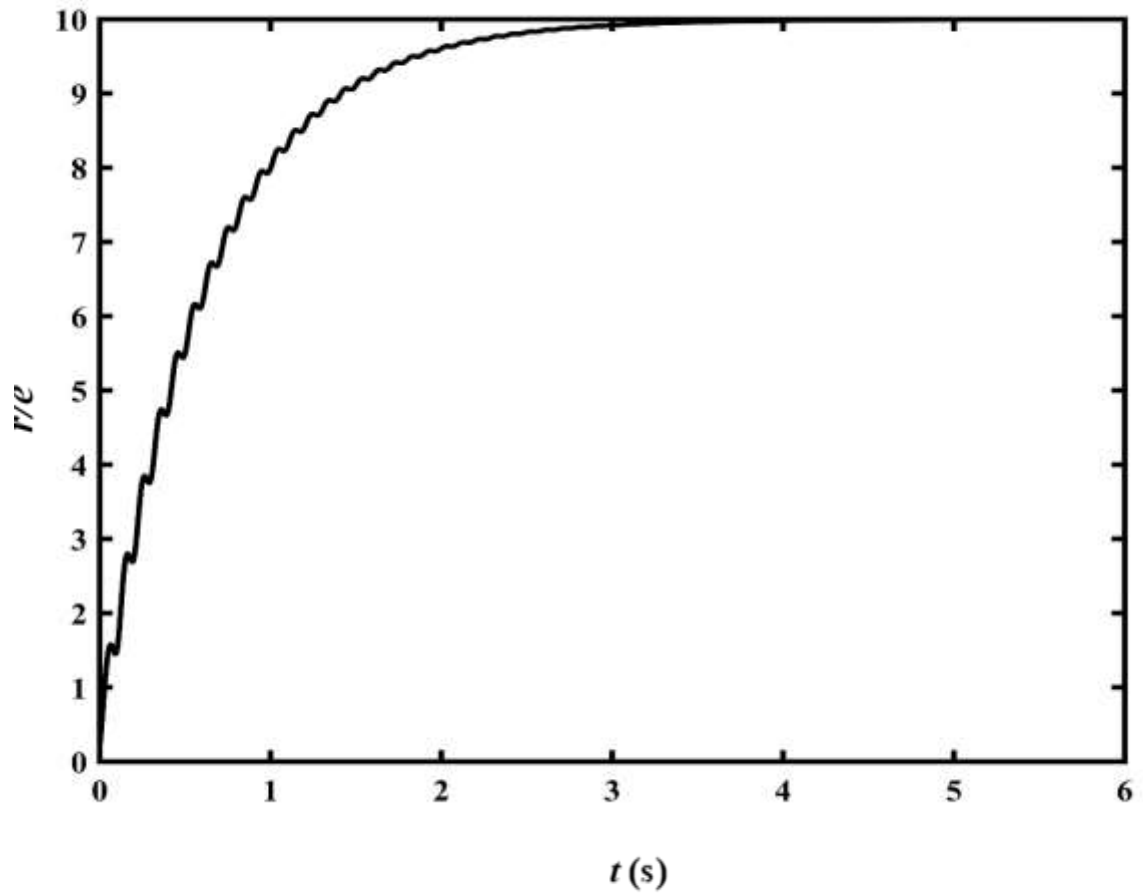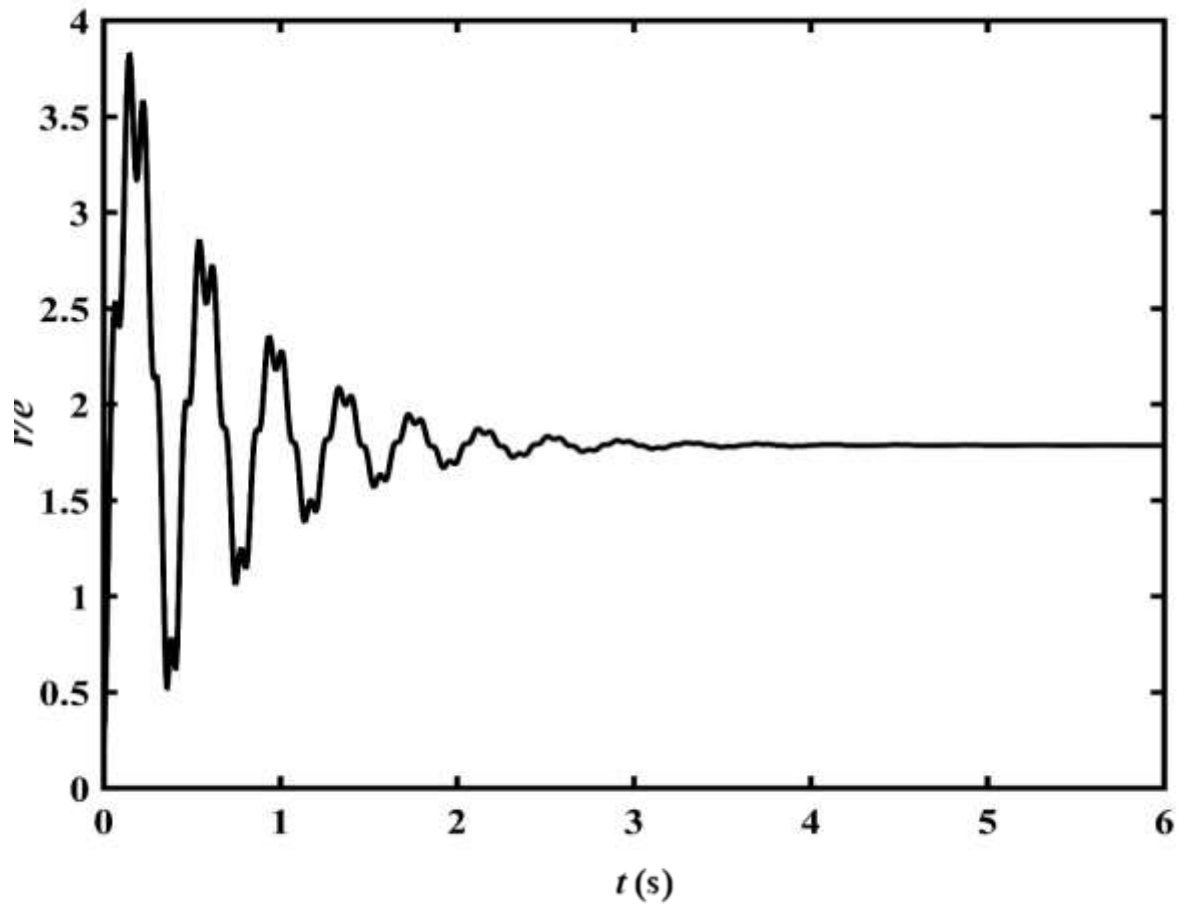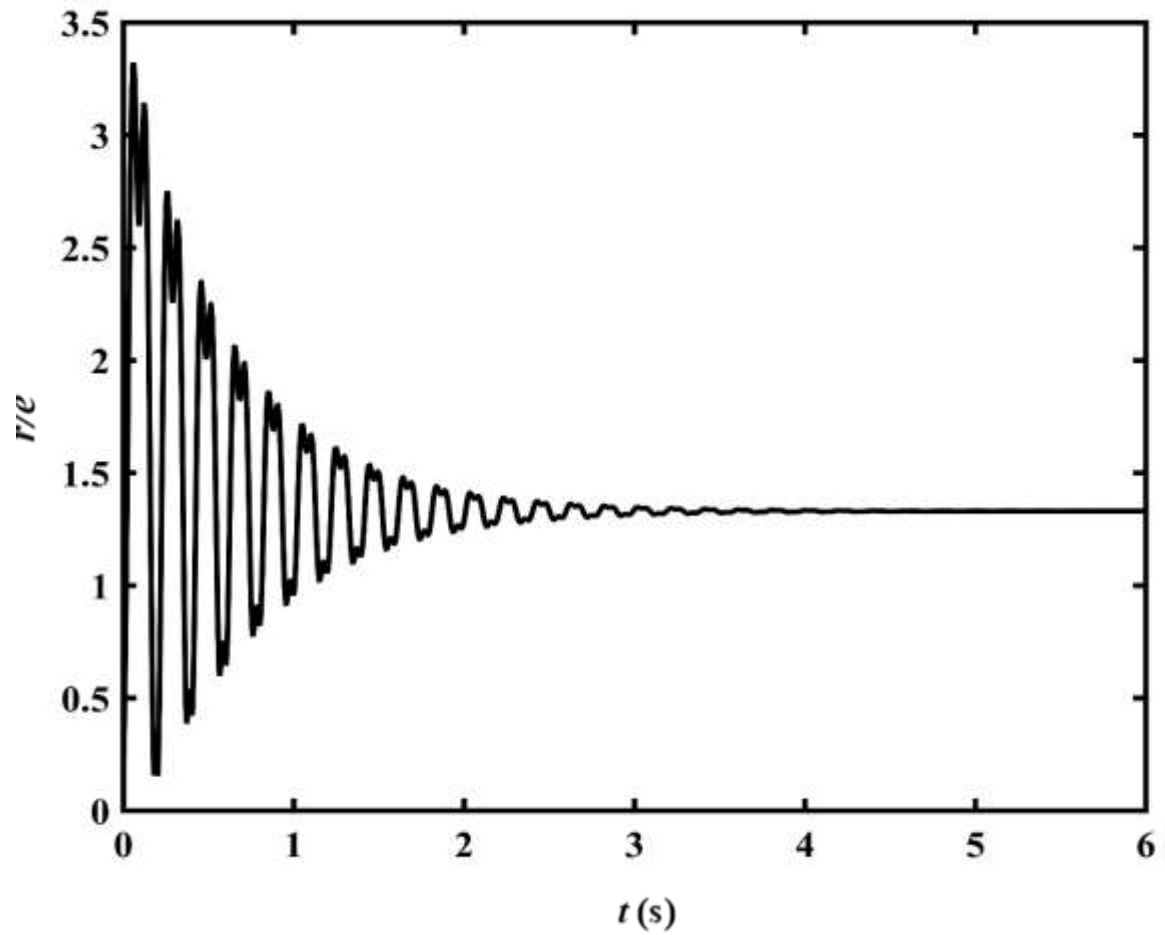
Figure 4.36: Unsteady-state whirl analysis: Non-dimensional whirling amplitude (r/e) vs. time curve for superelastic SMA shaft [Shaft specification w.r.t section 4.2, m = 300 g, ξ = 0.05, β = 5].
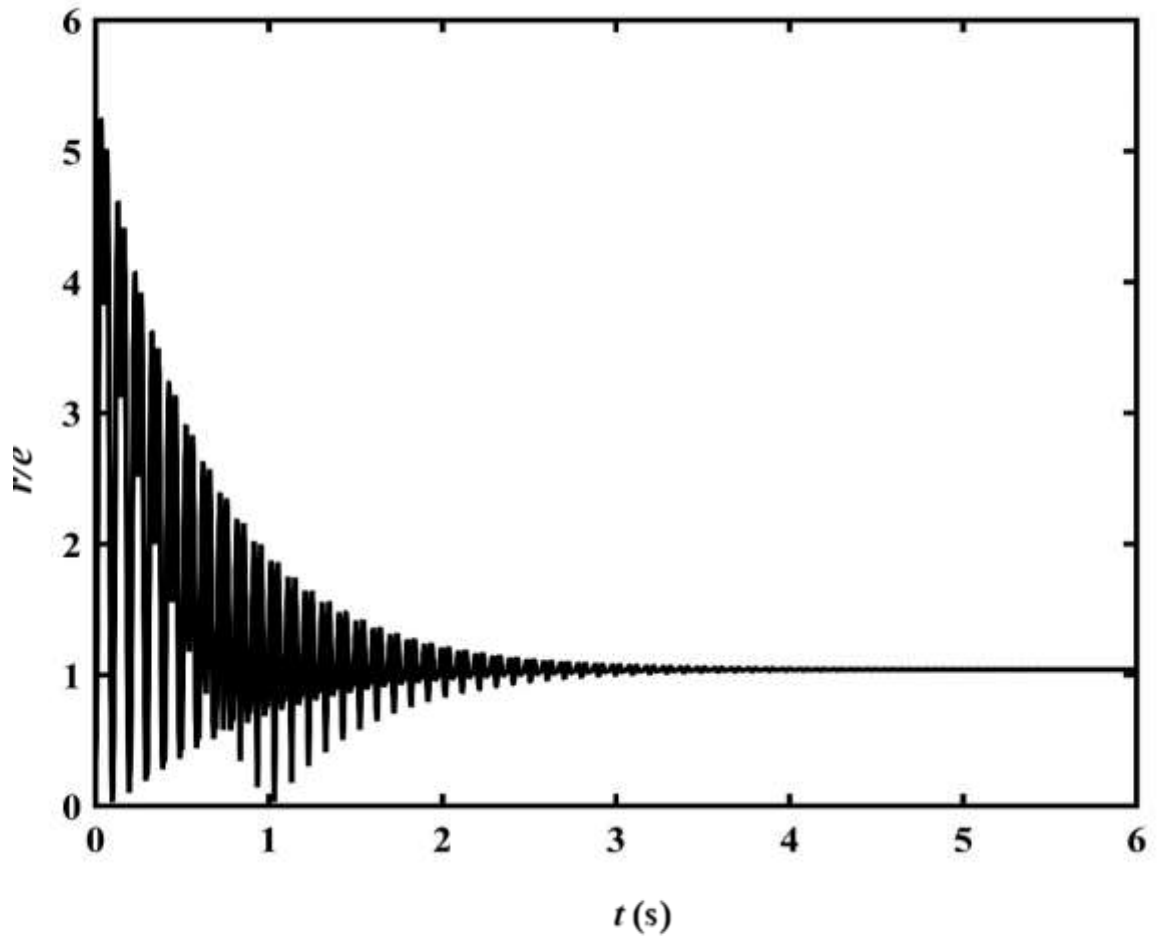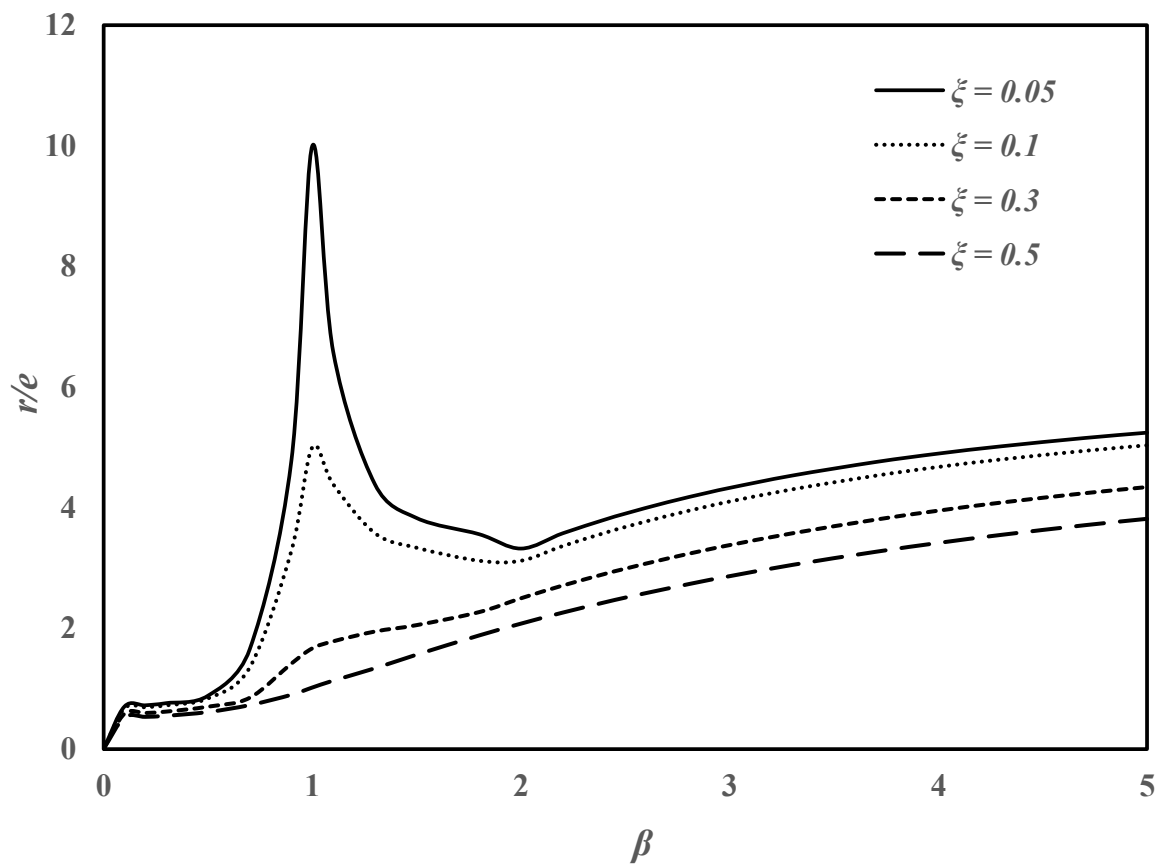
Figure 4.37: Unsteady-state whirl analysis: Maximum non-dimensional Whirling amplitude (r/e) vs. spin ratio (β) for different damping ratio (ξ) for superelastic SMA shaft [Shaft specification w.r.t section 4.2].
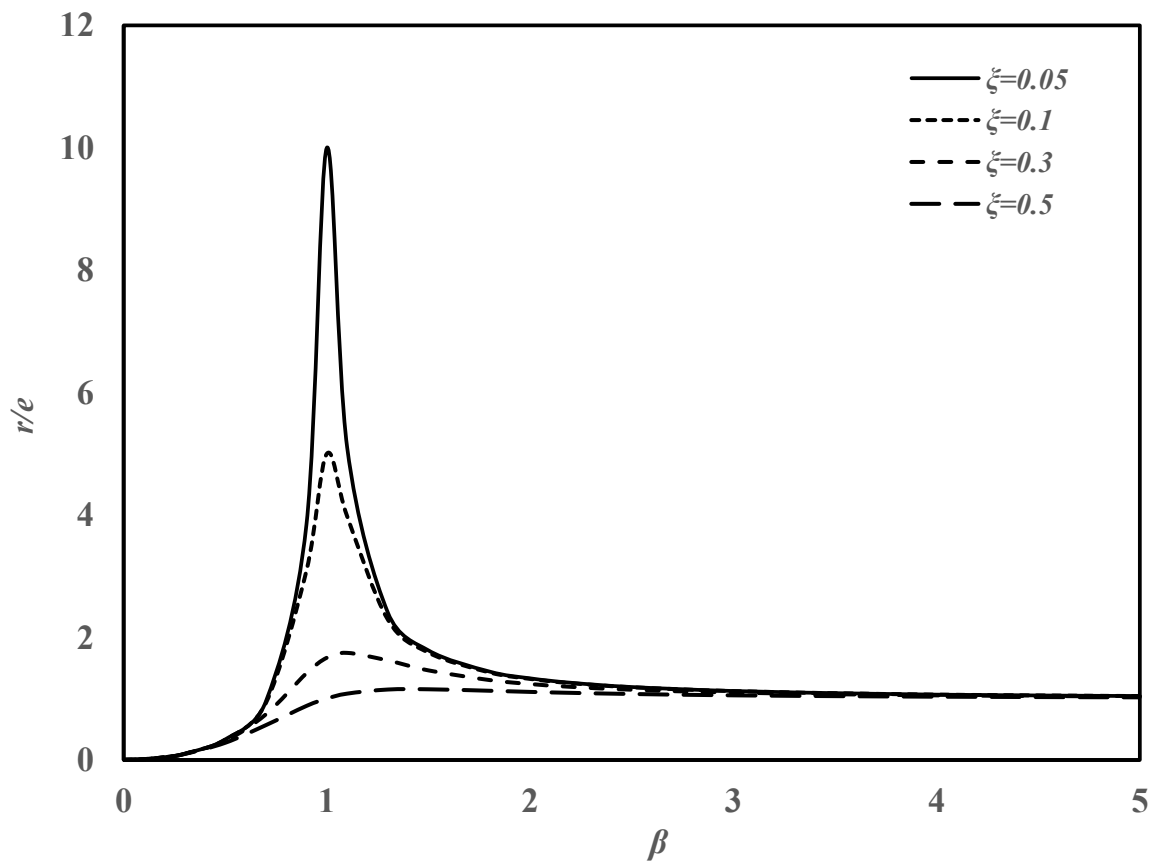
Figure 4.38: Unsteady-state whirl analysis: Maximum non-dimensional whirling amplitude (r/e) vs. spin ratio (β) after transient period for different damping ratio (ξ) for superelastic SMA shaft [Shaft specification w.r.t section 4.2].

Figure 4.39: Unsteady-state whirl analysis: Whirling amplitude (r) vs. spin ratio (β) curve for superelastic SMA shaft for different eccentricity [Shaft specification w.r.t section 4.2, $\xi = 0.05$].
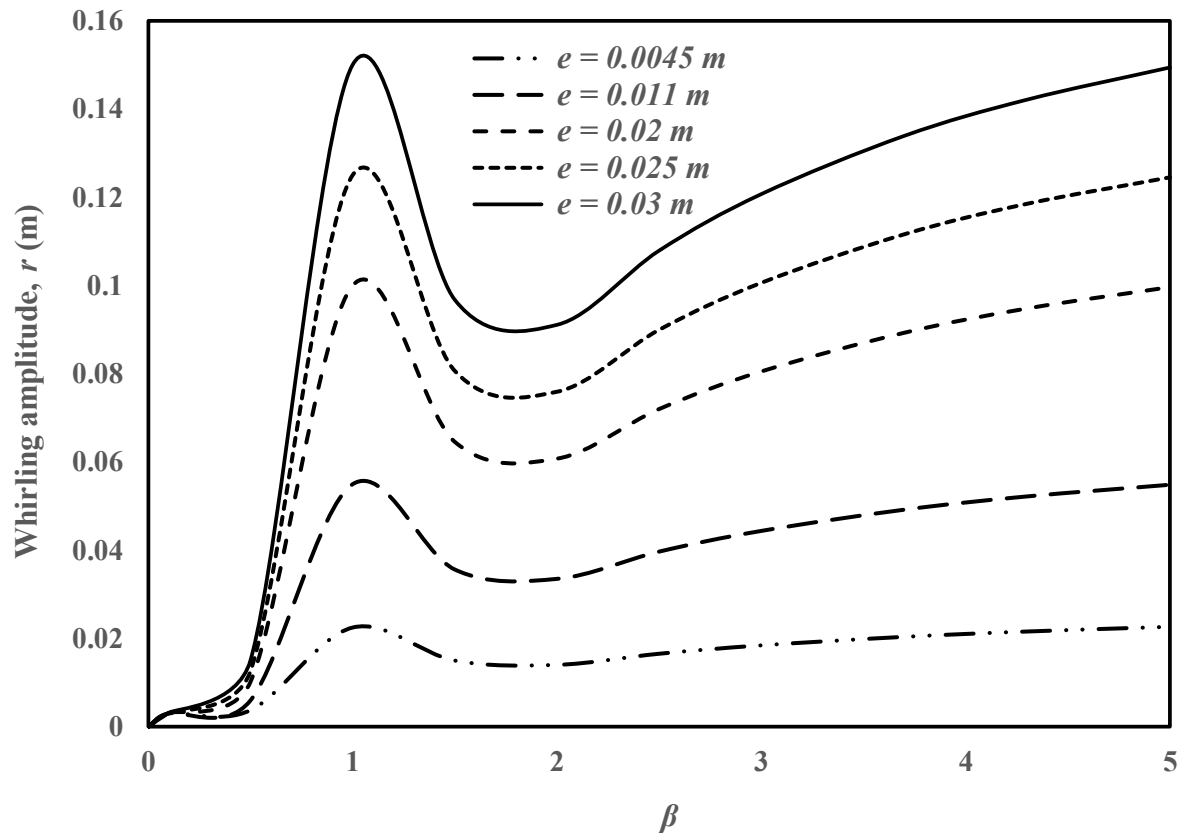
Figure 4.40: Unsteady-state whirl analysis: Whirling amplitude (r) vs. spin ratio (β) curve for superelastic SMA shaft for different eccentricity [Shaft specification w.r.t section 4.2, $\xi = 0.1$].
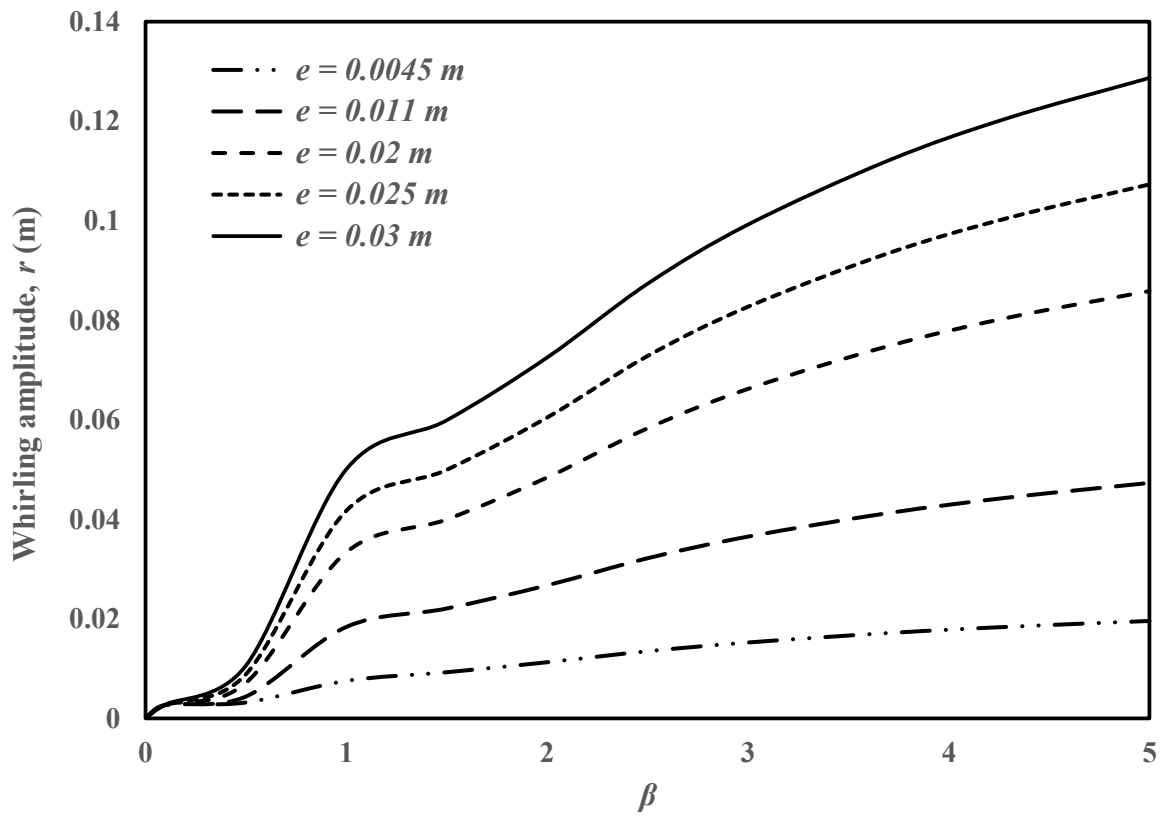
Figure 4.41: Unsteady-state whirl analysis: Whirling amplitude (r) vs. spin ratio (β) curve for superelastic SMA shaft for different eccentricity [Shaft specification w.r.t section 4.2, $\xi = 0.3$].
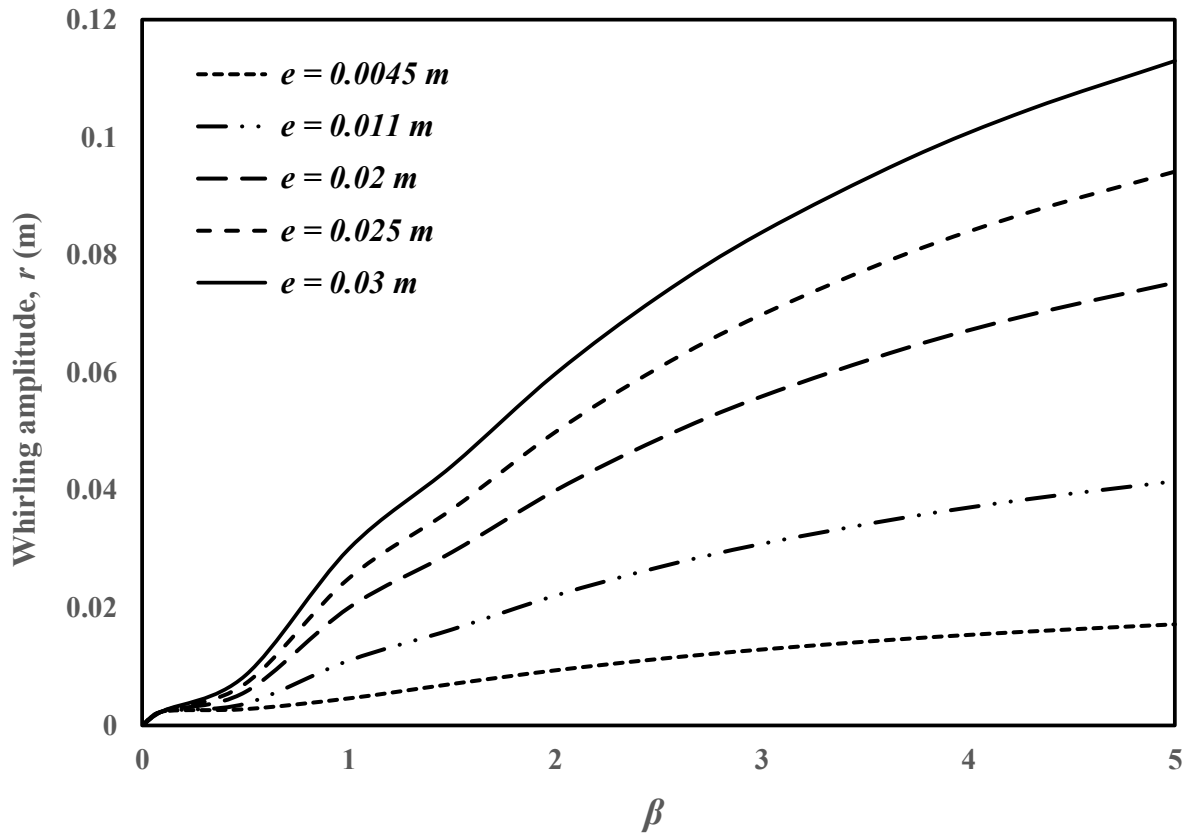
Figure 4.42: Unsteady-state whirl analysis: Whirling amplitude (r) vs. spin ratio (β) curve for superelastic SMA shaft for different eccentricity [Shaft specification w.r.t section 4.2, $\xi = 0.5$].
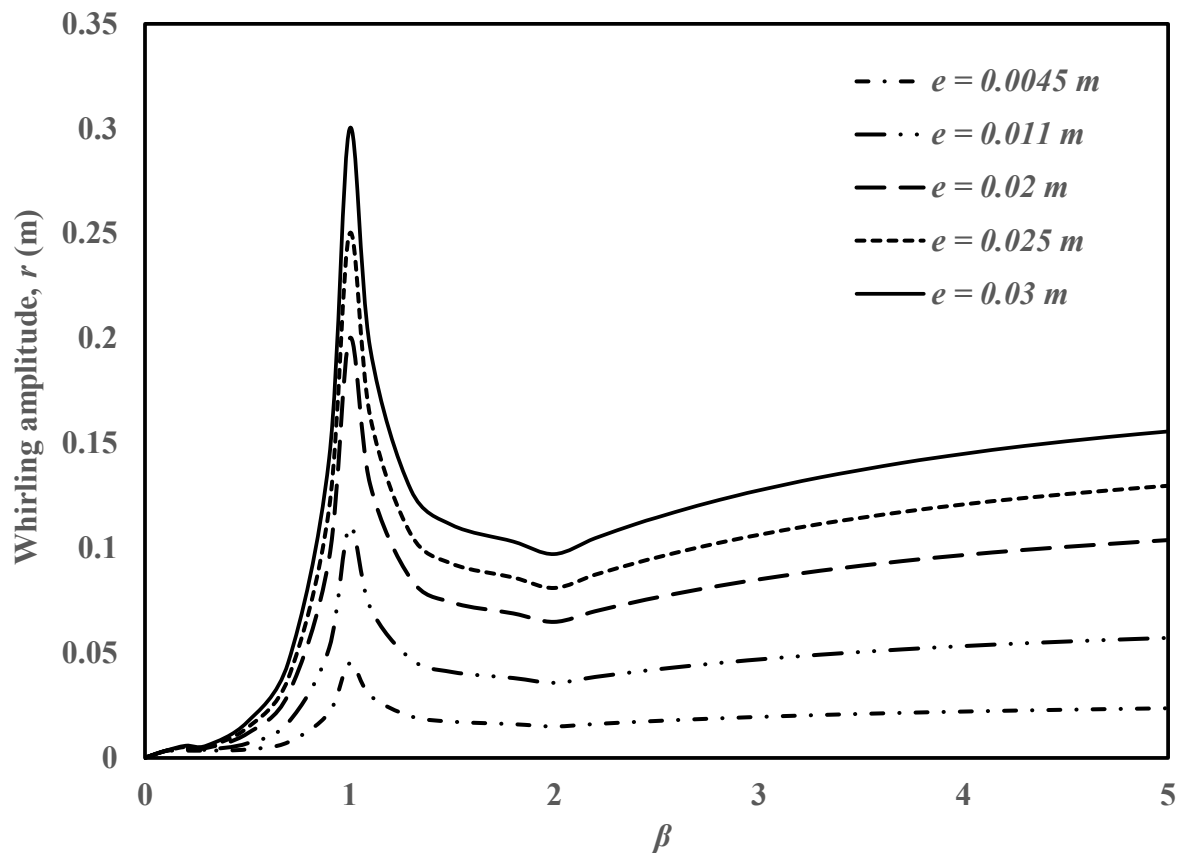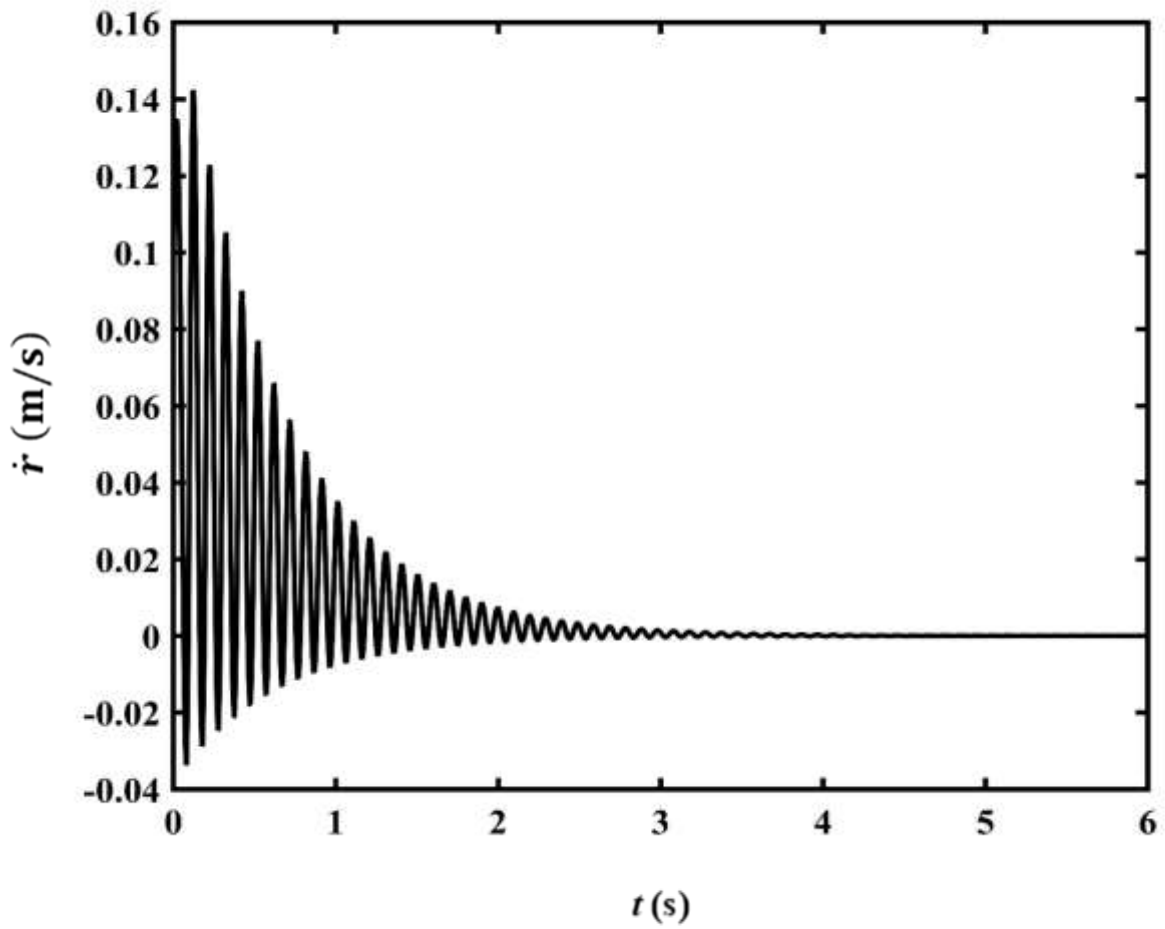
Figure 4.43: Unsteady-state whirl analysis: Radial velocity ($\dot{r}$) vs. time (t) curve for superelastic SMA shaft. [Shaft specification w.r.t section 4.2, $\xi = 0.05$, $\beta = 1$].
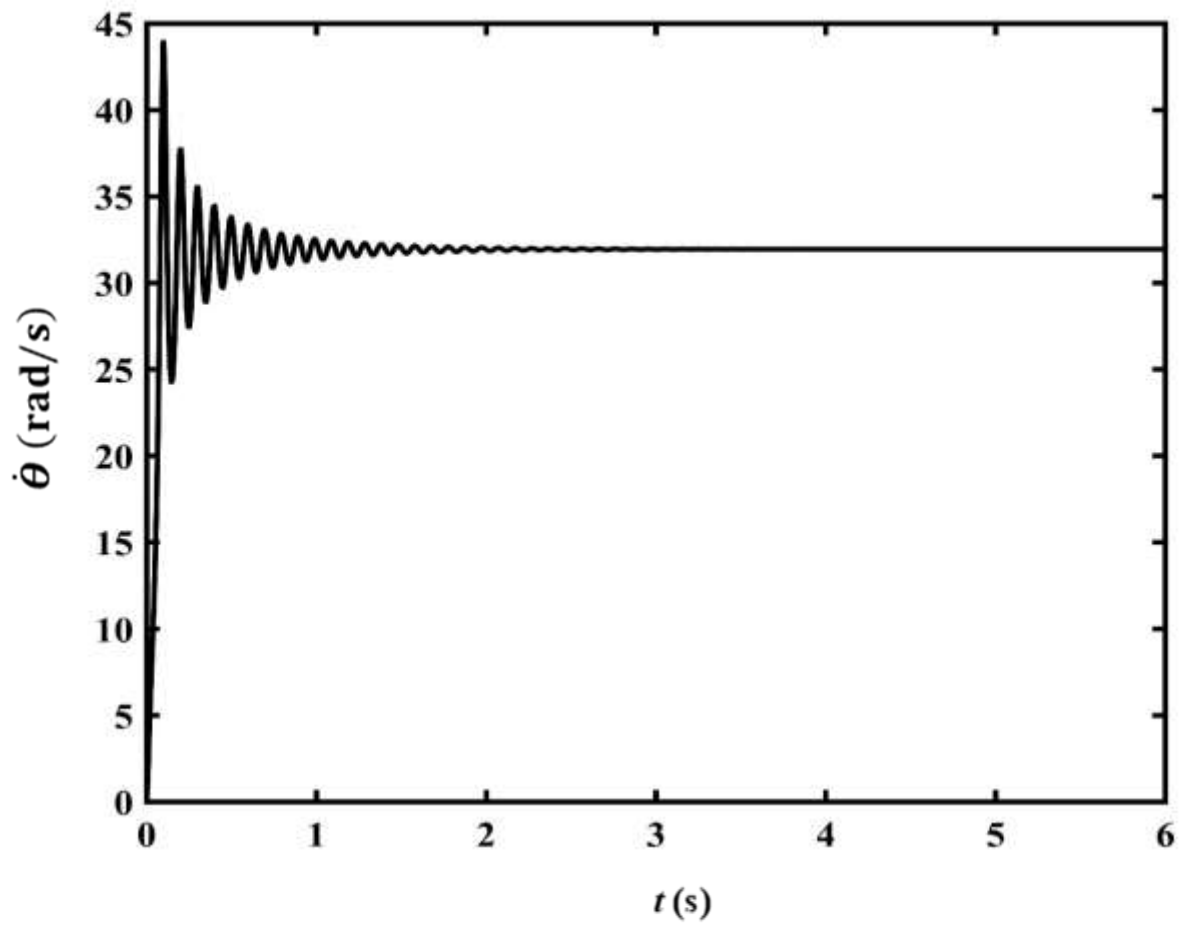
Figure 4.44: Unsteady-state whirl analysis: Whirl speed $(\dot{\theta})$ vs. time (t) curve for superelastic SMA shaft. [Shaft specification w.r.t section 4.2, $\xi = 0.05$, $\beta = 1$].

Figure 4.45: Unsteady-state whirl analysis: Non-dimensional dynamic force (P_d/mg) w.r.t maximum whirling amplitude (r) vs. spin ratio (β) curve for different damping ratio (ξ) superelastic SMA shaft [Shaft specification w.r.t section 4.2].
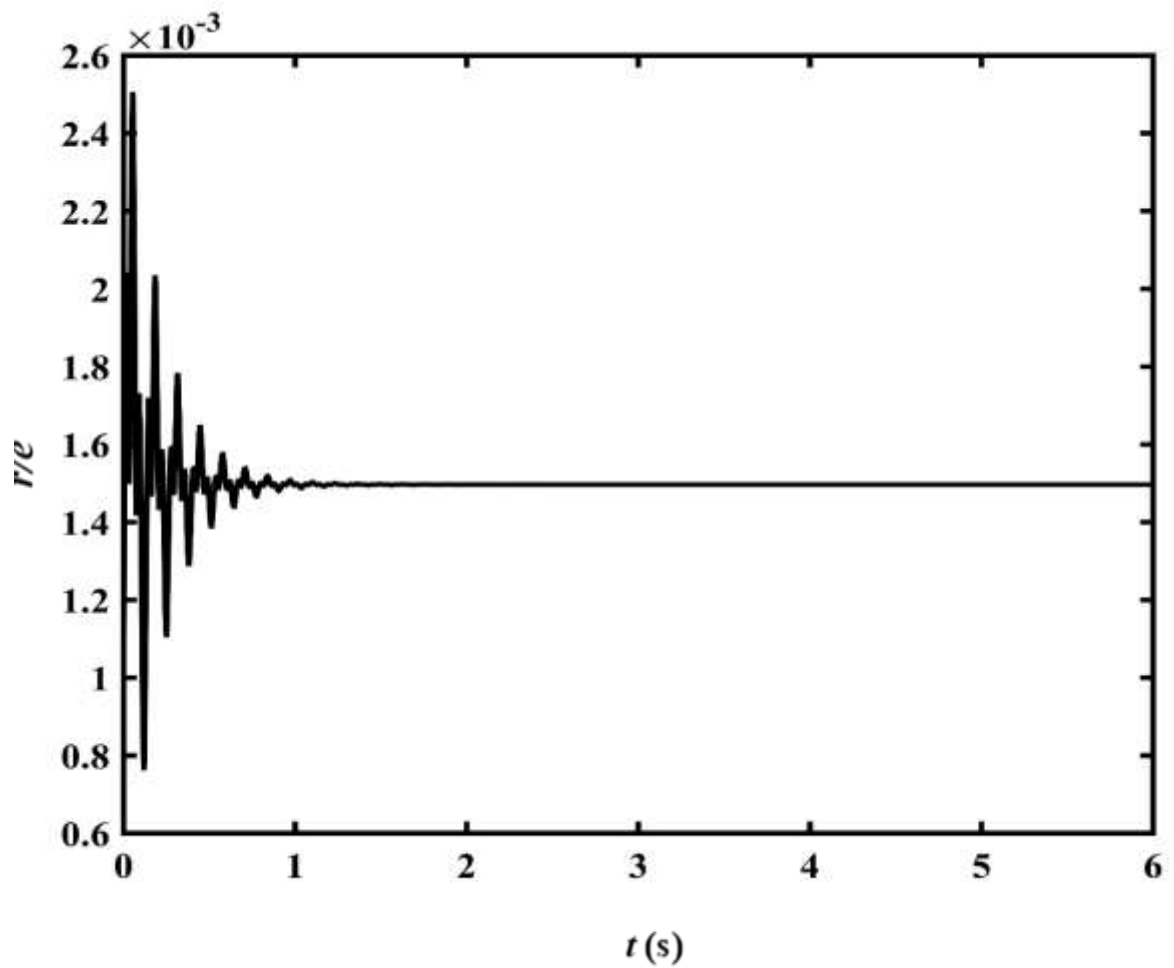
Figure 4.46: Unsteady-state whirl analysis: Non-dimensional whirling amplitude (r/e) vs. time curve for Stainless steel shaft [Shaft specification w.r.t. section 4.5,$\xi = 0.05$, $\beta = 0.5$].
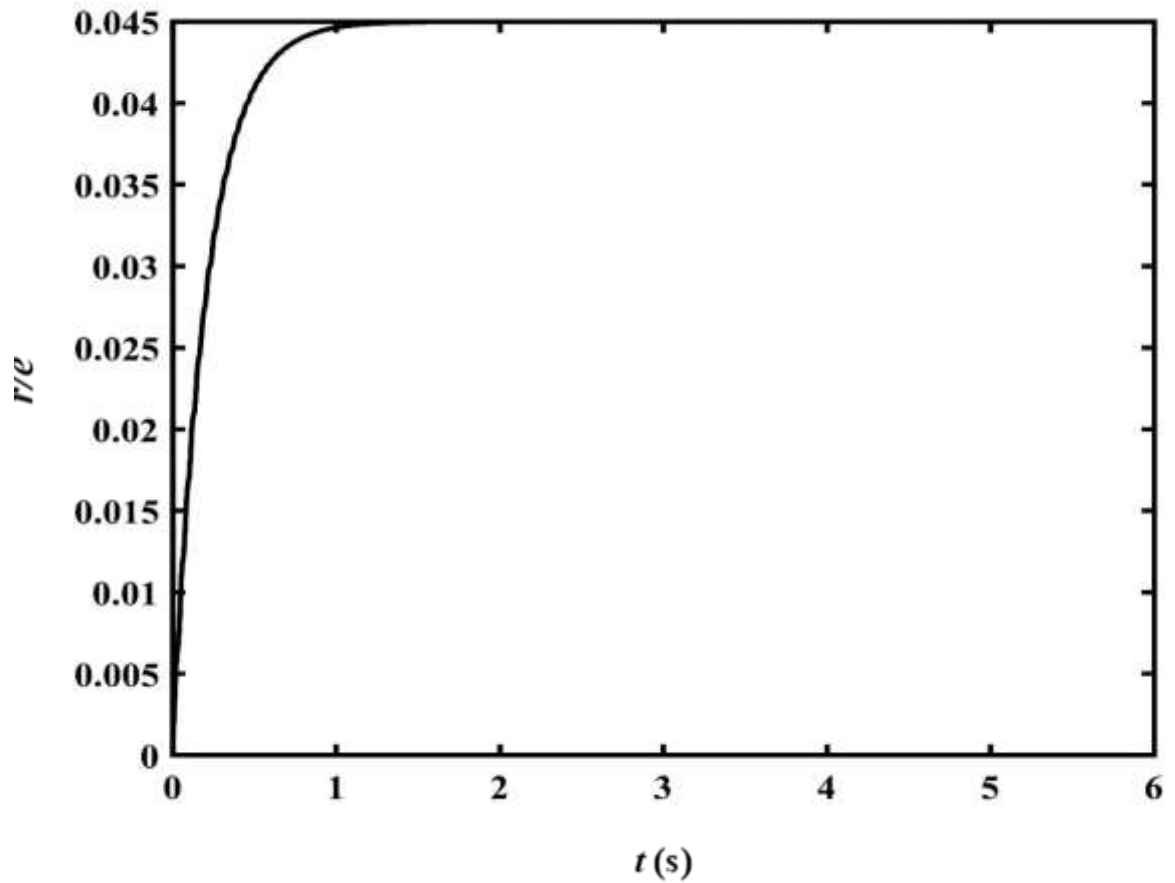
Figure 4.47: Unsteady-state whirl analysis: Non-dimensional whirling amplitude (r/e) vs. time curve for Stainless steel shaft [Shaft specification w.r.t. section 4.5, $m = 300$ g, $\xi = 0.05$, $\beta = 1$].
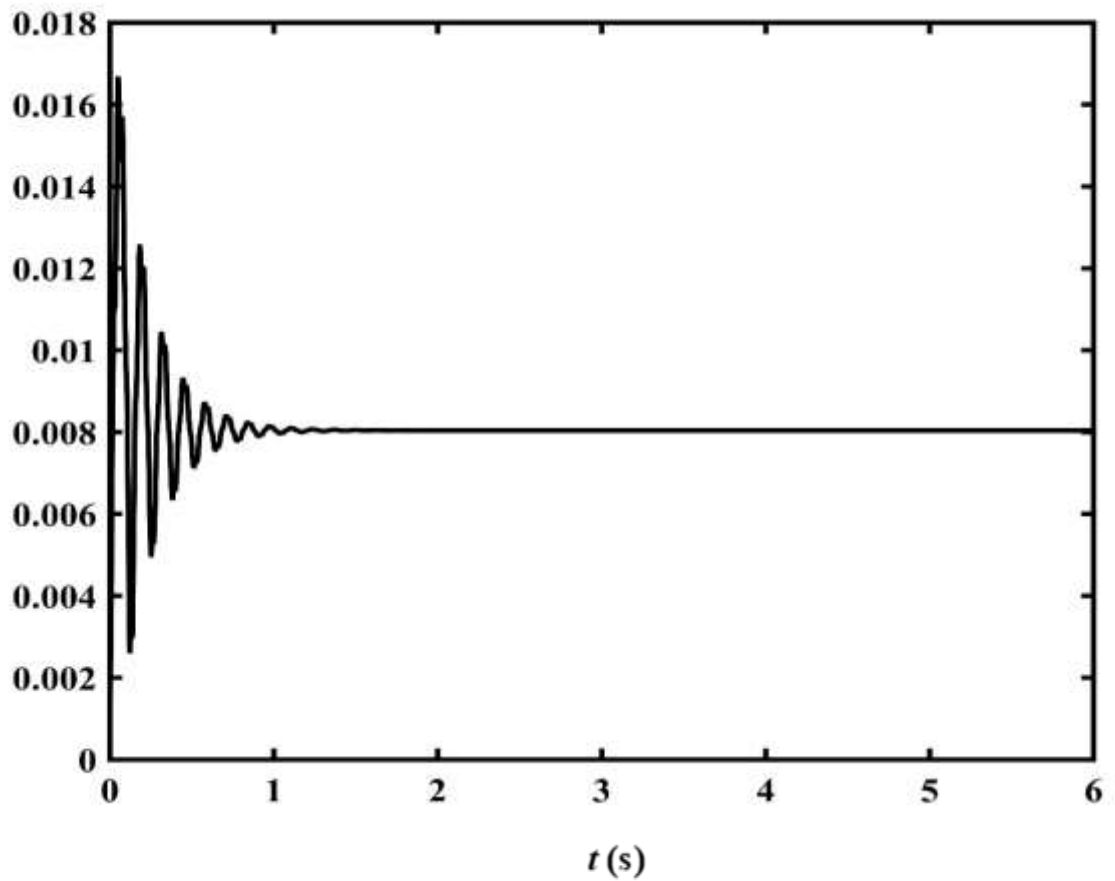
Figure 4.48: Unsteady-state whirl analysis: Non-dimensional whirling amplitude (r/e) vs. time curve for Stainless steel shaft [Shaft specification w.r.t. section 4.5, $m = 300$ g, $\xi = 0.05$, $\beta = 1.5$].
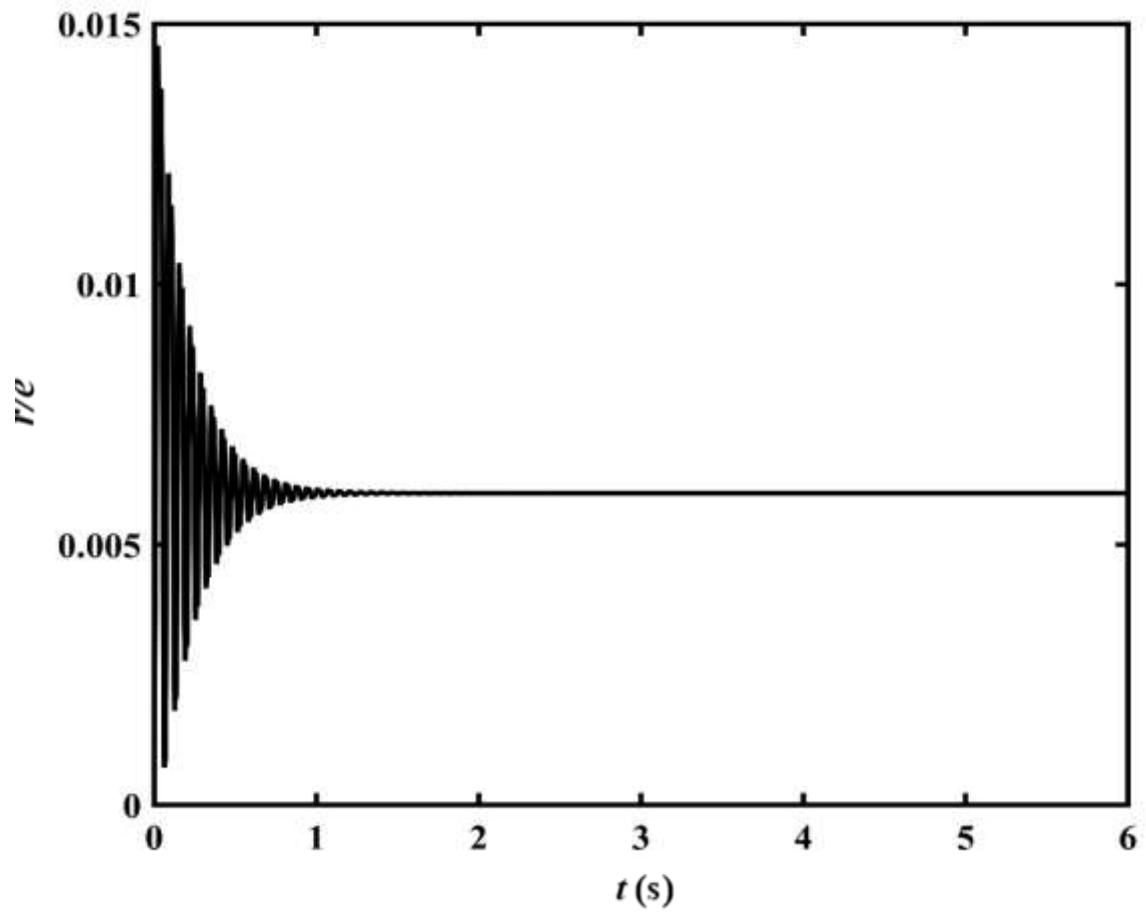
Figure 4.49: Unsteady-state whirl analysis: Non-dimensional whirling amplitude (r/e) vs. time curve for Stainless steel shaft [Shaft specification w.r.t. section 4.5, $m = 300$ g, $\xi = 0.05$, $\beta = 2$].
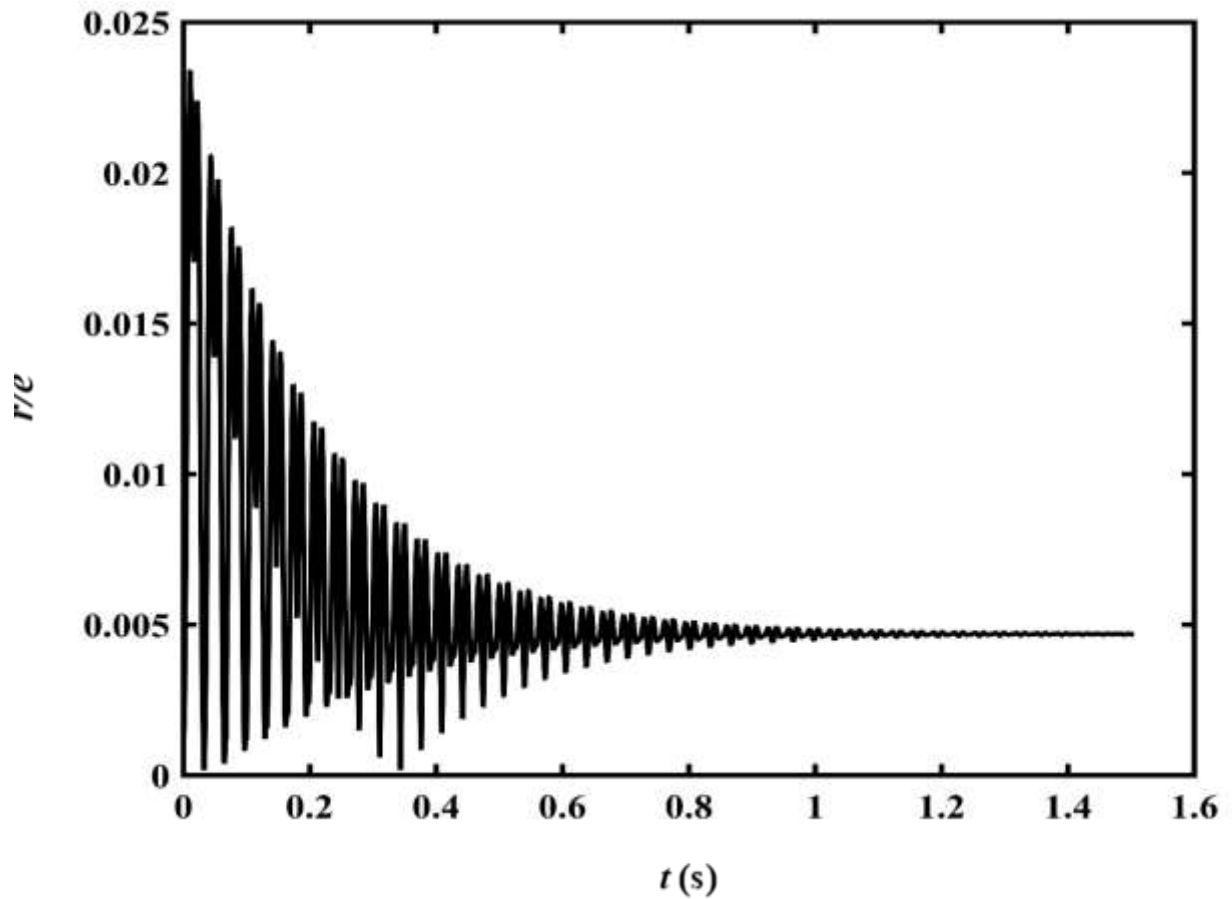
Figure 4.50: Unsteady-state whirl analysis: Non-dimensional whirling amplitude (r/e) vs. time curve for Stainless steel shaft [Shaft specification w.r.t. section 4.5, m = 300 g, ξ = 0.05, β = 5].
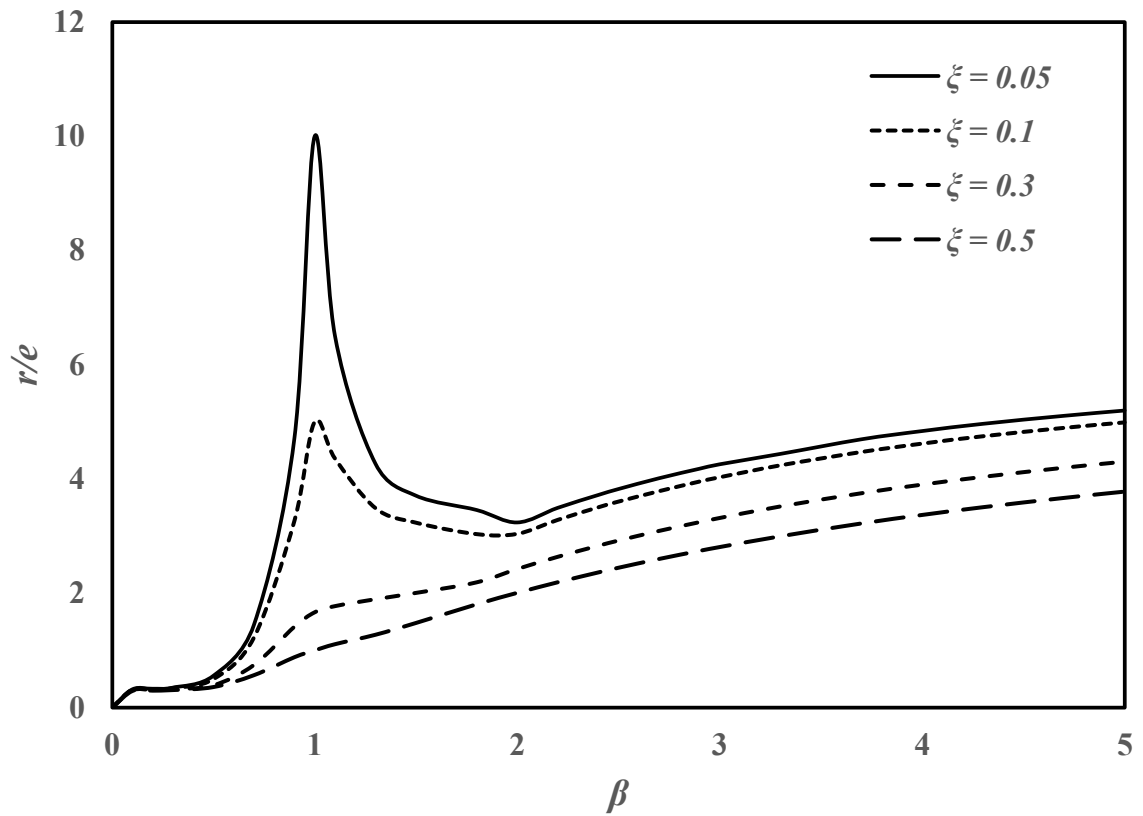
Figure 4.51: Unsteady-state whirl analysis: Maximum non-dimensional whirling amplitude (r/e) vs. spin ratio (β) for different damping ratio (ξ) for Stainless steel shaft [Shaft specification w.r.t section 4.5].
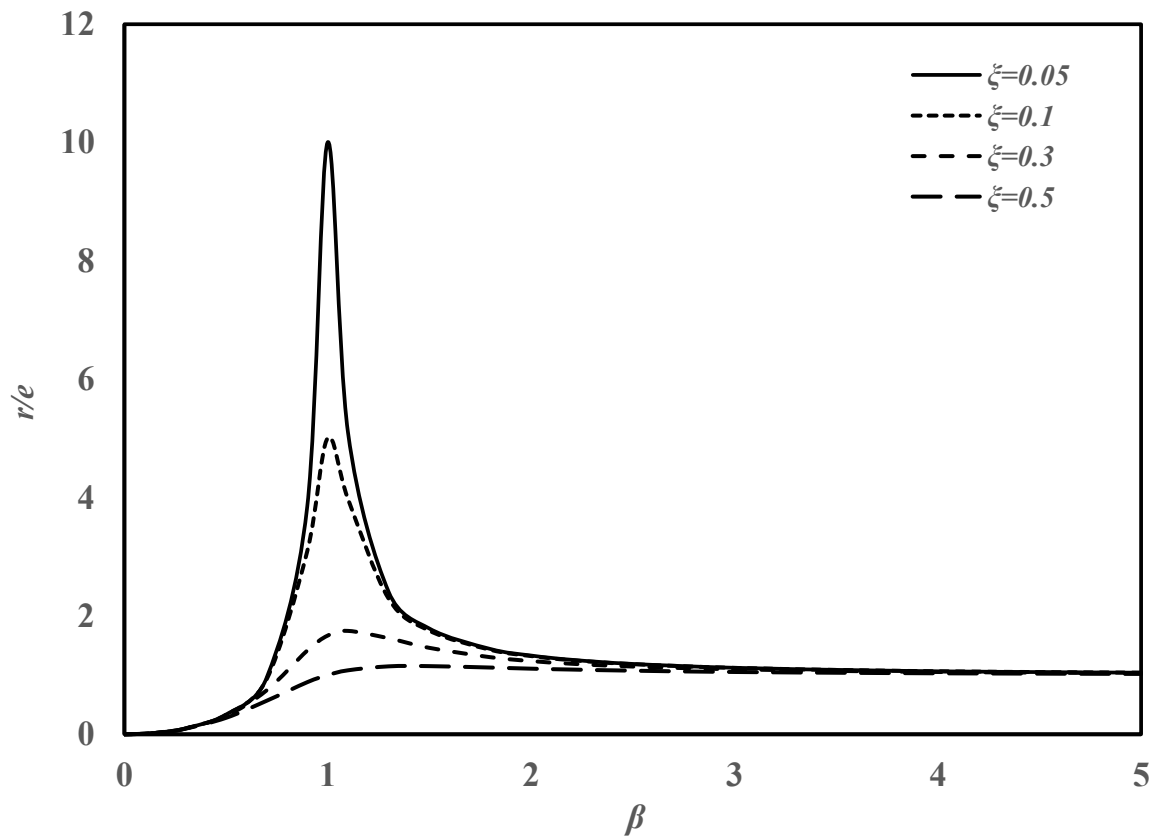
Figure 4.52: Unsteady-state whirl analysis: Maximum non-dimensional whirling amplitude (r/e) vs. spin ratio (β) after transient period for different damping ratio (ξ) for Stainless steel shaft [Shaft specification w.r.t section 4.5].
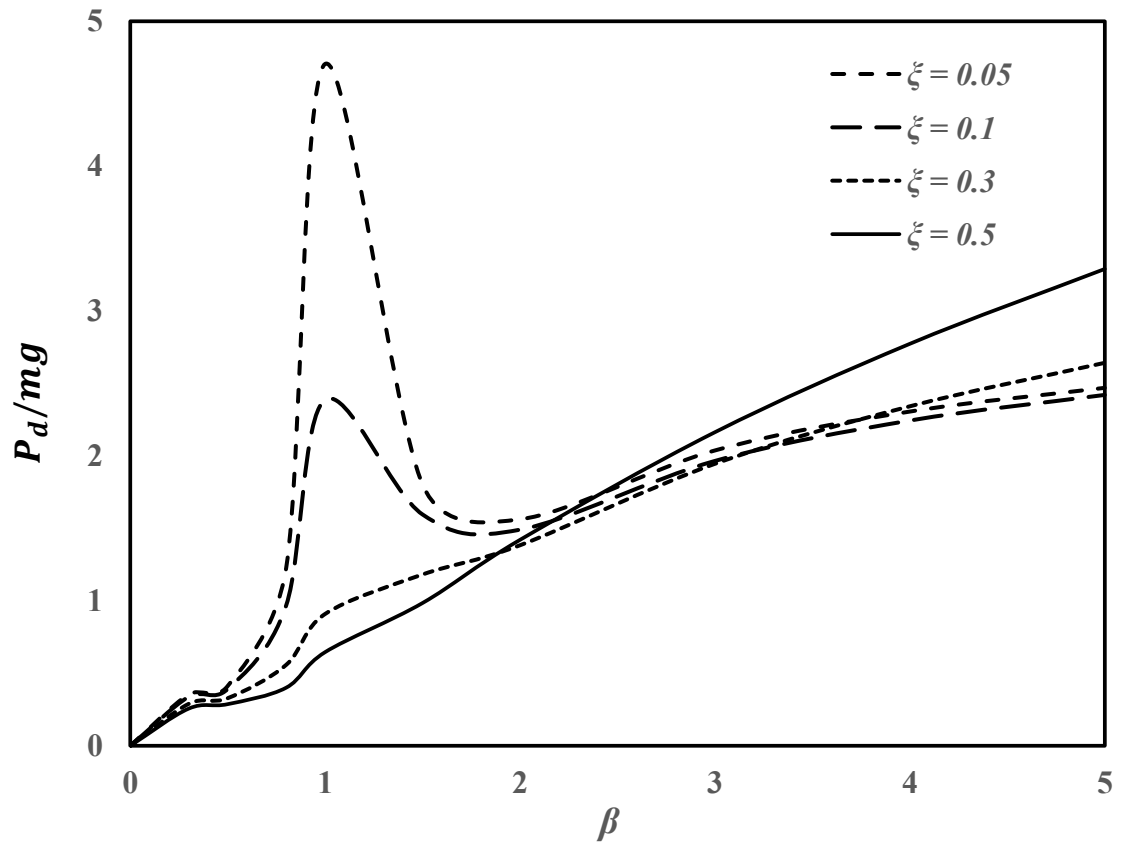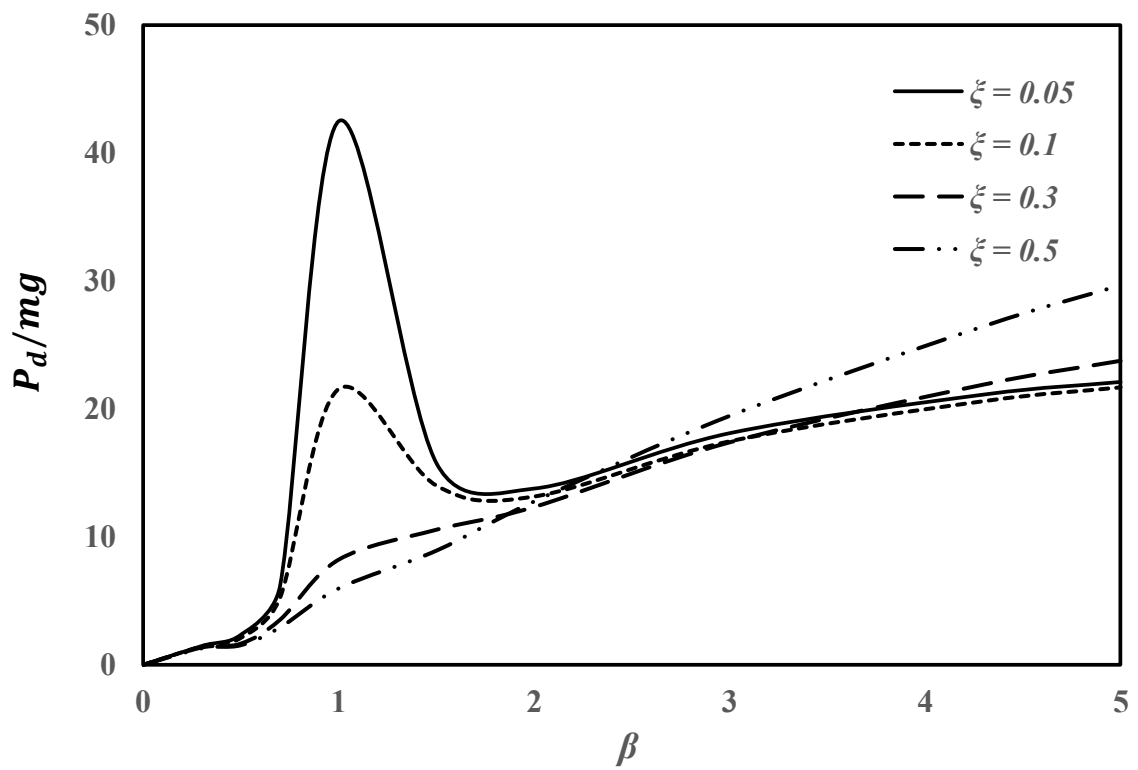
Figure: 4.53: Unsteady-state whirl analysis: Non-dimensional dynamic force (P_d/mg) w.r.t maximum whirling amplitude (r) vs. spin ratio (β) curve for different damping ratio (ξ) for Stainless steel shaft [Shaft specification w.r.t section 4.5].

Test Specimen (SS shaft)

Bores for using
different length shafts

Structure made of MS plate

Control unit   Disc   Drill chucks used as holders
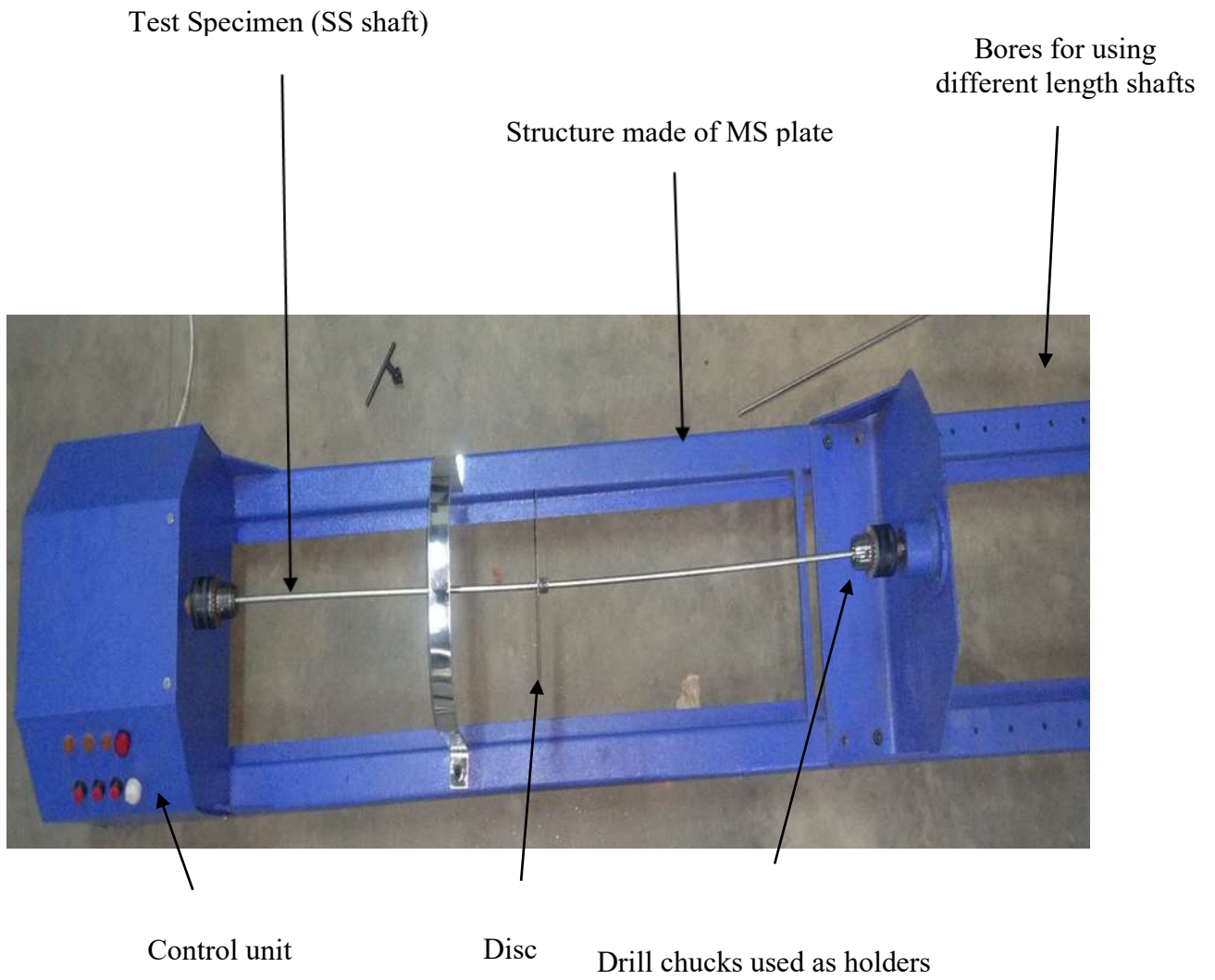
Figure 4.54: Experimental whirl test set-up.
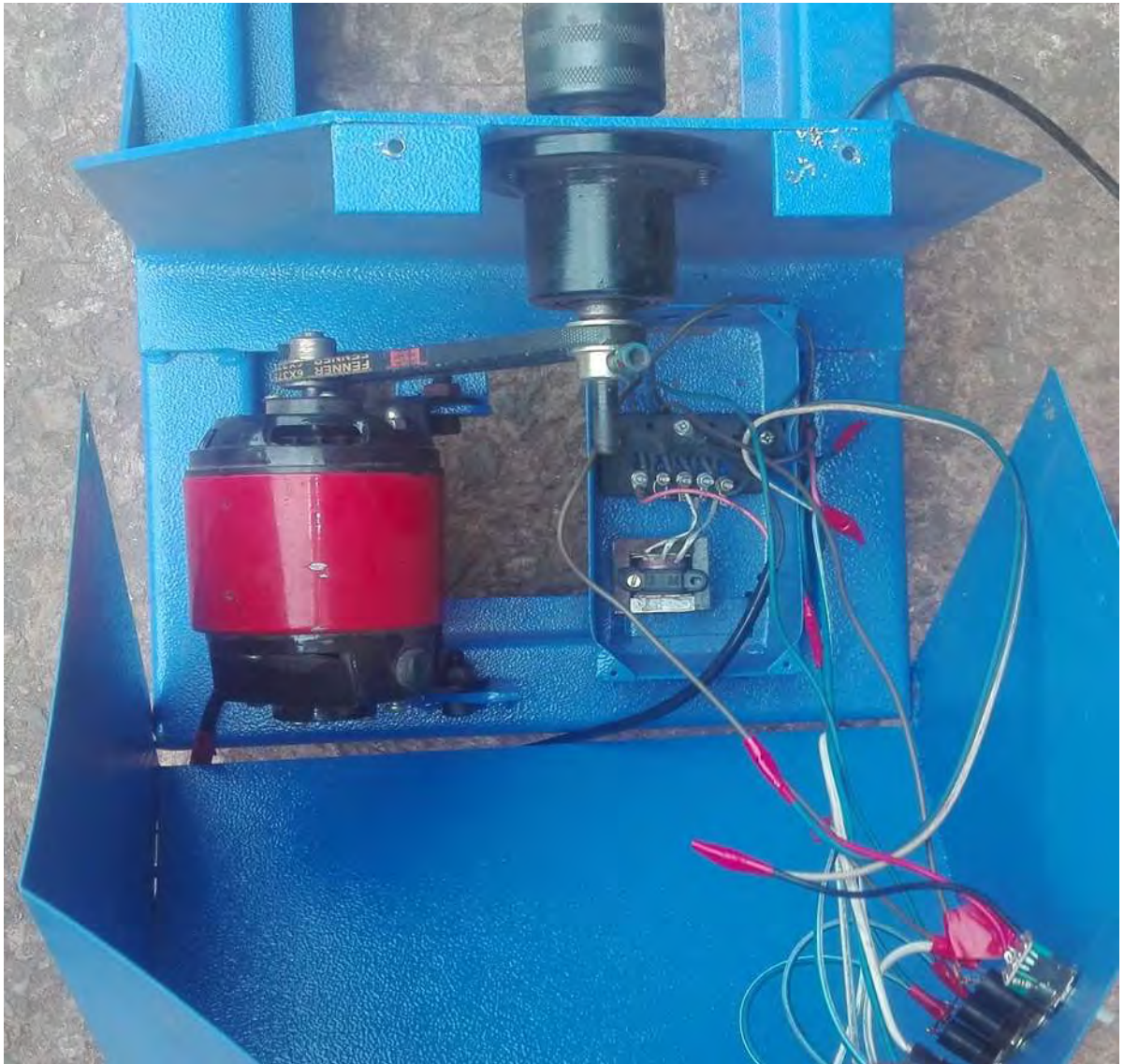
Figure 4.55: Control unit of the set-up.
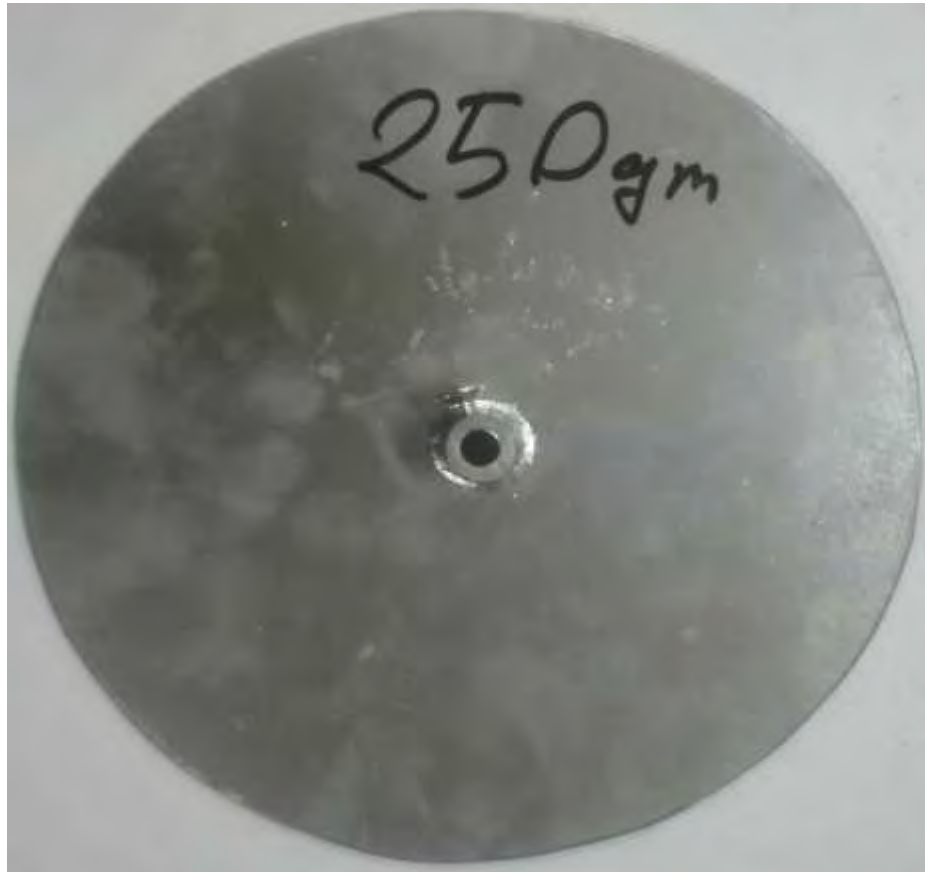
Figure 4.56: Circular disc of variable mass and diameter [Disc mass = 250 g, dia = 15.4 cm].

(Before experiment)

(After experiment)

Figure 4.57: Shaft's shapes before and after experiment [dia = 8 mm, disc mass 250 g, ω = 253 rpm, β = 0.25].

(Before experiment)

(After experiment)

Figure 4.58: Shaft's shapes before and after experiment [Shaft dia = 0.008 m, disc mass = 250 g, ω = 2298 rpm, $\beta = 2.29$].

(Before experiment)

(After experiment)

Figure 4.59: Shaft's shapes before and after experiment [Shaft dia = 0.008 m, Disc mass = 250 g, ω = 1133 rpm, β = 1.13].

(Before experiment)

(After experiment)

Figure 4.60: Shaft's shapes before and after experiment [Shaft dia = 0.006 m, disc mass = 250 g, ω = 531 rpm, β = 0.94].

APPENDIX - A

Steady-state Synchronous and Asynchronous Whirl (Whirling Amplitude Calculation at High Spin Ratio)

Equation of steady-state (synchronous and asynchronous) non-dimensional whirling amplitude is

$$\frac{r}{e} = \frac{\lambda^2 \beta^2}{\sqrt{(1-\lambda^2\beta^2)^2 + (2\xi\beta\lambda)^2}} \quad \text{......................................(1)}$$

Dividing both numerator and denominator of R.H.S of equation 1, we obtain,

$$\frac{r}{e} = \frac{1}{\sqrt{\frac{(1-\lambda^2\beta^2)^2 + (2\xi\beta\lambda)^2}{\lambda^4\beta^4}}}$$

$$\text{Or,} \quad \frac{r}{e} = \frac{1}{\sqrt{\left(\frac{1}{\lambda^2\beta^2}-1\right)^2 + \left(\frac{2\xi\beta\lambda}{\lambda^2\beta^2}\right)^2}} \quad \text{......................(2)}$$

From equation 2, if $\beta \gg 0$, $\frac{r}{e} \approx 1$.

APPENDIX - B

Steady-state Synchronous and Asynchronous Whirl (Force Calculation)

Equation of steady-state (synchronous and asynchronous) non-dimensional dynamic force is

$$\frac{P_d}{mg} = \frac{\sqrt{(kr)^2 + (c\lambda\omega r)^2}}{mg} \ldots\ldots\ldots\ldots..(1)$$

For superelastic SMA shaft (shaft specification w.r.t. section 4.2), for $\xi = 0.05$, $\lambda = 1$ (synchronous whirl condition), and $\beta = 1.414$,

$$P_d/mg = 0.94$$

Similarly, for $\xi = 0.1$, $\lambda = 1$, & $\beta = 1.414$,

$$P_d/mg = 0.94$$

For $\xi = 0.3$, $\lambda = 1$ & $\beta = 1.414$,

$$P_d/mg = 0.94$$

Therefore, all curves in (P_d/mg vs. β) Figure for synchronous whirl condition for any value of damping ratio intersect each other for a specific value of spin ratio ($\beta = 1.414$).

APPENDIX - C

Steady-state Synchronous and Asynchronous Whirl (Maximum whirling amplitude *r/e* calculation for a particular damping ratio)

Equation of steady-state (synchronous and asynchronous) non-dimensional whirling amplitude is

$$y = \frac{r}{e} = \frac{\lambda^2 \beta^2}{\sqrt{(1-\lambda^2\beta^2)^2 + (2\xi\beta\lambda)^2}} \quad \ldots\ldots\ldots\ldots\ldots\ldots\ldots\ldots..(1)$$

Differentiating both sides of Equation 1 w.r.t β,

$$\frac{dy}{d\beta} = \frac{2\lambda^2\beta\sqrt{(1-\lambda^2\beta^2)^2+(2\xi\lambda\beta)^2} - \lambda^2\beta^2\left[\dfrac{-4\lambda^2\beta(1-\lambda^2\beta^2)+8\lambda^2\xi^2\beta}{2\sqrt{(1-\lambda^2\beta^2)^2+(2\xi\lambda\beta)^2}}\right]}{(1-\lambda^2\beta^2)^2+(2\xi\beta\lambda)^2} \ldots\ldots\ldots\ldots\ldots(2)$$

For maximum whirling amplitude (*r/e*), $\frac{dy}{d\beta} = 0$.

Therefore, from Equation 2,

$$4\lambda^2\beta\{(1 - \lambda^2\beta^2)^2 + (2\xi\lambda\beta)^2\} - \lambda^2\beta^2\{-4\lambda^2\beta(1 - \lambda^2\beta^2) + 8\lambda^2\xi^2\beta\} = 0 \ldots\ldots(3)$$

Solving Equation 3,

$$\beta = \frac{1}{\lambda\sqrt{1-2\xi^2}} \ldots\ldots\ldots\ldots.(4)$$

For $\lambda = 1$ (Synchronous whirl condition) and $\xi = 0.05$,

$$\beta = 1.003$$

Putting value of $\beta = 1.003$, $\lambda = 1$ (Synchronous whirl condition) and $\xi = 0.05$ in Equation 1, corresponding non-dimensional whirling amplitude (r/e) is 10 for synchronous whirl condition.

For $\lambda = 2$ (Asynchronous whirl condition) and $\xi = 0.05$, from Equation 4,

$$\beta = 0.5013$$

Putting value of $\beta = 0.5013$, $\lambda = 2$ (Asynchronous whirl condition) and $\xi = 0.05$ in Equation 1, corresponding non-dimensional whirling amplitude (r/e) is 10 for asynchronous whirl condition.

APPENDIX - D

Moment Area Method

Two theorems of this method are used to predict the whirling shafts' shapes in this thesis. Brief description is provided in terms of Figures a-c.

Moment-area method - Theorem 1

The change in slope between the tangents drawn to the elastic curve at any two points A and B (Figure b) is equal to the product of $(1/EI)$ multiplied by the area of the moment diagram (Figure c) between these two points.

$$\Theta_{AB} = \frac{1}{EI}(Area_{AB})$$

Moment-area method - Theorem 2

The deviation of any point B relative to the tangent drawn to the elastic curve (Figure c) at any other point A, in a direction perpendicular to the original position of the beam, is equal to the product of $(1/EI)$ multiplied by the moment of an area about B of that part of the moment diagram (Figure b) between points A and B.

$$t_{A/B} = \sum \frac{1}{EI}(Area_{AB}) \bullet \bar{X}_A$$
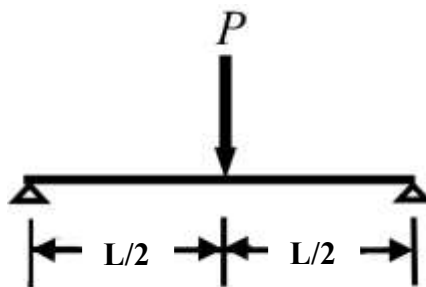
Figure (a): Simply-supported beam with force acting at the mid-span of the shaft.

Here, it is considered that, moment-area method can be applied to the Jeffcott rotor shaft which is whirling. Shaft specification stated in section 4.2 is considered here for the calculation. Maximum total force P = 16.8 N acting at the shaft center is w.r.t. Figure 4.12 is used to calculate the shaft maximum deflection considering material linearity and non-

linearity as well. For linearly elastic model, the change in slope between the tangents drawn to the elastic curve at A and B (Figure b),

$$\theta_{AB} = \int_A^B d\theta = \int_A^B \frac{M}{EI} dx = \frac{1}{2} \times \frac{L}{2} \times \frac{PL}{4EI} = \frac{PL^2}{16EI} = 0.823 \text{ rad.}$$

Figure (b): Elastic curve of a superelastic SMA Jeffcott rotor shaft while whirling considering material linearity and non-linearity. [Shaft specification w.r.t section 4.2].

The deviation of point B relative to the tangent drawn to the elastic curve (Figure b) at point A, in a direction perpendicular to the original position of the shaft, is equal to,

$$t_{B/A} = \int_A^B x \, d\theta = \int_A^B \frac{Mx}{EI} \, dx = \left(\frac{1}{3} \times \frac{L}{2}\right) \times \frac{PL^2}{16EI} = \frac{PL^3}{96EI} = 27.4 \text{ mm}.$$

The deflection at the center of the shaft can be obtained with the help of the second moment area theorem between points A and B i.e.

$$r_B = \left(\theta_{AB} \times \frac{L}{2}\right) - t_{\frac{B}{A}} = \left(\frac{PL^2}{16EI} \times \frac{L}{2}\right) - \frac{PL^3}{96EI} = \frac{PL^3}{48EI} = 54.9 \text{ mm}.$$

Next, material non-linearity effect is handled as follows. When moment at the shaft center exceeds threshold bending moment, then shafts corresponding deflection will be higher. Under this consideration, the change in slope between the tangents drawn to the elastic curve at A and C,

$$\theta_{AC} = \frac{PL^2}{16EI} + \frac{1}{2} \times l_1 \times \left(\frac{M_r - M}{EI}\right) = 1.75 \text{ rad}.$$
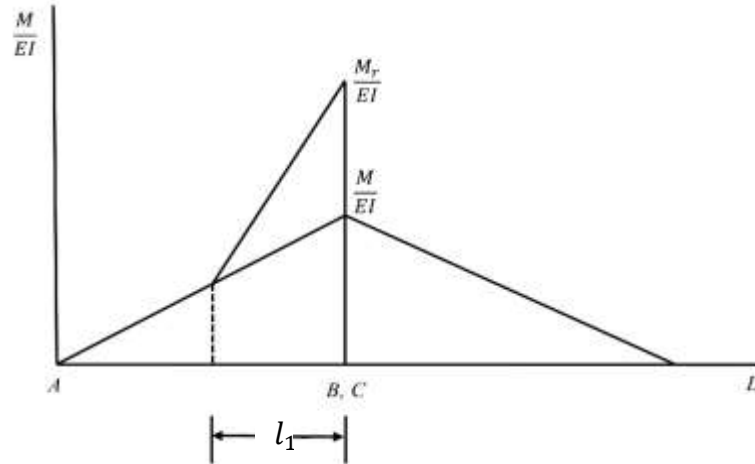
Figure (c): (M/EI) vs. Shaft length (L) diagram of a superelastic SMA Jeffcott rotor shaft
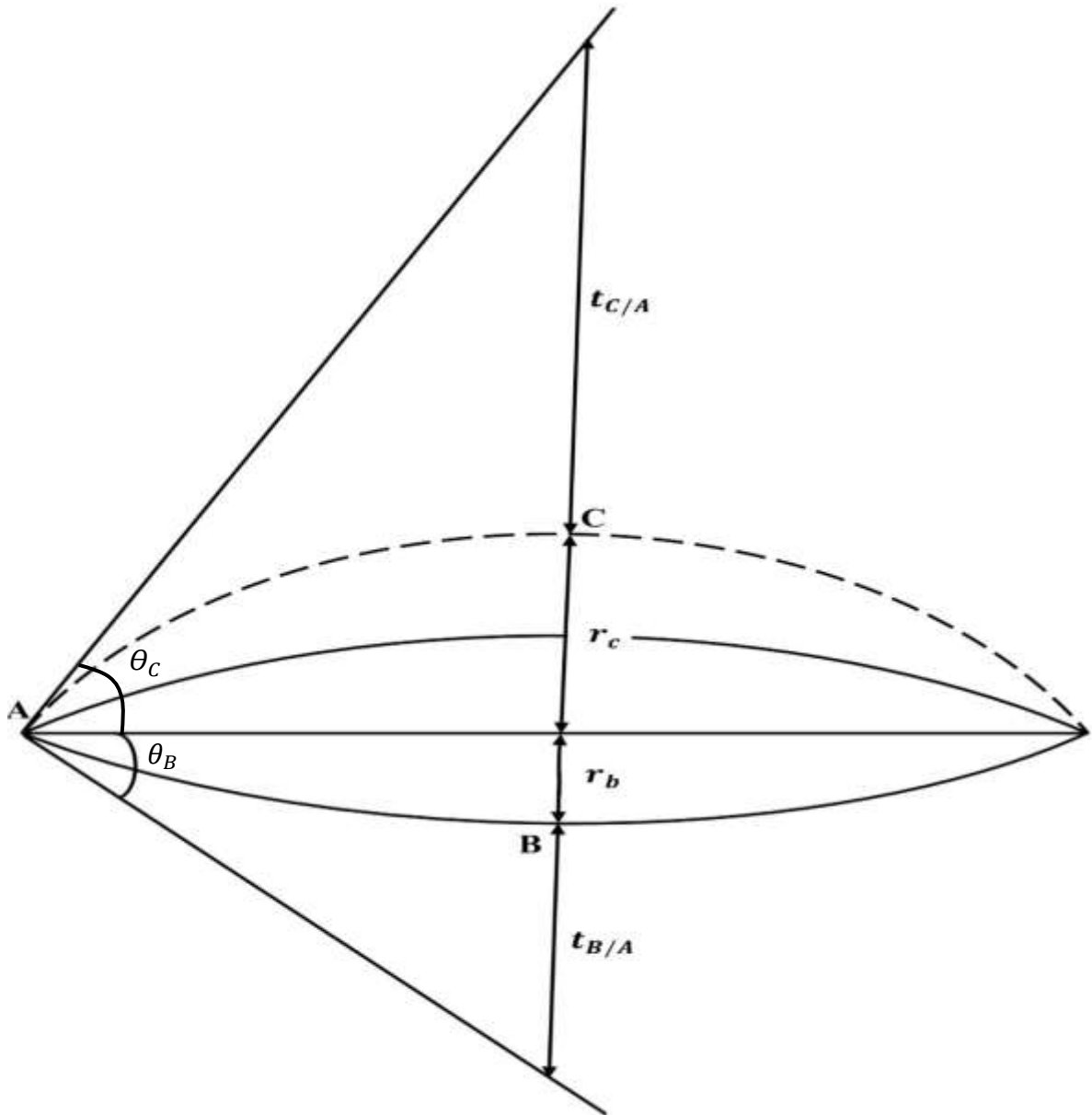
while whirling considering material linearity and non-linearity. [Shaft specification w.r.t section 4.2].

The deviation at point C relative to the tangent drawn to the elastic curve at point A, in a direction perpendicular to the original position of the beam, is equal to,

$$t_{C/A} = \frac{PL^3}{96EI} + \left[\frac{1}{3EI} \times l_1 \times \left\{\frac{1}{2} \times l_1 \times (M_r - M)\right\}\right] = 47.2 \text{ mm.}$$

The deflection at the center of the beam can be obtained with the help of the second moment area theorem between points A and B i.e.

$$r_c = \left(\theta_{AC} \times \frac{L}{2}\right) - t_{C/A} = 127.8 \text{ mm.}$$

APPENDIX – E

Matlab Code

E - 1: ** Program for Unsteady-state (Transient) Asynchronous Whirl of Jeffcott Rotor**

```
clear;clc
h=0.0001;
tfinal=0.6;

t(1)=0;
w(1)=0.001; x(1)=.1; y(1)=0; z(1)=0;
a=0.000025; b=115.98; c=14.5; d=0.2; e=1050.863;

f1=@(t,w,x,y,z) x;
f2=@(t,w,x,y,z) ((a*b^2)*cos(b*t-y)) + (w*(z)^2) - ((e*w)/d) - ((c*x)/d);
f3=@(t,w,x,y,z) z;
f4=@(t,w,x,y,z) (1/w)*((a*(b^2)*sin(b*t-y)-(c/d)*w*z - 2*x*z));

for i=1:ceil(tfinal/h)
    t(i+1)=t(i)+h;

    k1=f1(t(i), w(i), x(i), y(i), z(i));
    l1=f2(t(i), w(i), x(i), y(i), z(i));
    m1=f3(t(i), w(i), x(i), y(i), z(i));
    n1=f4(t(i), w(i), x(i), y(i), z(i))

    k2=f1(t(i)+.5*h, w(i)+0.5*k1*h, x(i)+.5*l1*h, y(i)+.5*m1*h, z(i)+.5*n1*h);
    l2=f2(t(i)+.5*h, w(i)+0.5*k1*h, x(i)+.5*l1*h, y(i)+.5*m1*h, z(i)+.5*n1*h);
    m2=f3(t(i)+.5*h, w(i)+0.5*k1*h, x(i)+.5*l1*h, y(i)+.5*m1*h, z(i)+.5*n1*h);
```

```matlab
n2=f4(t(i)+.5*h, w(i)+0.5*k1*h, x(i)+.5*l1*h, y(i)+.5*m1*h, z(i)+.5*n1*h);


k3=f1(t(i)+.5*h, w(i)+0.5*k2*h, x(i)+.5*l2*h, y(i)+.5*m2*h, z(i)+.5*n2*h);
l3=f2(t(i)+.5*h, w(i)+0.5*k2*h, x(i)+.5*l2*h, y(i)+.5*m2*h, z(i)+.5*n2*h);
m3=f3(t(i)+.5*h, w(i)+0.5*k2*h, x(i)+.5*l2*h, y(i)+.5*m2*h, z(i)+.5*n2*h);
n3=f4(t(i)+.5*h, w(i)+0.5*k2*h, x(i)+.5*l2*h, y(i)+.5*m2*h, z(i)+.5*n2*h);


k4=f1(t(i)+h, w(i)+k3*h, x(i)+l3*h, y(i)+m3*h, z(i)+n3*h);
l4=f2(t(i)+h, w(i)+k3*h, x(i)+l3*h, y(i)+m3*h, z(i)+n3*h);
m4=f3(t(i)+h, w(i)+k3*h, x(i)+l3*h, y(i)+m3*h, z(i)+n3*h);
n4=f4(t(i)+h, w(i)+k3*h, x(i)+l3*h, y(i)+m3*h, z(i)+n3*h);


w(i+1)= w(i) + (h/6)*(k1+2*k2+2*k3+k4);
x(i+1)= x(i) + (h/6)*(l1+2*l2+2*l3+l4);
y(i+1)= y(i) + (h/6)*(m1+2*m2+2*m3+m4);
z(i+1)= z(i) + (h/6)*(n1+2*n2+2*n3+n4);


end


%%
subplot (221)
plot (t,w,'MarkerFaceColor', 'k', 'MarkerEdgeColor','k', ...
    'LineWidth', 2);
ax = gca;
ax.FontSize = 14;
ax.FontWeight = 'bold';
xlabel ('t(s)');
ylabel ('r(m)');
grid on;
subplot (222)
```

```matlab
plot (t,x,'MarkerFaceColor', 'k', 'MarkerEdgeColor','k', ...
    'LineWidth', 2);
ax = gca;
ax.FontSize = 14;
ax.FontWeight = 'bold';
xlabel ('t(s)');
ylabel ('r(m/s)');
grid on;
subplot (223)
plot (t,y,'MarkerFaceColor', 'k', 'MarkerEdgeColor','k', ...
    'LineWidth', 2);
ax = gca;
ax.FontSize = 14;
ax.FontWeight = 'bold';
xlabel ('t(s)');
ylabel ('Theta(rad)');
grid on;
subplot (224)
plot (t,z,'MarkerFaceColor', 'k', 'MarkerEdgeColor','k', ...
    'LineWidth', 2);
ax = gca;
ax.FontSize = 14;
ax.FontWeight = 'bold';
xlabel ('t(s)');
ylabel ('Whirling speed (rad/s)');
grid on;
```

E - 2: ** Program for Finding Out of Reduced Modulus of Jeffcott Rotor shaft **

```
%number of steps must be even
n = 4;

d = .002;
radius = 0.001;
e1 = -0.107432661;
e2 = 0.15:0.01:0.17
del = e2-e1;

iterations = size(e2,2);
Ep = zeros(1,iterations);

%%
tic
for i = 1:iterations
    disp(sprintf('iter: %d, e1: %f e2: %f', i, e1, e2(i))); %#ok<DSPS>
    constant = (2*(d^2));
    r = romberg_manual(e1, e2(i), n);
    eppp = constant * r(n,n)/(e2(i)-e1)
    Ep(i) = eppp;
    if(eppp>0)
        break;
    end
    toc
end
%%
plot(del , Ep);
grid on;
```

```matlab
xlabel('Del', 'FontSize',12,'FontWeight','bold','Color','r');
ylabel('Ep', 'FontSize',12,'FontWeight','bold','Color','r');


function dat = getData()
%%% Import the data
% [~, ~, raw] = xlsread('streesVstrain.xlsx','Sheet1','A2:B41');


[~, ~, raw] = xlsread('final_sma2.xlsx','Sheet1','A2:B53');
%%% Create output variable
dat = reshape([raw{:}],size(raw));
clearvars data raw;


% All the vaues are randomly selected
%number of steps must be even
n = 8;
del = 0.228382;
d = .002;
radius = .001
e1 = -0.09395828
e2 = 0.134422


iterations = size(e1,2);
Ep = zeros(1,iterations)


%%% E vs DEL


%%
tic
for i = 1:iterations
    i
```

```matlab
    rho = d/del;
    constant = (128 *rho)/(pi * d * del^3)


    f =@(x) getStress(x)*x *(sqrt(abs((radius/rho)^2 - x.^2)));
    f(e1)
    f(e2)
    r = romberg(f, e1, e2, n)
    eppp = 10^6 * constant * r
%    Ep(i) = eppp;
    toc
end
%%
plot(del , Ep);
grid on;
xlabel('Del', 'FontSize',12,'FontWeight','bold','Color','r');
ylabel('Ep', 'FontSize',12,'FontWeight','bold','Color','r');
```

E - 3: ** Program for Finding of Bending moment of Jeffcott Rotor Shaft **

```
%number of steps must be even
n = 4;

d = .002;
radius = 0.001;
e1 = -0.107432661;
e2 = 0.15:0.01:0.17
del = e2-e1;

iterations = size(e2,2);
Ep = zeros(1,iterations);

%%
tic
for i = 1:iterations
    disp(sprintf('iter: %d, e1: %f e2: %f', i, e1, e2(i))); %#ok<DSPS>
    constant = (2*(d^2));
    r = romberg_manual(e1, e2(i), n);
    eppp = constant * r(n,n)/(e2(i)-e1)
    Ep(i) = eppp;
    if(eppp>0)
        break;
    end
    toc
end
%%
plot(del , Ep);
grid on;
```

```matlab
xlabel('Del', 'FontSize',12,'FontWeight','bold','Color','r');
ylabel('Ep', 'FontSize',12,'FontWeight','bold','Color','r');


function dat = getData()
%% Import the data
% [~, ~, raw] = xlsread('streesVstrain.xlsx','Sheet1','A2:B41');


[~, ~, raw] = xlsread('final_sma2.xlsx','Sheet1','A2:B53');
%% Create output variable
dat = reshape([raw{:}],size(raw));
clearvars data raw;


% All the vaues are randomly selected
%number of steps must be even
n = 8;
del = 0.228382;
d = .002;
radius = .001
e1 = -0.09395828
e2 = 0.134422


iterations = size(e1,2);
Ep = zeros(1,iterations)
n=8;
del = 0.228382;
d = .002;
radius = .001
e1 = -0.09395828
e2 = 0.134422
```

```
iterations = size(e1,2);
Ep = zeros(1,iterations)


%% E vs DEL

%%
tic
for i = 1:iterations
    i
    rho = d/del;
    constant = 2 * d^3 / (del(i)^3);


    f =@(x) getStress(x)*x *(sqrt(abs((radius/rho)^2 - x.^2)));
    f(e1)
    f(e2)
    r = romberg(f, e1, e2, n)
    eppp = 10^6 * constant * r
%    Ep(i) = eppp;
    toc
end
%%
plot(del , Ep);
grid on;
xlabel('Del', 'FontSize',12,'FontWeight','bold','Color','r');
ylabel('Ep', 'FontSize',12,'FontWeight','bold','Color','r');
```

Appendix – F

A Problem and Solution (Example 3.4.1) from Thomson et. al. (2011)

Turbines operating above the critical speed must run through dangerous speed at resonance each time they are started or stopped. Assuming the critical speed ω_n to be reached with amplitude r_o, determine the equation for the amplitude buildup with time. Assume zero damping.

Solution

We will assume synchronous whirl as before, which makes $\dot{\theta} = \omega = \text{constant}$ and $\ddot{\theta} = 0$. However, $\ddot{r}$ & $\dot{r}$ terms must be retained unless shown to be zero. With $c = 0$ for the undamped case, the general equations of motion reduce to

$$\ddot{r} + \left(\frac{k}{m} - \omega^2\right)r = e\omega^2 \cos\phi \ldots\ldots\ldots\ldots\ldots\ldots..(1)$$

$$2\dot{r}\omega = e\omega^2 \sin\phi \ \ldots\ldots\ldots\ldots\ldots\ldots\ldots.....\ldots..(2)$$

The solution of the second equation with initial deflection equal to r_o is

$$r = \frac{e\omega}{2}t\sin\phi + r_0 \ldots\ldots\ldots\ldots\ldots\ldots\ldots\ldots\ldots..(3)$$

Differentiating this equation twice, we find that $\ddot{r} = 0$; so the first equation with the above solution for r becomes

$$\left(\frac{k}{m} - \omega^2\right)\left(\frac{e\omega}{2}t\sin\phi + r_0\right) = e\omega^2 \cos\phi\ldots\ldots..(4)$$

Because the right side of this equation is constant, it is satisfied only if the coefficient of t is zero:

$$\left(\frac{k}{m} - \omega^2\right)\sin\phi = 0\ldots\ldots\ldots\ldots\ldots.\ldots\ldots(5)$$

Which leaves the remaining terms:

$$\left(\frac{k}{m} - \omega^2\right) r_0 = e\omega^2 \cos \phi \dots\dots\dots\dots\dots(6)$$

With $\omega = \sqrt{k/m}$, the first equation is satisfied, but the second equation is satisfied only if $\cos \phi = 0$ or $\phi = \pi/2$. Thus, we have shown that at $\omega = \sqrt{k/m}$, or at resonance, the phase angle is π/2 as before for the damped case, and the amplitude builds up linearly according to the equation shown in following Figure.